AN ABSTRACT OF THE THESIS OF

Cheng-Chang Huang for the degree of Doctor of Philosophy in

Civil Engineering Presented on August 30, 1990.

Title: Local Scour at Isolated Obstacles on River Beds

Redacted for Privacy

Abstract Approved: __

Peter C. Klingeman

Maximum equilibrium scour depths, equilibrium scour volumes,

and induced equilibrium movements at isolated obstacles on river

beds were investigated in clear-water scour. The research was

achieved by a systematic flume study based on the results of

dimensional analysis of local scour.

The main tested obstacles for local scour were cubes. Local

scour at a circular cylinder of aspect ratio 1 and a sphere were

also examined for comparison with scour at cubes. Each obstacle was

placed on a flat movable bed and oriented normal to the incident

flow. Non-cohesive uniform medium sand and very fine gravel were

used as movable beds. The tested flow conditions were controlled to

give many combinations of the relevant dimensionless parameters for

local scour: the flow Froude Number, relative obstacle size, and

relative roughness of bed material.

Water surface profiles and longitudinal velocity profiles along

the plane of symmetry, as well as the horizontal velocities near the

bed around isolated obstacles on a fixed bed were examined in several runs. For a slightly submerged cube, the path of maximum velocity downstream of the cube moves from the water surface into the lower part of the flow. At a greater distance downstream, the path of maximum velocity tends to move upward toward the water surface. An increase of flow Froude Number leads to a hydraulic jump behind the cube. The relative longitudinal velocity near the bed is increased in this region. The decrease of relative water depth or the increase of flow Froude Number can lead to increased average relative horizontal velocity (V/u) near a cube. The cube has the highest average V/u value, as compared to flow near a circular cylinder and a sphere.

The local scour processes and equilibrium scour patterns at isolated cubes on movable beds were also examined. There is not a unique equilibrium scour pattern for clear-water scour at a cube on a movable bed. Equations were developed to predict the maximum equilibrium scour depth and scour volume and the critical condition for incipient motion of bed material at a cube in clear-water scour. As the water becomes relatively deep, the shape effect of the circular cylinder and the sphere become negligible. The major equilibrium movement of a cube on a movable bed due to scour involves longitudinal displacement, vertical settlement, and longitudinal inclination. Equations were developed to predict the equilibrium movement and the critical condition for incipient upstream movement of a cube in clear-water scour.

Local Scour at Isolated Obstacles on River Beds

by

Cheng-Chang Huang

A THESIS

submitted to

Oregon State University

in partial fulfillment of
the requirements for the
degree of

Doctor of Philosophy

Completed August 30, 1990

Commencement June 1991

APPROVED:

Redacted for Privacy
Professor of Civil Engineering in charge of major

Redacted for Privacy

Head of Department of Civil Engineering

Redacted for Privacy

Dean of Graduate School

Date thesis is presented_____August 30, 1990_____

ACKNOWLEDGEMENTS

TABLE OF CONTENTS

LIST OF FIGURES

LIST OF TABLES

LIST OF APPENDIX TABLES

LOCAL SCOUR AT ISOLATED OBSTACLES ON RIVER BEDS

I. INTRODUCTION

Research Need

An isolated large obstacle placed on the bed of an alluvial river will disturb the nearby flow, causing local scour of some of the bed material near the obstacle and formation of a scour hole. Application of such scouring effects has been made to modify local river environments as part of fish habitat rehabilitation and enhancement in the Pacific Northwest (Klingeman, 1984). For example, large boulders are often used to provide greater water depth and cover for fish. Important information needed for such applications includes the predicted scour depths and scour volumes that can be achieved. Information is also needed on the likelihood that the obstacle may sink into the bed as a consequence of local scour.

Unfortunately, this information is not presently available except as "rules of thumb" developed from trial-and-error field experience, a conclusion supported by an extensive review of the hydraulic literature. Research and design attention have concentrated almost entirely on the problem of local scour around bridge piers. These structures are fixed into the river bed and are fully exposed above the water surface. Thus, none of the previously

studied objects has a flow geometry like that for the isolated objects being widely used in fish habitat work.

The possible relationships of the obstacle to river flow characteristics, to bed material, and to the geometric boundary of the obstacle are still largely unknown. Research attention is needed on this problem not only for the practical application to habitat work but also for a better understanding of the problem and for general applications in the hydraulic sciences.

Research Objectives

The overall objective of this research is to develop a predictive knowledge of the local scour at isolated large obstacles on alluvial river beds. This includes situations when such obstacles are subject to fully submerged local scour and partially submerged local scour, over a range of conditions.

Five specific objectives provide detail to this broader objective. These are as follows:

1. To identify the important parameters involved in local scour around large isolated obstacles in an alluvial channel;

2. To highlight the major features of local scour around such isolated obstacles;

3. To examine the flow fields around isolated obstacles of differing geometry under different flow conditions;

4. To examine whether the development of local scour at
    isolated obstacles over time may lead to partial sinking
    and burial of the obstacles; and

5. To isolate some of the key parameters which govern the
    local scouring process and to represent the results in
    graphical form and/or by formula to describe the scour
    depth, scour volume and obstacle displacement as a function
    of these key parameters.

Research Scope and Approach

The application of mathematical modeling and analytic solutions
to sediment transport problems is far behind the development of
experimental findings. The exact mathematical description has not
been established due to the extremely complicated interaction
between flowing water and sediment (Wang, 1982, 1987). Experimental
research is necessary to solve the complex problems of sediment
transport.

The approach to the problem of local scour at isolated
obstacles is through an experimental laboratory investigation.
Emphasis is placed on laboratory work because of the extremely
complicated interactions that occur among the moving boundaries of
water surface, river bed, and the obstacle surface as obstacle
displacement occurs. These changes are highly turbulent,
three-dimensional and time-dependent in nature during the local
scouring process. In nature, a systematic study such as researched

here is very difficult because of extraneous variables (e.g.,
debris) and lack of control over dominant variables.

An extensive series of movable-bed experiments is designed and
conducted, based upon the concepts of dimensional analysis and use
of avaliable experimental facilities. The research is restricted
mainly to the local scour at isolated cubes (four test sizes) on
river beds under clear water scour and sustained steady flow
conditions upstream. Two other test shapes -- cylinders of aspect
ratio 1 and spheres -- are also used as isolated obstacles in this
research, but their use is limited to comparative purposes only.
Data are obtained using a laboratory flume with a test reach filled
with non-cohesive sediment in two test sizes (medium-sized sand and
very fine gravel).

Before conducting movable-bed experiments, a few fixed-bed
experiments are carried out to get general information about the
structure of the flow field by measuring the mean flow fields around
the various isolated obstacles. In order to better understand the
physical processes in the research problem, the local scouring
processes and the induced obstacle movements are observed, measured
and photographed during the movable-bed experiments. At the end of
these experiments, the local scour patterns, scour volumes, maximum
scour depths, and obstacle movements are carefully measured and
documented photographically. These data are later analyzed and
discussed to determine the possible relationships which might exist
for local scour at isolated obstacles on river beds.

II. REVIEW OF LITERATURE

Overview of Literature Review

The available literature contains very few studies on local scour at isolated obstacles on river beds, especially when the obstacles are fully submerged in the flow. Most of the literature is related to local scour around bridge piers, which are fixed into river beds and fully exposed above water surface.

Local scour is closely related to the disturbed flow fields near the fluid-sediment boundaries at obstacles. Therefore, a review of the flow fields around isolated obstacles and of bridge pier scour can provide a qualitative understanding of the scour processes and give valuable clues for determination of the important variables in this study.

The literature review begins with the description of flow fields around isolated obstacles on fixed ground planes. This is followed by a review of the local scour around bridge piers fixed into river beds. Finally, the limited existing literature concerning the local scour at isolated obstacles on river beds is reviewed.

Flow Field Around Isolated Obstacles on Fixed Planes

Figure 1 defines several variables used in discussing the work of several investigators. The isolated obstacles are described by
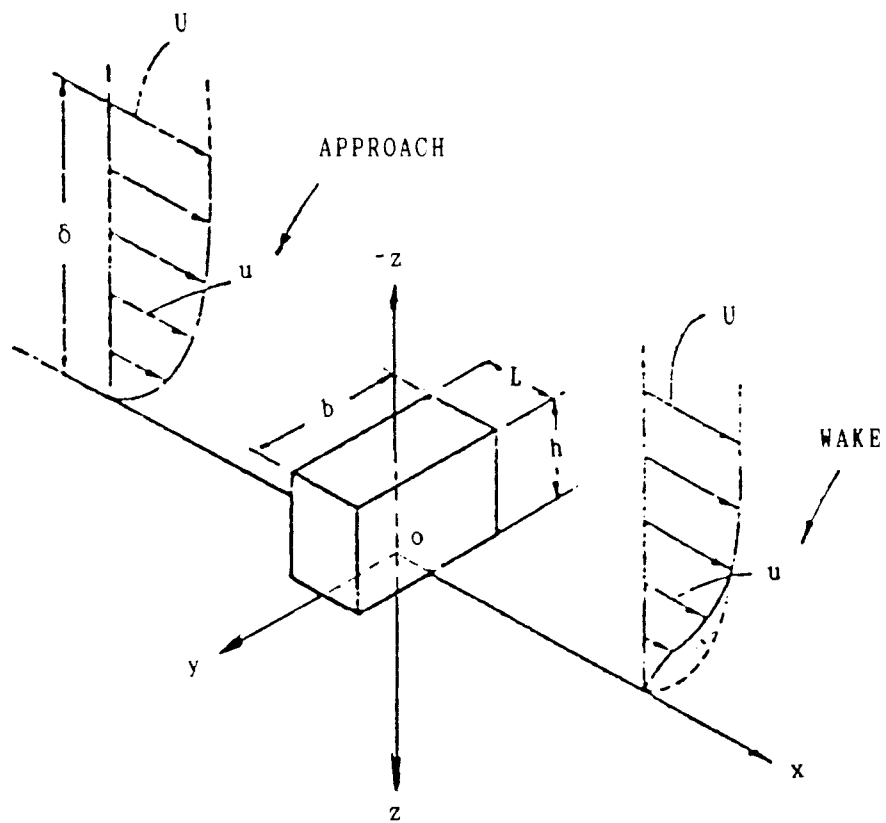
Figure 1. Definition of variables for flow at isolated obstacles.

their height, h, width, b, and length, L. The flow is described by

its freestream velocity in the x direction, U, local longitudinal

component of velocity, u, and its boundary layer height or

thickness, δ. The three coordinate axes are identified by x, y, and

z. The z axis has been taken at positive downward because its main

use is to describe scour (and the right hand rule for coordinates is

being followed as the observer looks downstream).

Peterka et al. (1985) revealed the mean wind flow patterns

about buildings of cube shape. Key findings are shown in Figure 2.

In Figure 2(a), the flow approaching the obstacle separates from the

surface at some distance upwind of the building. This separation

distance is primarily dependent on the building height-to-width

ratio (h/b), building height to boundary layer height ratio (h/δ),

and upstream surface roughness. The vorticity in this separated

flow, in combination with the pressure distribution on the front of

the building, results in downward flow on the front of the building.

This subsequently causes the separated flow to roll up into a vortex

and wrap around the building by convection into a horseshoe shape.

This primary horseshoe vortex induces additional vortices of smaller

size and strength (Figures 2(b) and 2(c)) which are eventually

incorporated into the primary horseshoe vortex around the side of

the building and lose their individual identity. The horseshoe

vortex can still be identified in the flow at some distance downwind

from the obstacle. The approaching flow separates at the front edge

of the top and sides of the obstacle and may or may not reattach to

the top or sides before reaching the back edges. Reattachment
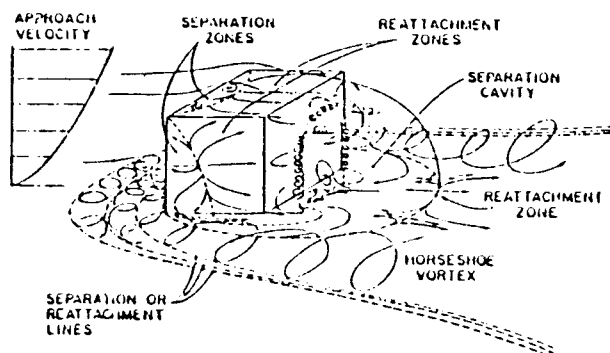
(a) Mean streamline patterns about a cube.
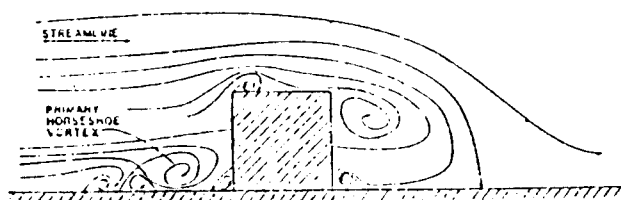
(b) Centerline streamline patterns for flow reattaching to top of cube.
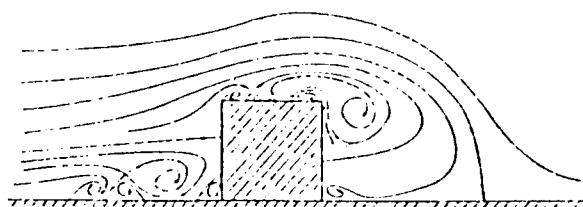
(c) Centerline streamline patterns for flow not reattaching to top of cube.

Figure 2. Mean wind flow patterns about a cube-shaped building. (Peterka et al., 1985).

depends on length to width ratio (L/b), height to length ratio (h/L) and boundary layer height (δ). Figures 2(a) and 2(b) show flow patterns for a reattached flow; Figure 2(c) shows flow patterns for an unreattached flow. The reattached flow downstream from the building requires some distance before the wind recovers the characteristics of the approach boundary layer and all disturbances caused by the building disappear. A rougher boundary upwind of the building results in a high level of turbulence in the approach wind. This causes the wake to disappear more quickly and any evidence of the horseshoe vortex in the wake to diminish. The aspect ratio (h/b) influences the magnitude and persistence of the wake. An increasing of h/b increases the distance of downstream velocity "defect" compared to upstream approach conditions. The effective length of the turbulence wake is about the same as for the mean velocity wake.

Gowda et al. (1983) presented experimental data in support of these general observations. Figure 3 schematically indicates the observed surface flow pattern around an isolated rectangular obstacle in a boundary layer. For upwind flow velocity U = 18 m/s, and with b = 3 cm and a maintained h/δ = 2 in a wind tunnel with a 30 x 12 cm cross section, they found that the relative distance of the primary separation point (S_1/b) far upwind from the front face of a rectangular obstacle increased linearly with h/b value. Thus, the S_1/b value ranges from 0.8 to 1.25 for constant L/b = 1, and ranges from 0.8 to 1.4 for constant L/h = 1 when the h/b value increases from 1 to 4. The changes in the relative distance of the
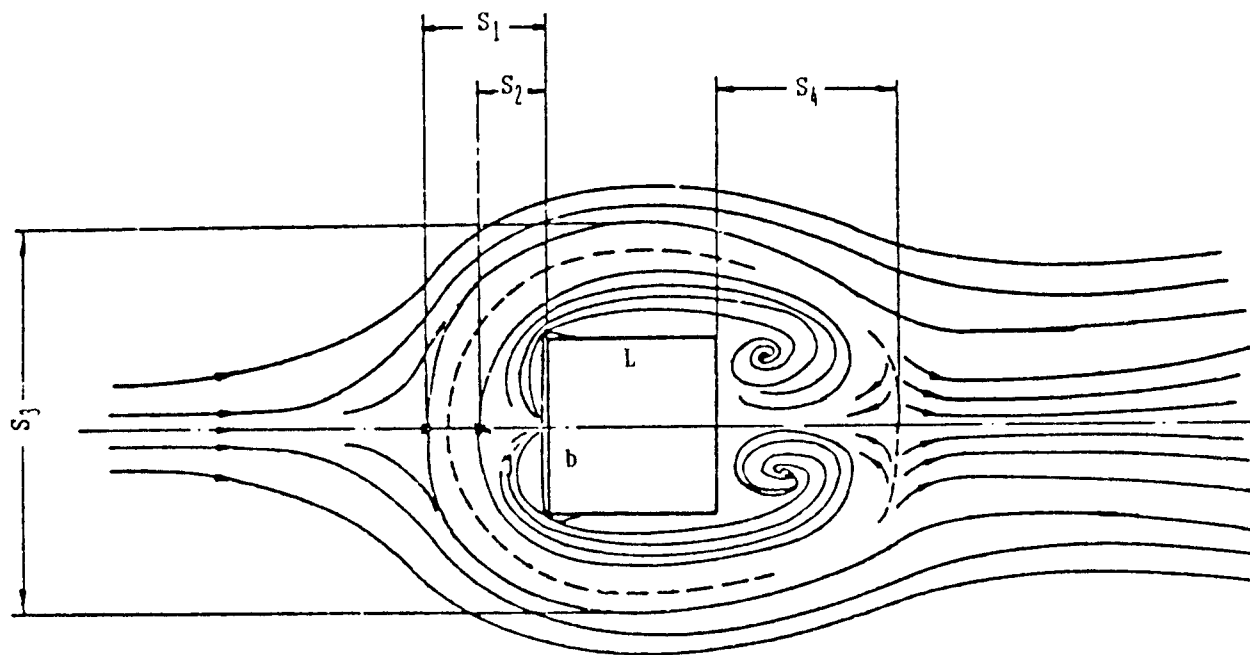
Figure 3. Schematic view of the flow past a three-dimensional rectangular
body on a ground plane (Gowda et al., 1983).

secondary separation point (S_2/b) of the primary horseshoe vortex

and the maximum relative width between the two primary separation

points (S_3/b) on each side of the obstacle are similar to changes

for S_1/b but less severe. The S_2/b value ranges from 0.5 to 0.6 for

constant L/b = 1, and ranges from 0.5 to 0.8 for constant L/h = 1

when h/b value increases from 1 to 4. The S_3/b value ranges from

3.0 to 4.0 for constant L/b = 1, and ranges from 3.0 to 3.4 for

constant L/h = 1 when the h/b value increases from 1 to 4. The

relative near-wake length (S_4/b) between the rear face and the

downwind reattachment point of the obstacle also increases linearly

with h/b at constant L/b = 1. It ranges from 1.7 to 3.4, whereas

there is hardly any change for constant L/h = 1 when the h/b value

increases from 1 to 4. For a cube with h/δ between 0.5 and 2.5 at a

constant value of δ, they further discovered that S_1/b increased

slightly with h/δ but the values of S_2/b, S_3/b and S_4/b remained

constant.

Castro and Robins (1977) measured the longitudinal mean

velocity and turbulence intensity in the near-wake region behind a

cube in a 2.7 x 9.1 m (cross section) wind tunnel. The size of the

cube was 20 cm, which was one tenth of the upstream boundary

thickness. Figures 4 and 5 show the major features of the near-wake

flow. A significant mean velocity defect exists and the intensity

of turbulence is largely intensified in the near wake. As the wake

flow moves downstream, the mean velocity tends to restore to its

original value that exists far upstream of the cube.

For the far wake flow behind the cube, Okamoto (1985) revealed
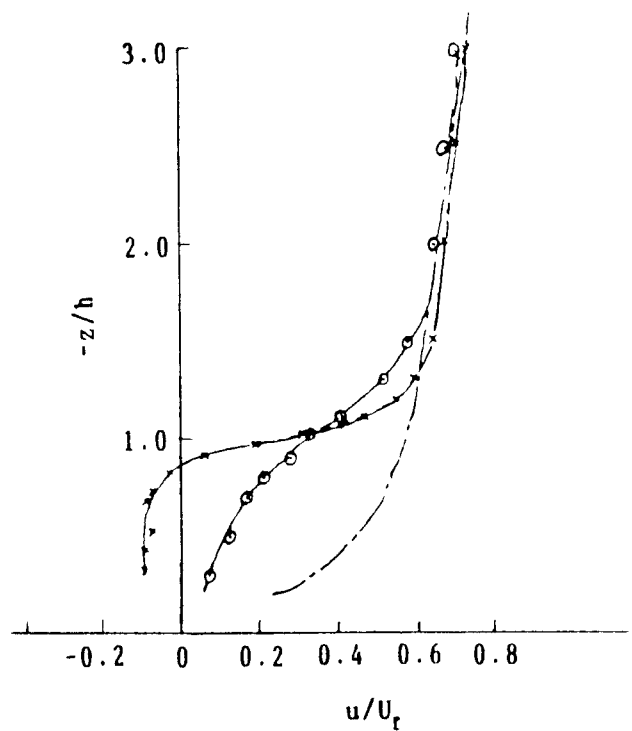
(a) Mean velocity variations in the wake.
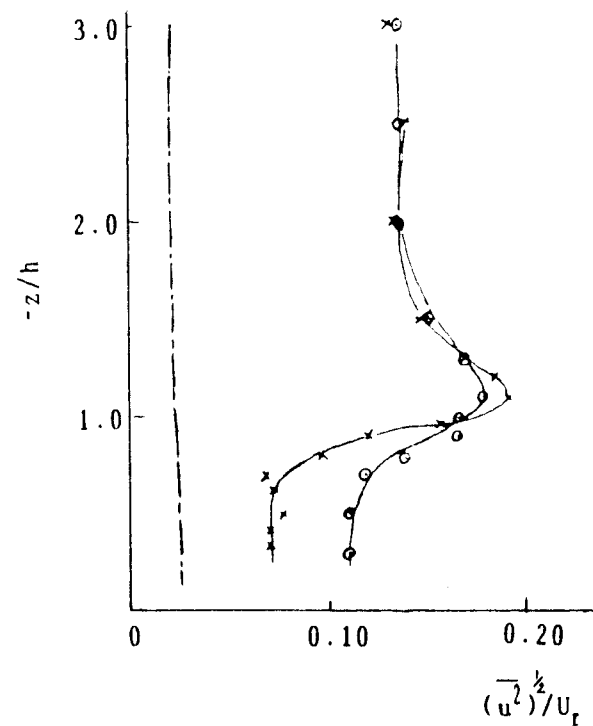
(b) Turbulence intensity variation.

Key: —x—, x/h = 1.0; —o—, x/h = 2.0; —·—, upstream approach flow variation.

Figure 4.   Near-wake flow behind a cube on y/h = 0 (Castro and Robins, 1977).
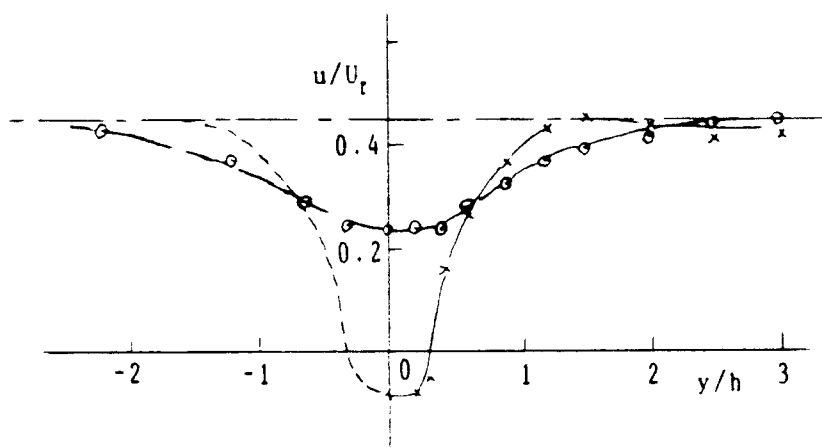
Key: —x—, x/h = 0.75; --o--, x/h = 3.0; ———, upstream approach
       flow variation.

Figure 5.   Lateral mean velocity variations for boundary-layer
            upstream flow on -z/h = 0.5 (Castro and Robins, 1977).

the following features in his wind tunnel experiment. For the longitudinal velocity component u, the velocity defect decreases with an increasing vertical distance of ⁻z from the ground plane. The transverse spread of the velocity defect is large at lower value of ⁻z/h, and it decreases with an increasing upward distance from the ground plane. The velocity defect and the turbulence intensity decrease and the width of the wall wake increases with an increasing downstream distance.

Baker (1979) investigated the laminar horseshoe vortex on the plane of symmetry upstream of a circular cylinder in a wind tunnel. The circular cylinder had b = 7.6 cm and b/h = 2. The wind tunnel cross-section was 30.5 x 15.3 cm. Three different types of vortex systems were observed. These were, with increasing obstacle Reynolds Number Re_b (Ub/ν, where ν is the kinematic viscosity of the fluid):

1. Steady horseshoe vortex systems with 2, 4 or 6 vortices. The number of vortices increase as Reynolds Number increases;

2. Horseshoe vortex systems which exhibit a regular oscillatory motion;

3. Horseshoe vortex systems which exhibit an irregular unsteady behaviour.

The velocity measurements in the steady laminar horseshoe vortex systems indicated that the vertical component of velocity (w) is an order of magnitude smaller than the longitudinal component of velocity (u). The velocity component of the primary vortex was much

greater than other vortices. There was found to be little variation in the dimensionless velocity profile within the primary vortex, as shown in Figure 6, when the flow speed varied. The high velocity gradient beneath the primary vortex infers there is a considerable increase in shear stress beneath the vortex. The shear stress there is almost five times its value far upstream of the cylinder.

Eckerle and Langston (1987) investigated the horseshoe vortex formation around a circular cylinder having h/b = 1 (b = 29.8 cm) in a wind tunnel with a cross section of 180 x 30.5 cm. For an approach flow velocity $\overline{U}$ = 30.5 m/s, and with one tenth of the cylinder width for the boundary layer thickness at x/b = -2.72, they measured the mean radial velocity vectors in several angular planes. Results are shown in Figure 7. On the plane of symmetry, the reverse flow does not roll up to form a vortex. It passes out of the plane and proceeds tangentially around the cylinder next to the separation line. The velocity vectors in the 5-degree plane (not given in Figure 7) show a similar flow pattern to that in the plane of symmetry. The horseshoe vortex become fully formed between the plane of symmetry and 25-degree plane. The velocity vectors in the 45-degree plane (not given in Figure 7) are similar to those in the 25-degree plane. The vortex structure in the 90-degree plane is much weaker than that in the 45-degree plane. The vortex core moves radially outward and slightly away from the ground plane as the vortex passes around the cylinder. No multiple vortex pattern was present in the experiments.

Melville and Raudkivi (1977) studied the flow fields around a
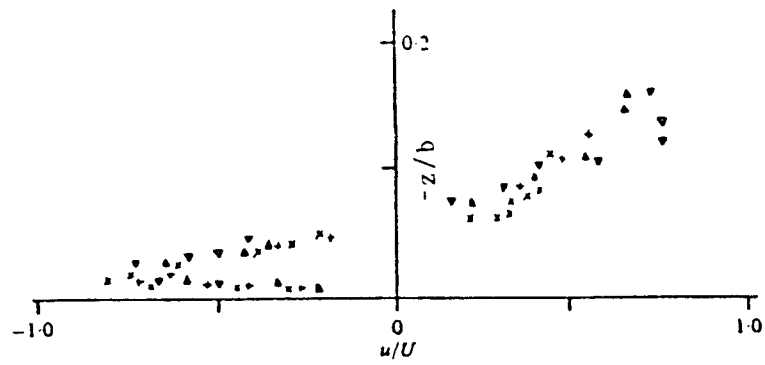
(a) u/U versus ⁻z/b.
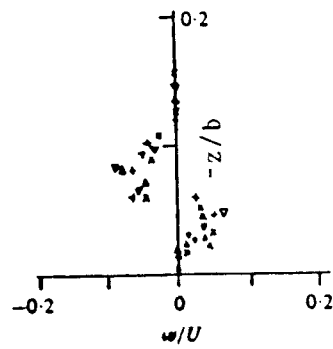
(b) w/U versus ⁻z/b.

Figure 6.   Velocity profiles through primary horseshoe vortex at
x/b = -0.67 in laminar flow (Baker, 1979).
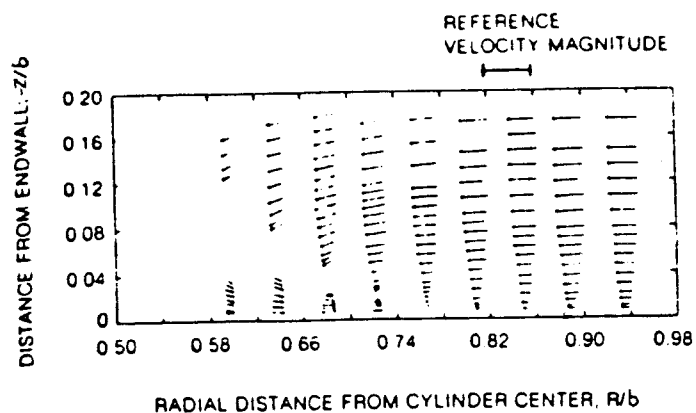
(a) the plane of symmetry.
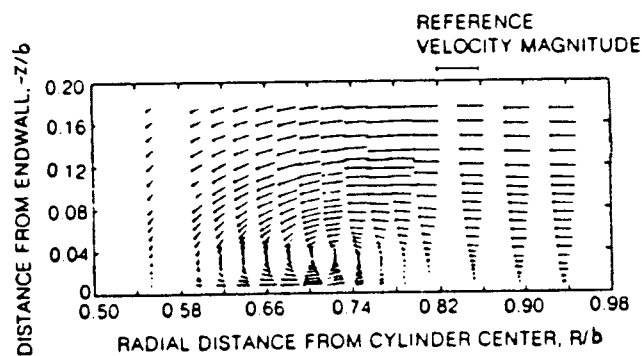
(b) the 25-degree plane.
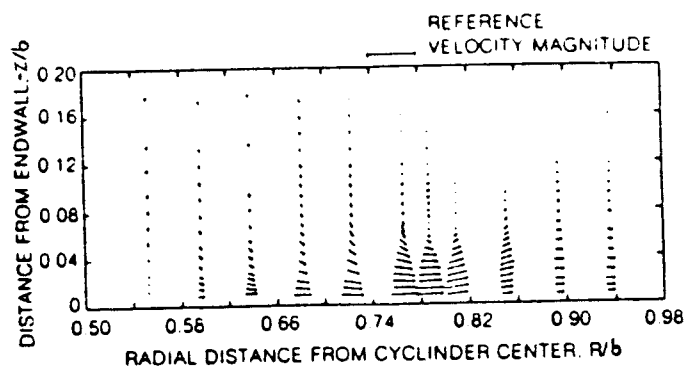
(c) the 90-degree plane.

Figure 7. Velocity vectors in the angular planes around a circular cylinder (Eckerle and Langston, 1987).

circular cylinder in a water flume. They indicated a strong
downflow in front of the cylinder and a spiralling flow around the
cylinder, similar to the findings of others in wind tunnel
experiments. The circulation was strongest on the plane of
symmetry, decreasing around the perimeter of the cylinder as the
spiral flow expanded in cross section. The most significant flows
in the near-wake zone and near the bed were strong upflow and
somewhat weaker backflow, respectively.

Eckman and Nowell (1984) made a detailed investigation of the
boundary skin friction distribution around a submerged isolated
circular cylinder in a water flume 5.28 m long and 15.5 cm wide.
They found the flow pattern around the cylinder shown in Figure 8.
The patterns of boundary skin friction were tested quantitatively
for dependence on the cylinder height and diameter, as well as on
the magnitude of the imposed (upstream) boundary shear stress.
Production and decay of skin friction within the wake region were
also described. In all experiments, the water depth D was kept
constant at 10 cm and the h/D value was confined between 0.05 and
0.20. The h value ranged from 0.5 cm to 2 cm, and the b value
ranged from 0.3 cm to 0.6 cm. Some typical distributions found for
the skin friction on the bed are shown in Figures 9 and 10. In
these figures, the mean skin friction, $\bar{\tau}$, is normalized by
comparision with the mean imposed shear stress of the flow, $\bar{\tau}_i$. The
authors related the stress distributions to the anticipated regions
of scour and deposition around the cylinder. A large region of
increased mean skin friction always occurred several diameters
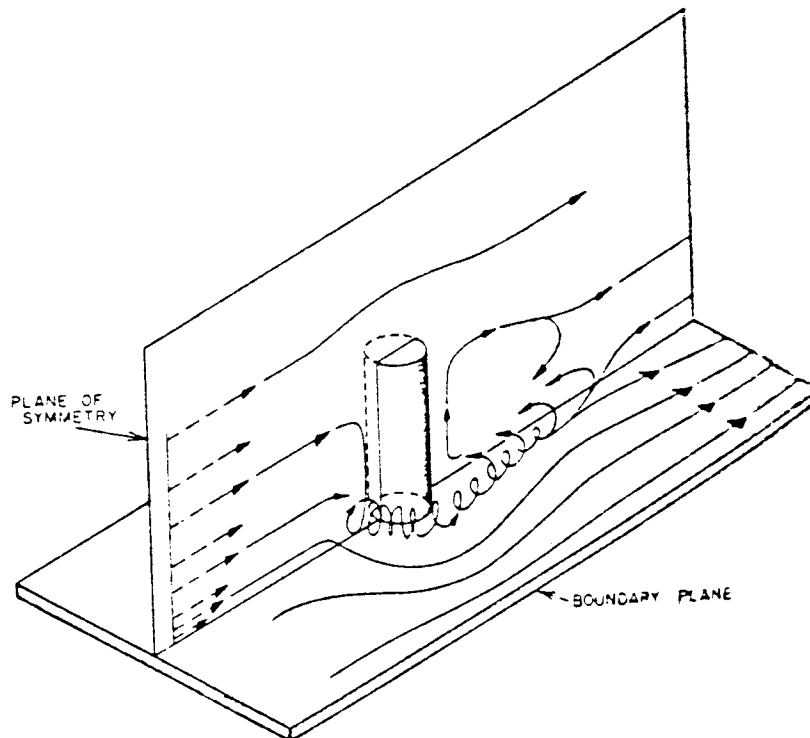
Figure 8. Schematic representation of flow about an isolated
cylinder at $90 < Re_b < 906$, as indicated by dye-injection
studies (Eckman and Nowell, 1984).
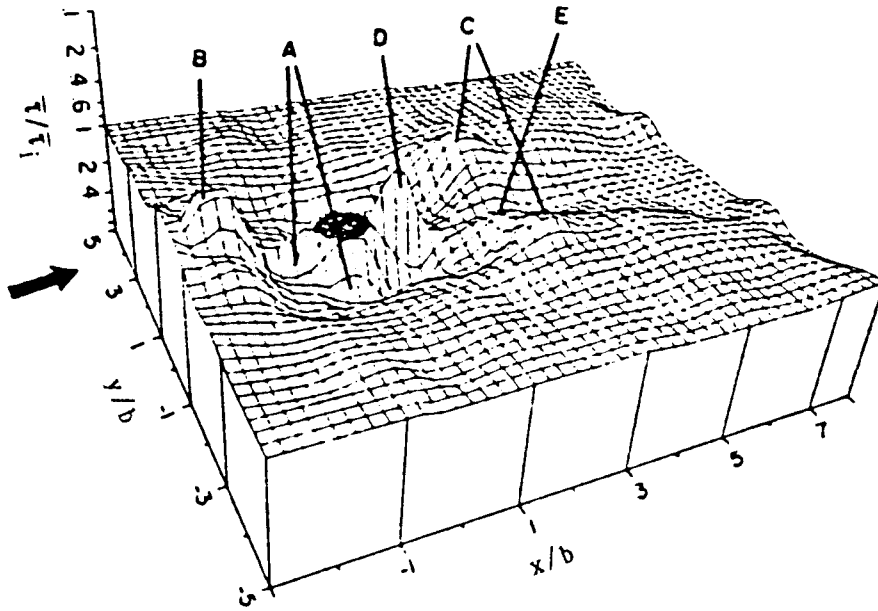
(a) cylinder 1 cm high, 0.45 cm wide in flow 10 cm deep;
$\bar{\tau}_i$ = 0.98 dyn cm^{-2}
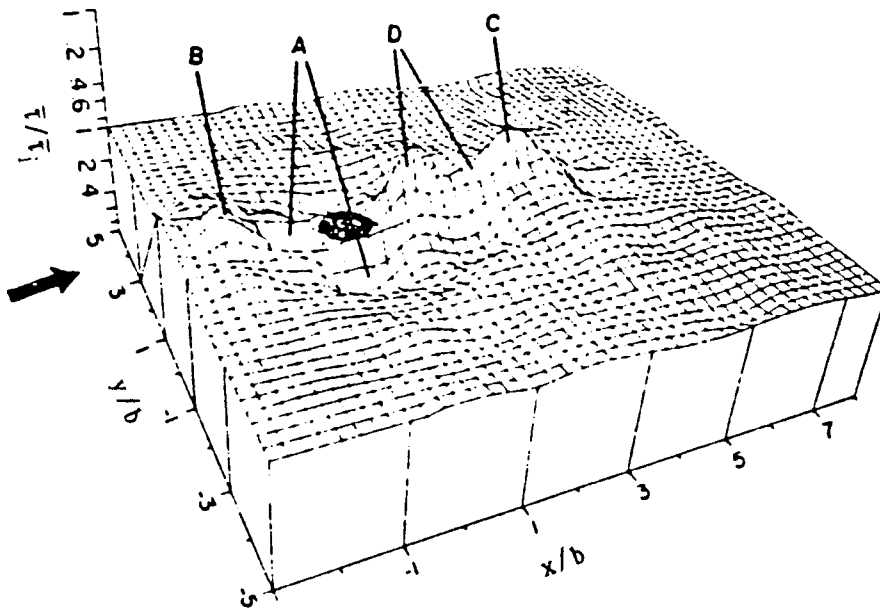
(b) cylinder 0.5 cm high, 0.45 cm wide in flow 10 cm deep;
$\bar{\tau}_i$ = 0.98 dyn cm^{-2}

key: $\bar{\tau}$ = mean skin friction; $\bar{\tau}_i$ = imposed shear stress.

Figure 9. Distribution of mean skin friction on bed near cylinder,
normalized to the imposed shear stress. Cylinder
location is indicated by the solid circle. A local
increase in mean skin friction is represented by a
depression in the surface (Eckman and Nowell, 1984).
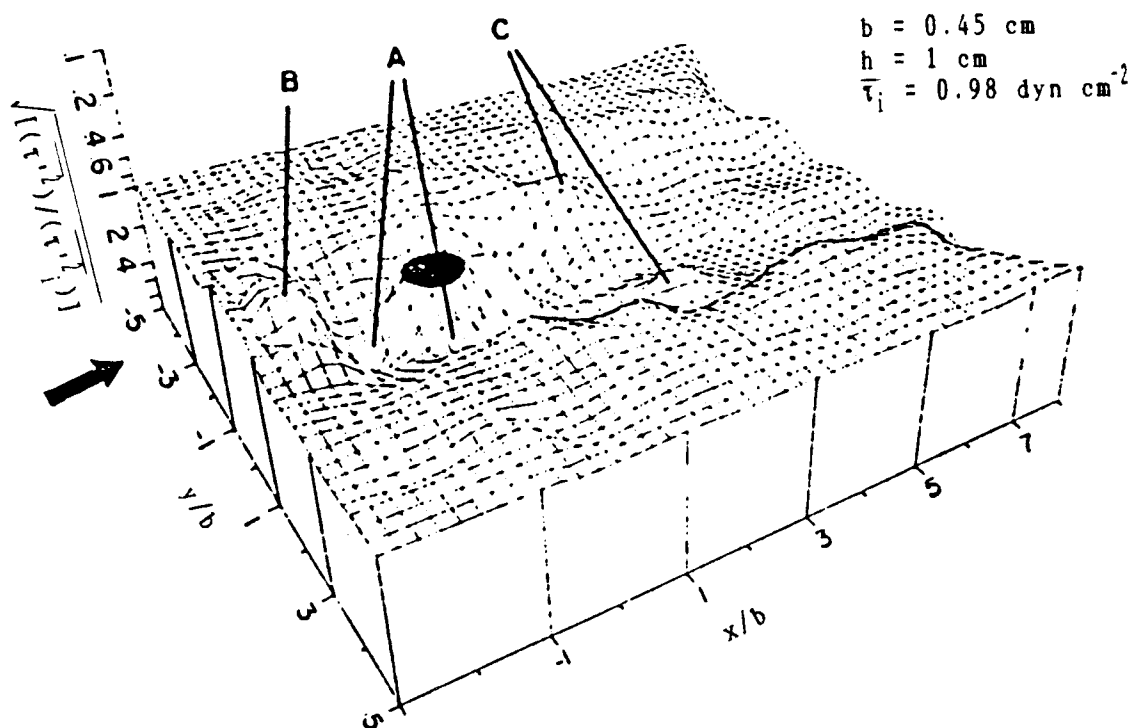
Key: $\sqrt{(\overline{\tau'^2})}$ = turbulent fluctuation skin friction;

$\sqrt{(\overline{\tau'^2}_i)}$ = imposed turbulent shear stress.

Figure 10. Distribution of turbulent fluctuations in bed skin friction near 1 cm cylinder, normalized to the imposed turbulent shear stress. Interpretation as in Figure 9 (Eckman and Nowell, 1984).

directly upstream of the cylinder (region A of Figures 9). The

extent of this region ranged from two to five cylinder diameters

cross-stream. Turbulence intensity also increased at the cylinder's

upstream and lateral faces (region A of Figure 10). A region of

reduced mean skin friction always occurred several diameters

directly upstream of the cylinder (region B of Figures 9). This

region was approximately five diameters upstream of the cylinder and

upstream of the margin of the horseshoe vortex. Turbulence

intensities typically were reduced within this region (region B of

Figure 10). In all cases studied, laterally symmetrical regions of

reduced mean skin friction occurred downstream of and lateral to the

cylinder (region c of Figure 9). The increased turbulent

fluctuations filled a widening area downstream (dashed line in

Figure 10). This lateral spread seemed to reach an asymptote at

$y = 2\text{-to-}4\ b$. In general, turbulent fluctuations along the plane of

symmetry attained a maximum downstream value at $x = 1\text{-to-}2\ b$, and

then decayed monotonically. The near-wake pattern of boundary skin

friction depended strongly on cylinder dimensions and boundary shear

stress imposed by the external flow (region D of Figure 9). The

average relative skin friction of the region adjacent to the

cylinder ranged from 1.29 to 1.89, with point estimates of relative

skin friction value as high as 6.94. Highest ratios typically

occurred just upstream of the cylinder. The authors further

identified that any cylinder confined to the logarithmic-velocity-

profile layer ($h < \delta$) will experience a weaker pressure gradient on

its upstream face, and will thereby create a weaker horseshoe

vortex, than will a cylinder that reaches the higher velocity region above the boundary layer.

Okamoto (1980) described the flow pattern around an isolated sphere on the ground plane. Results are shown in Figure 11 and include a horseshoe vortex that is generated at the corner between the frontal face of the sphere and the ground plane and arch vortices that are generated behind the separation line on the sphere. The arch vortices are shed downstream and drop to the ground plane as a result of the strong downwash behind the sphere. Okamoto measured the turbulent wake flow behind the sphere (b = 6 cm) for Re_b = 47,400 in a wind tunnel with a cross section 40 x 40 cm. At a distance of $-z/b$ = 0.5 above the ground plane, the positions of the peak longitudinal velocity defect and the peak turbulence intensities were shifted in the y-direction and were decayed when the downstream distance increased. At x/b = 10 behind the sphere, the longitudinal peak velocity defect decreased with increasing vertical distance above the ground plane, and it almost vanished at $-z/b$ = 1.2. At $-z/b$ < 1.0, the longitudinal turbulence intensity was larger than the lateral and vertical turbulence intensities, but the turbulence became almost isotropic at $-z/b$ = 1.2.

Local Scour at Isolated Obstacles

Local Scour around Bridge Piers Fixed in River Beds

Breusers et al. (1977) made a critical review of the local
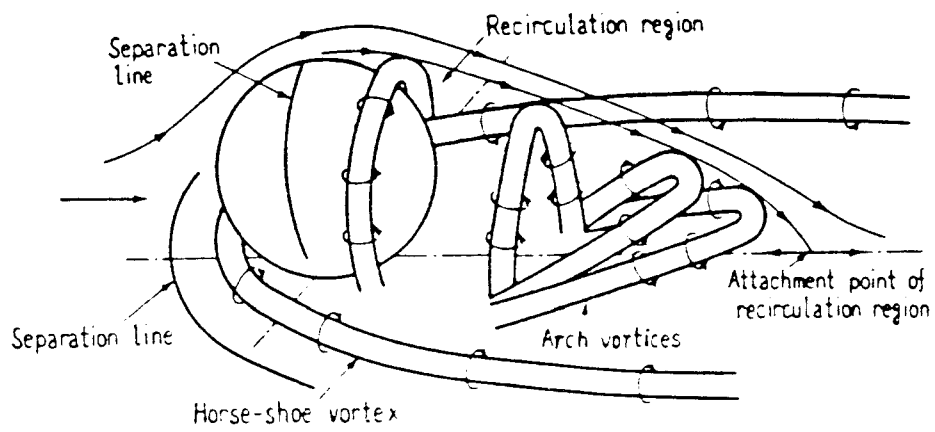
Figure 11.   Flow pattern around an isolated sphere on the ground
plane (Okamoto, 1980).

scour around cylindrical bridge piers. They described the flow field, the scouring processes, and the analysis of relevant parameters. The dominant feature of the flow near a pier was identified as the large eddy structure or system of vortices which developed about the pier. These vortex systems consisted of a horseshoe vortex system, a wake vortex system and/or a trailing vortex system. The horseshoe vortex system was also the dominant feature of scouring processes around the pier. The geometry of the pier was important in determining the strength of the horseshoe vortex. A blunt-nosed pier created a stronger horeshoe vortex than did a sharp-nosed pier. For a circular pier, the rotational velocity in the vortex core was greatest near a point about 70 degrees from the main flow direction. For a square pier, it was greatest near the corners where the vortex was being stretched the most. The scour was initiated there if the scouring potential created by this velocity was strong enough to overcome bed particle resistance to motion. The horseshoe vortex was initially small in cross section and comparatively weak. With the formation of the scour hole, however, the vortex rapidly grew in size and strength as additional fluid attained a downward component and the strength of the down-flow increased. The down-flow acted somewhat like a vertical jet in its ability to erode the bed. As the scour hole enlarged, the circulation associated with the horseshoe vortex increased, but at a decreasing rate. The velocity and the combination of temporary mean bed shear and turbulent agitation at the bed tended to decrease as the scour hole enlarged. This

continued until equilibrium was reached.

According to Breusers et al., the equilibrium depth of scour for a particular bed material and for clear-water scour conditions was a function of the magnitude of the downward flow ahead of the cylinder. This was found to be primarily a function of the diameter of the pier and the magnitude of the approach flow velocity. Although an equilibrium scour depth was obtained ahead of the pier, erosion continued in the downstream dune region. The mound immediately behind the pier was progressively flattened and extended downstream by the flow out of the scour hole.

Breusers et al. categorized the parameters which may influence the scouring phenomenon into four groups, those characterizing (1) the fluid, (2) the bed material, (3) the flow, and (4) the bridge pier. By limiting the analysis to the case of steady uniform flow over a flat bed of uniform non-cohesive natural sediment in a wide channel, they concluded that the relative equilibrium scour depth to pier width (d_{se}/b) at a circular pier was primarily dependent on the relative mean approach flow velocity ($\bar{U}/\bar{U}_c$, where $\bar{U}_c$ is the critical mean approach flow velocity for the incipient motion of the bed material), the relative flow depth to pier width (D/b), and the relative grain size of the bed material to pier width ($\bar{d}/b$).

Clark, et al. (1982) described the local scouring processes around a circular cylinder in a river. The scour began at two points located at 45 degrees to the direction of the flow on the upstream side of the cylinder. Further development of the scour caused two conical scour holes which met at a common point upstream

of the cylinder center and had slopes equal to the angle of repose
of the saturated sediment. This period of scour development was
very rapid and the upper edges of the two scour holes soon merged.
If there was sufficient flow field strength, the next development
was the formation of a conical scour hole at the nose of the
cylinder. As the velocity increased, the scour depth of this scour
hole also increased -- up to the point of incipient motion of the
whole bed. When this live-bed condition occurred, the scour depth
no longer kept increasing with velocity but instead fluctuated about
the maximum value for the clear-water scour. The equilibrium scour
depth developed only after a certain time had elapsed and that depth
was approached only asymptotically. The rate of development of the
scour depended on the geometrical and hydraulic parameters.

Baker (1980) developed a semi-empirical equation to predict the
equilibrium scour depth at a cylindrical bridge pier under
clear-water scour conditions. On the plane of symmetry, he assumed
the horseshoe vortex system within the scour hole to act as a
circular forced vortex: the radius of the horseshoe vortex increased
linearly with the scour depth but the circulation around the vortex
remained approximately constant during scouring. Thus, the
tangential velocity at the edge of the vortex was derived; it was a
function of the approach surface flow velocity, the initial radius
of the horseshoe vortex (r) and the scour depth. He applied this
velocity to calculate the drag forces on an idealized sediment
particle, located beneath the primary horseshoe vortex. The
equilibrium scour depth was derived from the balance of the external

forces on the sediment particle, which was given by:

$$(d_{se}/b) = (r/b) \ (C_1 \ F_d - C_2)$$ \hfill 2.1

where $F_d = U/(\gamma_{sb}\bar{d}/\rho)^{0.5}$, and C_1, C_2 were constants.

He further indicated that the ratio of initial vortex radius to pier width (r/b) depended only upon the relative pier width to water depth (b/D) -- and not upon the flow parameters to any extent. The variation of r/b was represented by

$$(r/b) = C_3 \ \tanh \ (C_4 \ D/b)$$ \hfill 2.2

where C_3, C_4 were constants. For large values of D/b, the r/b value was constant and independent of D/b, while for small values of D/b, r/b was proportional to D/b. Substituting Equation 2.1 into Equation 2.2, the semi-empirical equation of equilibrium scour depth was derived as

$$(d_{se}/b) = (C_5 \ F_d - C_6) \ \tanh \ (C_4 \ D/b)$$ \hfill 2.3

where C_5 and C_6 were constants dependent upon the sediment size and shape.

Qadar (1981) measured the initial radius and the reference velocity at the edge of the primary horseshoe vortex on the plane of symmetry of a bridge pier in a 30 cm wide, 45 cm deep and 5 m long water flume. The bridge piers were 45 cm high, 15 cm long and 2.5 cm to 15 cm wide and had semi-circular streamlined shapes. Two

water depths -- 10 cm and 20 cm -- were used in the experiments.

The initial radius of the primary horseshoe vortex was found to be

0.1 b for b > 2.5 cm. The reference velocity of the primary

horseshoe vortex was a function of the approach flow velocity and

the pier width. It increased as the approach flow velocity

increased but discreased with the pier width. Based upon the

determination that the horseshoe vortex was the basic mechanism

causing local scour, Qadar further related the scour depth to the

initial circulation of the primary horseshoe vortex. He confirmed

this relationship with the model and field experimental data. The

scour depth increased with the initial ciuculation of the horseshoe

vortex.

Chiew and Melville (1987) investigated the relationship between

the local scour depth at a cylindrical pier and the mean approach

velocity of the flow, using a 11.8 m long, 0.44 m wide and 0.38 m

deep water flume and several size of piers. The results of

particular interest are shown in Figure 12 for subcritical flow

($F_r < 1$) with a constant approach water depth of D = 170 mm. Each

data point represents sufficiently long steady-state flow so that

equilibrium scour conditions occurred. For clear-water scour, the

relative equilibrium scour depth to pier width (d_{se}/b) increased

when the relative mean approach flow velocity to the critical mean

approach flow velocity for the incipient motion of the bed material

($\overline{U}/\overline{U}_c$) increased. It reached the first peak at $\overline{U}/\overline{U}_c = 1$, the

condition for the incipient motion of the bed; then it started to

decrease due to live-bed scour ($\overline{U}/\overline{U}_c > 1$). The decrease of d_{se}/b
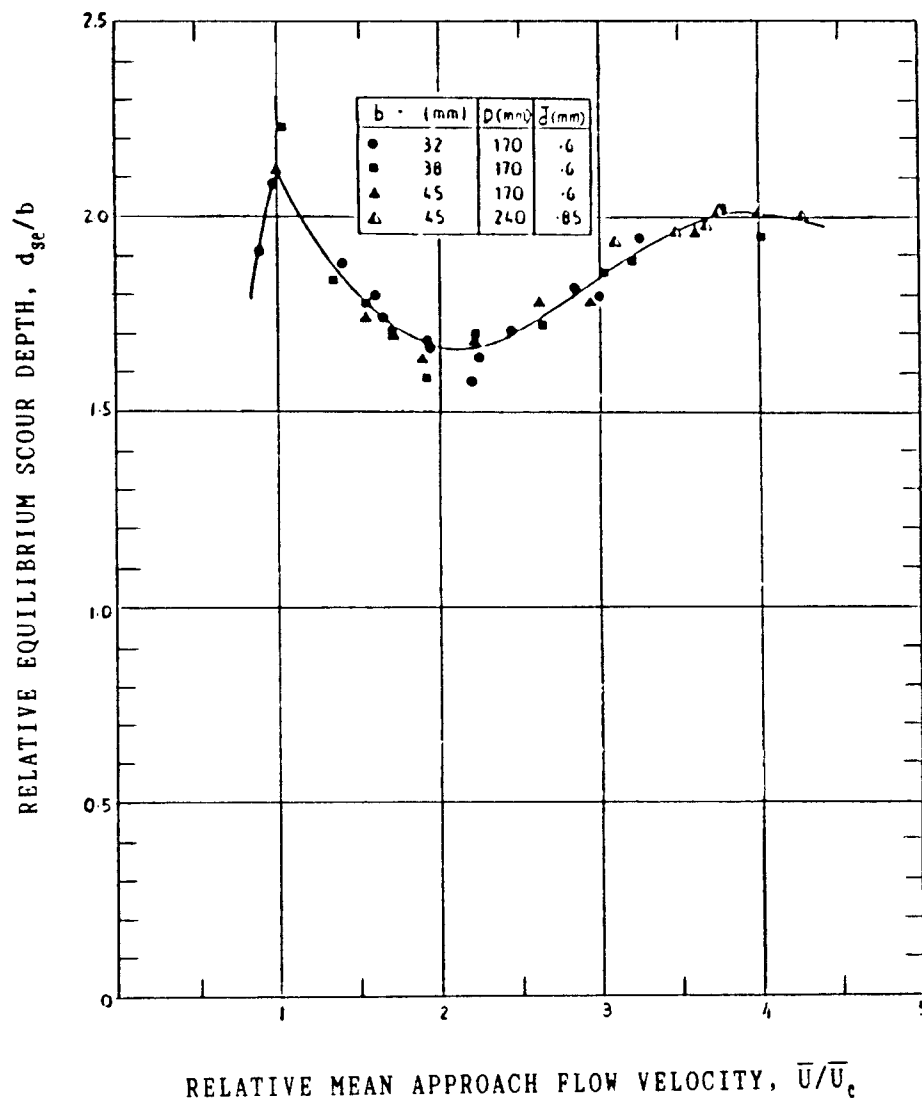
Figure 12. Relative equilibrium scour depth versus relative mean approach flow velocity for various pier sizes, water depths, and bed material sizes (Chiew and Melville, 1987).

continued until a minimum value was reached at $\overline{U}/\overline{U}_c = 2$.

Thereafter, the d_{se}/b increased again, but at a decreasing rate, until a second peak was reached at $\overline{U}/\overline{U}_c = 4$; this corresponds to the condition where a transition flat bed formed. The shape of the curve of d_{se}/b versus $\overline{U}/\overline{U}_c$ was related to the bed features translating past the scour hole.

Chiew and Melville also investigated the effects of relative pier width to sediment size ($b/\overline{d}$) and relative water depth to pier width (D/b) upon the ratio of equilibrium scour depth to pier width (d_{se}/b). The results are shown in Figure 13. For several constant values of $\overline{U}/\overline{U}_c$ and D/b, the d_{se}/b value decreased with decreasing value of $b/\overline{d}$ but became independent of $b/\overline{d}$ when $b/\overline{d}$ became greater than or equal to 50. They used a sediment size adjustment factor K_d, defined as the the ratio of d_{se}/b at a particular $b/\overline{d}$ to the d_{se}/b for $b/\overline{d} > 50$, to account for the influence of the $b/\overline{d}$ value upon the value of d_{se}/b. For clear-water scour at a constant value of $b/\overline{d}$ and with $\overline{U}/\overline{U}_c = 0.9$, they also used a flow depth adjustment factor K_D, defined as the ratio of d_{se}/b at a particular D/b to the d_{se}/b at a large D/b such that the flow depth effect was absent, to account for the influence of the D/b value upon the value of d_{se}/b. The results are shown in Figure 14. The effect of D/b on the depth of the scour was independent of $b/\overline{d}$ when $b/\overline{d}$ was greater than or equal to 50. The K_D value decreased as the D/b value decreased. For $b/\overline{d} < 50$, the results show different functions relating scour depth to D/b for each value of $b/\overline{d}$.
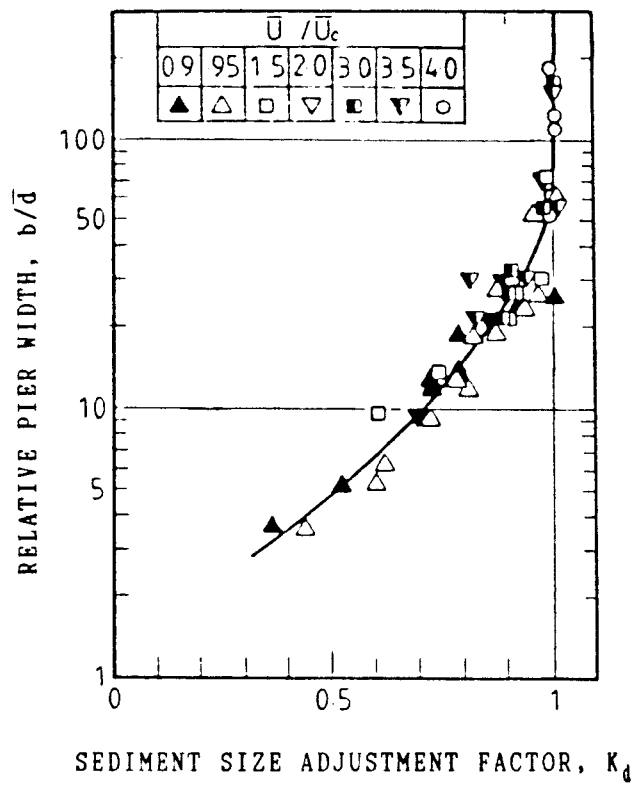
Figure 13. Relative pier width versus sediment size adjustment factor (Chiew and Melville, 1987).
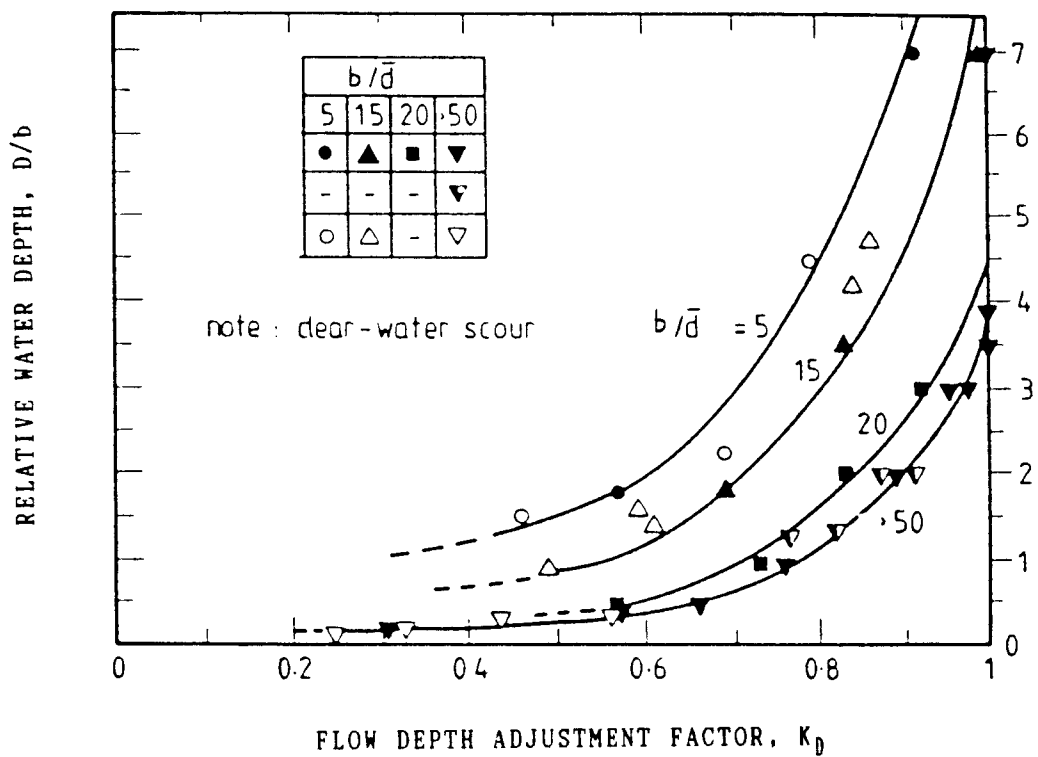
Figure 14.   Relative water depth versus flow depth adjustment factor
             for clear-water scour at $\overline{U}/\overline{U}_c$ = 0.9 (Chiew and
             Melville 1987).

Local Scour at Movable Isolated Obstacles on River Beds

Thomas (1971a, 1971b) studied the equilibrium settlement (vertical sinking) and the time evolution of settlement due to local scour at a circular pier on a river bed. The relative equilibrium settlement to water depth (S_{ze}/D) was found to be a function of the relative approach shear stress to critical shear stress of the bed ($\overline{\tau}_i/\overline{\tau}_c$). The S_{ze}/D ratio increased as the $\overline{\tau}_i/\overline{\tau}_c$ ratio increased in clear-water scour but it decreased as the $\overline{\tau}_i/\overline{\tau}_c$ ratio increased in live-bed scour. The magnitude of the pier load was not a key factor for such settlement. Settlement was increased by the erosive activity of the rotating pier as it was subjected to sand waves and was decreased by the presence of the bedload discharge. Thomas also found that the average rate of change of the scour depth (d_s/t) and the average rate of change of the settlement (S_z/t) at the pier over time t were governed by exponential laws after the initial period of active scour.

Raudkivi and Ettema (1982) identified the stability of an exposed particle of d_1 size seated on a bed composed of particles of size d_2, as shown in Figure 15. Changes in the amount of particle protrusion (P) into the flow influenced the critical shear velocity (u_{*i}) for incipient motion of the exposed particle. Figure 16 shows that increased relative amount of protrusion of the exposed particle (P/d_1) led to a decrease in the critical dimensionless shear stress, θ_{ci}, where

$$\theta_{ci} = u_{*i}^2/[g(S_s-1)d_1]$$

2.4

Flow

$(U, U_*, \overline{\tau}_i)$

particle of size d_l

P

particle of size d_l
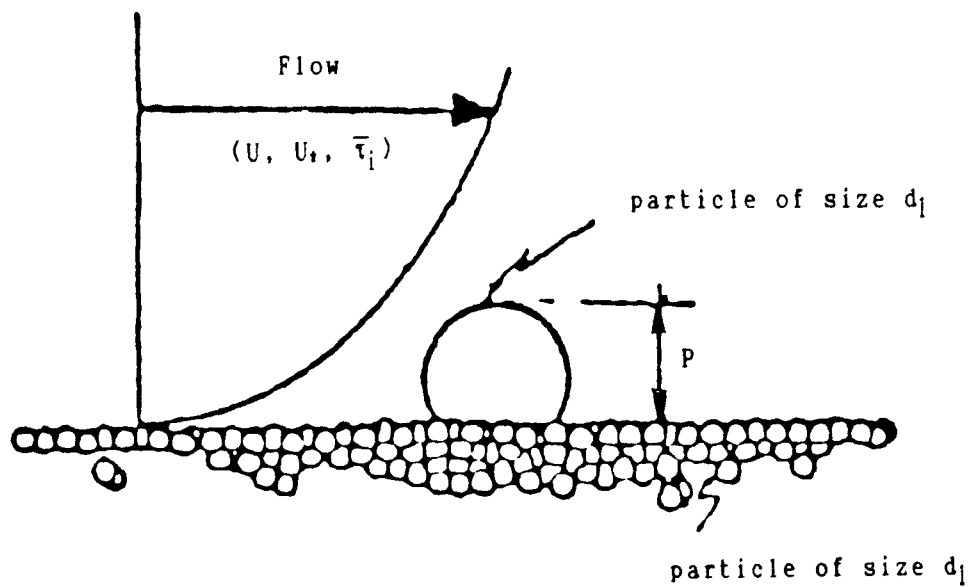
Figure 15.   Definition sketch for an exposed large particle on a
bed of particles of smaller uniform size (Raudkivi and
Ettema, 1982).
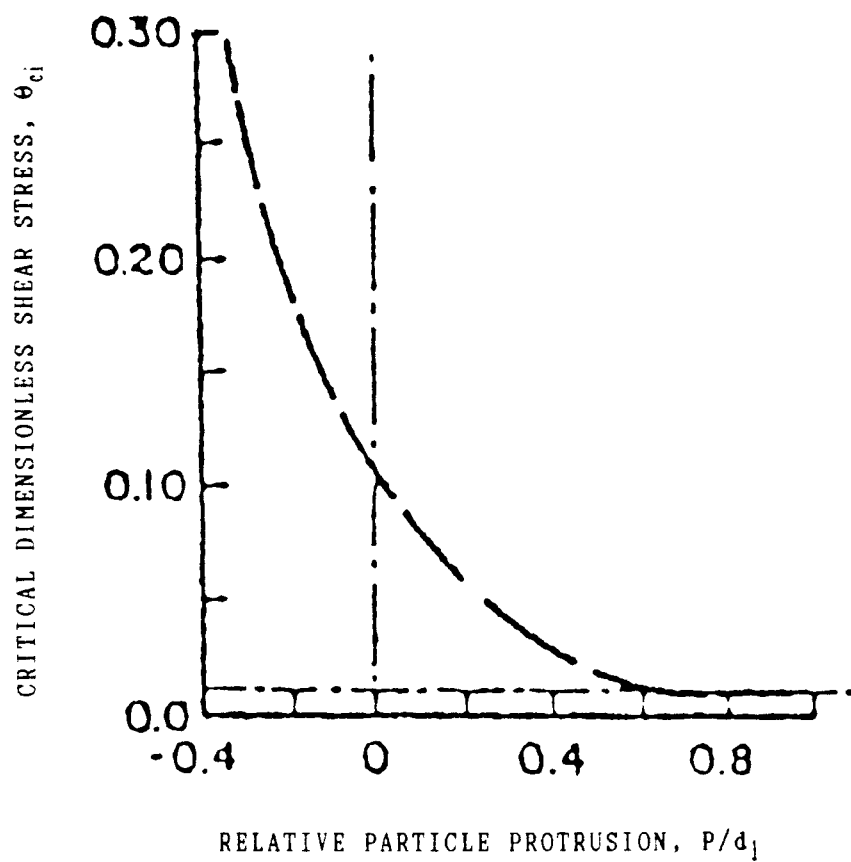
Figure 16. Effect of relative particle protrusion on the critical
dimensionless shear stress for incipient motion of the
exposed particle (Raudkivi and Ettema, 1982).

g is the gravitational acceleration, and S_g is the specific gravity of the particle.

For a particle seated in an almost fully exposed position on the bed surface in a turbulent flow, such that $P/d_1 > 0.6$, the value of θ_{ci} is reduced to $\theta_{ci} = 0.01$.

Raudkivi and Ettema reviewed the work of others which described that a particle seated on a bed surface behaved as an isolated obstacle and shed wake vortices when the value of the particle Reynolds Number, Re_p ($= u_*d_1/\nu$, where u_* is the shear velocity of the flow), were greater than approximately 3.5. The finer-sized bed particles were scoured by the local flow structure around the leading perimeter of the exposed larger particle, and were deposited at its rear. The loss of support at its front and the build-up of particles at the rear caused the larger particle to slide into the scour hole upstream from it and, thus, became embedded amidst the finer particles. As it became embedded, the exposure of the large particle was reduced. They made several conclusions about the behavior of a single d_1 particle on a bed of d_2 particles in the steady uniform flow. These are shown in Figure 17. The domain of u_*/u_{*1} versus d_1/d_2 (u_{*1} is the critical shear velocity for the incipient motion of a surface of d_1 particle) is divided into four regions. In region 1, there is no erosion of any particles. In region 2, there is overpassing of the d_1 particle above the d_2 particles. In region 3, there is embedment of the d_1 particle among d_2 particles. In region 4, there is erosion of all particles. For $u_*/u_{*1} = 0.42$ and for $1 < d_1/d_2 < 5.6$, the fully exposed d_1 particle
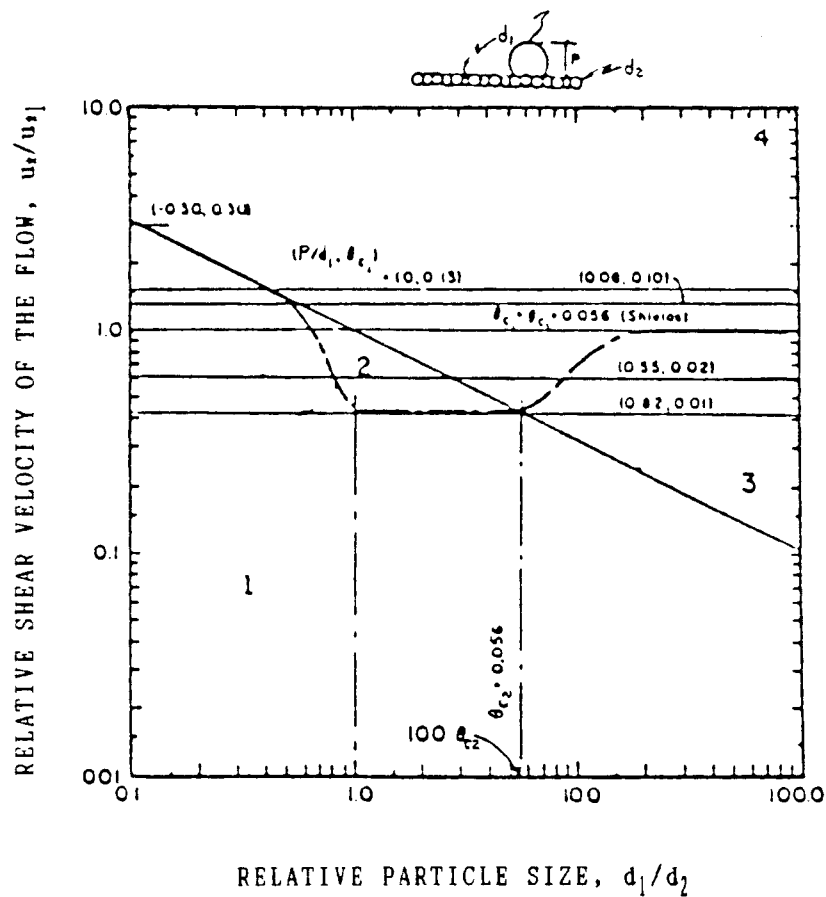
Figure 17. Regions for the behavior of a single d_1 particle on a bed of d_2 particles, assuming 0.056 is the value of the critical dimensionless shear stress of a sediment surface (Raudkivi and Ettema, 1982).

is preferentially entrained in the flow from the bed of d_2 particles, but for $d_1/d_2 > 5.6$, the exposed d_1 particle is no longer entrained. At $d_1/d_2 = 17$, by experimental observation, the d_1 particle became rapidly embedded and only the d_2 particles were entrained.

Fisher (1984) and Fisher and Klingeman (1984) investigated the local scour depth and scour volume at isolated boulders on a river bed. Three natural boulders (width x height x length = 19.35 x 13.01 x 13.96 cm, 26.03 x 16.52 x 22.86 cm, and 15.54 x 10.79 x 13.96 cm; and volume = 1821 cm^3, 5040 cm^3, and 1059 cm^3, respectively), and two kinds of fairly uniform noncohesive sediment bed material ($\bar{d}$ = 1.5 mm and 6.8 mm) were tested in a 106.7 cm wide, 45.7 cm deep and 488 cm long water flume under clear-water scour conditions. A series of profile sections of the scour region were measured for each run. The standard end-area method was used to calculate the net volume of scour below the initial bed surface. Their study confirmed the horseshoe-wake scour pattern as shown in Figure 18, which developed around the boulders. The boulders tended to roll upstream and sink into the resultant scour holes during the progress of local scour. When a boulder was submerged and a sufficient plunge effect was present, a downstream scour pattern developed. For a given flow velocity, the local scour depth was maximized at a single water depth. They expressed the relative equilibrium scour depth to water depth (d_{se}/D) as a function of the Froude Number of the flow (F_r), and related the equilibrium scour volume (V_{se}) to the equilibrium scour depth (d_{se}). The values of
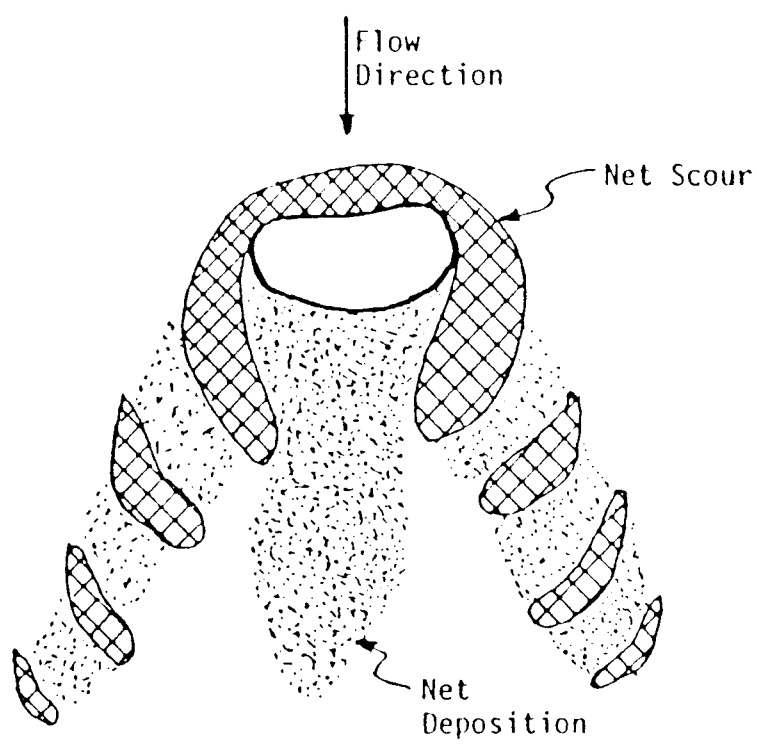
Figure 18. Typical horseshoe-wake scour pattern at a boulder
(Fisher and Klingeman, 1984).

d_{se}/D increased with the value of F_r. Although this led to determining the scour depth without using the size of the proposed boulder and sediment, they noted that additional relationships were needed.

III. ANALYSIS OF THE PROBLEM

Theoretical Background of Local Scour

Laursen (1952) identified three basic general characteristics which should be included in any detailed analysis of local scour in an alluvial channel. These are:

1. the rate of scour will equal the difference between the capacity for transport out of the scoured area and the rate of supply of material to that area;

2. the rate of scour will decrease as the flow section is enlarged; and

3. there will be a limiting extent of scour; this limit will be approached asymptotically.

The first characteristic describes the principle of conservation of mass. The second and third describe the development and achievement of an equilibrium scour condition over time.

The conservation of mass principle can be expressed symbolically by

$$df(B)/dt = g(B) - g(S) \qquad 3.1$$

in which S = sediment supply in the channel; t = time; f(B) = the mathematical description of the boundary, related to channel width B; g(B) = the sediment discharge or transport rate out of the scour zone as a function of the boundary shape and position; and g(S) =

the rate of sediment supply to the scour zone. Here the boundary is defined somewhat arbitrarily and is not necessary equal to the channel width or the scour width but is related to the scour geometry. At present, the functions of $g(B)$ and $g(S)$ can only be predicted by the empirical formulas of sediment transport after the flow fields at the isolated obstacle have been solved.

For quantitative predictions of the scour depth and the obstacle movement induced by local scour, two cases may be considered, based on Equation 3.1. These are: (1) clear-water scour and (2) live-bed scour.

For clear-water scour, $g(B) > 0$, and $g(S) = 0$. For live-bed scour, $g(B) > g(S) > 0$. At equilibrium, when $df(B)/dt = 0$, a limiting extent of scour is reached and the bed and the obstacle are stable. This can happen if $g(B) = 0$ for clear-water scour or if $g(B) = g(S)$ for live-bed scour.

During the local scouring process at an isolated obstacle on a river bed, there may be a loss of lateral support of bed material beneath the obstacle or a direct undermining of bed material by the vortex mechanism. Either of these will cause the obstacle to shift its position upstream, either rotating or sinking, if the static equilibrium of the obstacle has been changed. The time history of the obstacle movement thus greatly depends on the evolution of the scour depth. Once the obstacle changes its position, it will change its exposure to the flow. Hence the original scouring processes will be altered to some degree due to the modification of the flow field. The obstacle will eventually cease its movement when the scour depth at the obstacle reaches equilibrium.

Variables Affecting Scour Depth and Obstacle Movement

In Local Scouring Processes

Several independent variables affect the scour depth and the obstacle movement under steady flow conditions. These can be classified into four groups:

1. The geometric characteristics of the boundary:

    (a) shape (Nc), width (B) and slope (s) of the channel;

    (b) shape (ß), width (b), length (L) and height (h) of the isolated obstacle; and

    (c) angle of attack (θ) of the flow against the obstacle.

2. The hydraulic characteristics of the flow: the depth (D) and average velocity ($\bar{U}$) of the approach flow, and time (t) of the local scour.

3. The characteristics of the fluid: density (ρ), specific weight (γ) and kinematic viscosity (ν) of the fluid.

4. The characteristics of the erodible bed material and the isolated obstacle: mean size ($\bar{d}$), standard deviation (σ), submerged specific weight (γ'_{sb}) and cohesiveness (c) of the sediment, and submerged specific weight (γ'_{so}) of the obstacle.

The dependent variables of the problem are: local scour depth (d_s) and local scour volume (V_s) at the obstacle, displacement (S_i, where i = x, y and z) of the obstacle, as described here for a point at the center of the obstacle top surface, and obstacle inclination ($\Delta\theta_{ij}$, which equals the difference of θ_{ij} at time t and and at time

zero, where i = x, y and z; j = x' and z'), as described here by means of the unit tangent vector and unit normal vector at the obstacle top surface. Here θ_{ij} is the angle from the i axis at time zero to the j axis at time t. Several of these variables are shown in Figure 19.

The whole problem of local scour and obstacle movement can be expressed as a function:

$$d_s, V_s, S_i, \Delta\theta_{ij} = f\ (Nc, B, s, \beta, b, L, h, \theta, D, \bar{U}, t, \rho, \gamma, \nu, \bar{d}, \sigma, \gamma'_{sb}, c, \gamma'_{so})\qquad 3.2$$

This problem is very complicated if all the variables involved in the local scouring process are considered. Some assumptions must be made in order to reduce the number of variables and reduce the problem to one that can be reasonably analyzed. These assumptions are:

1. the channel near the obstacle is plain and straight;

2. the channel width is far greater than the obstacle width;

3. approach flow incidence is normal to the obstacle width;

4. flow is uniform, and

5. the erodible bed material consists of uniform and noncohesive sand and/or gravel.

Thus, the Equation 3.2 can be reduced to:

$$d_s, V_s, S_i, \Delta\theta_{ij} = f\ (\beta, b, l, h, D, \bar{U}, t, \rho, \gamma, \nu, \bar{d}, \gamma'_{sb}, \gamma'_{so})\qquad\qquad 3.3$$
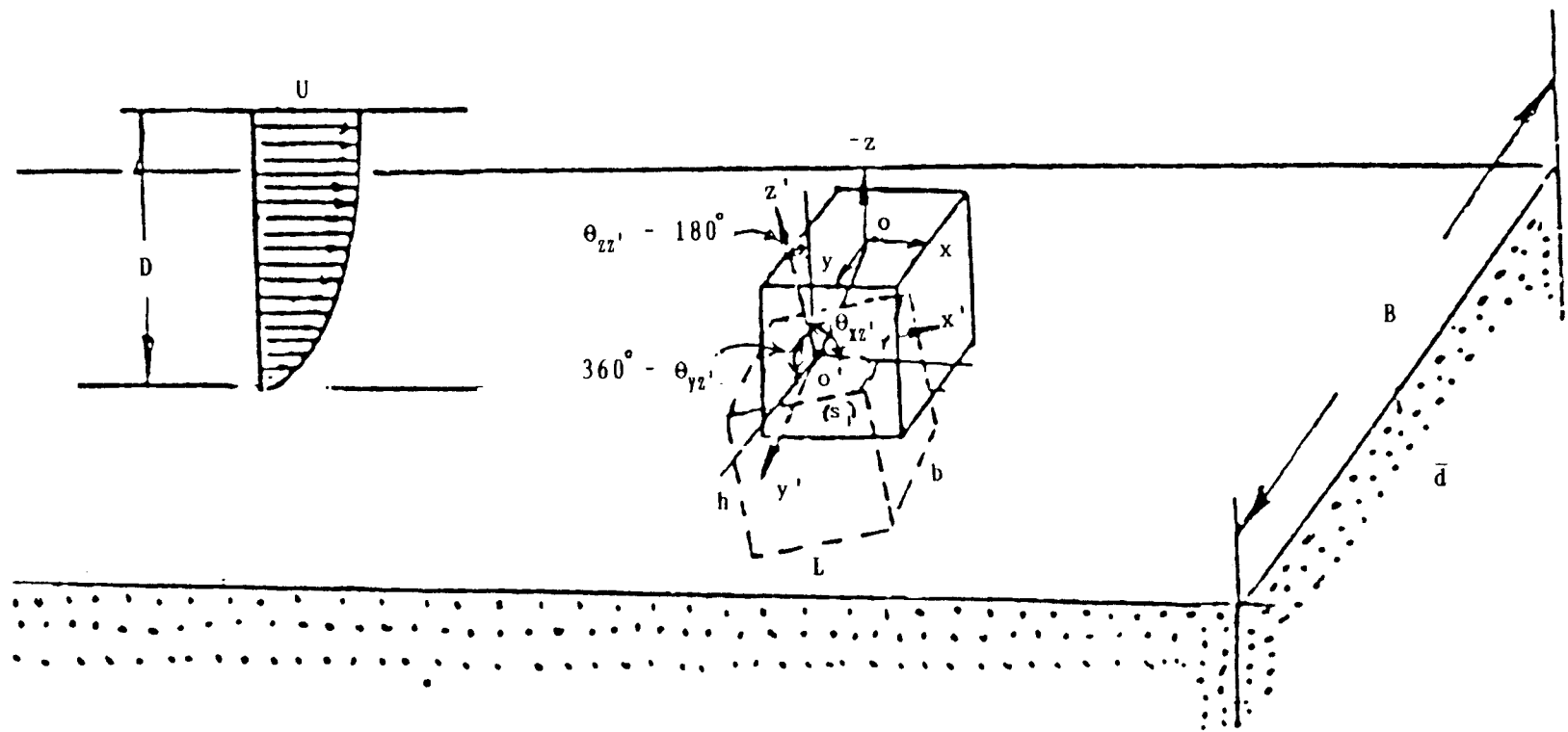
Figure 19. Definition sketch for some of the variables describing obstacle movement in local scour.

Dimensional Analysis of Local Scour

A systematic way of collecting, analyzing and presenting data is necessary in order to organize experimental work and minimize the time and effort for a complicated problem. Dimensional analysis is a first step toward this end. The obtained dimensionless groups can be used as the similarity laws for a scaled model. Then the experimental results can be applied to a full-scale model. The Buckingham π Theorem provides a widely-used approach for this analysis. The problem variables include the three basic dimensions of length, mass and time. Hence, three repeating variables must be selected for full analysis of all terms.

For the problem of local scour, let ρ, $\bar{U}$, D be the repeating variables. Equations 3.3 can be nondimensionalized as:

$$d_s/D,\ V_s/D^3,\ S_i/D,\ \Delta\theta_{ij} = f\ [\beta,\ b/D,\ L/D,\ h/D,\ \bar{U}t/D,\ \gamma D/(\rho\bar{U}^2),\ \nu/(\bar{U}D),$$
$$\bar{d}/D,\ \gamma'_{sb}D/(\rho\bar{U}^2),\ \gamma'_{so}D/(\rho\bar{U}^2)]\qquad 3.4$$

Equations 3.4 can be rearranged to have more physical sense as:

$$d_s/D,\ V_s/D^3,\ S_i/D,\ \Delta\theta_{ij} = f\ [\beta,\ b/D,\ L/D,\ h/D,\ \bar{U}t/D,\ \bar{U}/\sqrt{gD},\ \bar{U}D/\nu,\ \bar{d}/D,$$
$$\bar{U}/\sqrt{\gamma'_{sb}\bar{d}/\rho},\ \bar{U}/\sqrt{\gamma'_{so}b/\rho}]\qquad 3.5$$

Here, g is the gravitational acceleration and links ρ and γ through Newton's Second Law of Motion (force = mass x acceleration).

The physical significance of the above dimensionless groups is described as follows:

1. d_s/D is the relative scour depth with respect to the water depth.

2. V_s/D^3 is the relative scour volume with respect to the water volume which can be given in terms of D^3.

3. S_i/D is the relative displacement at the center of the obstacle top surface with respect to the water depth.

4. $\Delta\theta_{ij}$ is the inclination of the obstacle in terms of the angles, as shown in Figure 20.

5. β is the shape factor of the obstacle. It affects the curvature of streamlines and points of flow separation, hence also the scour depth and the obstacle movement. According to Breusers et al. (1977), a blunt-nose obstacle creates a stronger horseshoe vortex system than does a sharp-nose obstacle.

6. b/D is the relative obstacle width with respect to the water depth. It greatly affects the location and the dimension of flow separation at the obstacle. According to Breusers et al. (1977), Baker (1980) and Qadar (1981), the scour depth is determined primarily by the horseshoe vortex and the vortex dimensions are dependent upon the obstacle width to a large extent.

7. L/D is the relative obstacle length with respect to the water depth. It affects the flow separation and reattachment on both sides of the obstacle, hence affecting the dimension of wake vortices. According to Gowda et al. (1983), on obstacle that is slender in length can also

reduce the width of the horseshoe vortex on both sides of the obstacle and, to some extent, its downstream length.

8. h/D is the relative obstacle height with respect to the water depth. Acording to Adamek (1968), for a cube with $h/D < 1/4$, the free water surface above the cube was hardly affected by the changes of the flow condition. The h/D is important because it measures the depth of flow which affects scour and obstacle movement. Eckman and Nowell (1984) identified that the h/D affected the intensity of the horseshoe vortex and the skin friction force on the bed at the obstacles.

9. $\bar{U}t/D$ expresses similarity in the time evolution of local scour and obstacle movement. This parameter can be eliminated if the equilibrium state of local scour is considered.

10. $\bar{U}/\sqrt{gD}$ is the Froude Number (F_r) of the flow and expresses the ratio of inertia forces to gravity forces. The Froude Number is important whenever the effect of gravity is significant and, in particular, where a free surface is present.

11. $\bar{U}D/\nu$ is the Reynolds Number (Re) of the flow and expresses the ratio of inertia forces to viscous forces. When the bed materials are coarse or the flow is fully turbulent in open channel flow, viscous effects will not be significant and the Reynolds Number can be neglected.

12. $\bar{d}/D$ is the relative roughness of the bed material with

respect to the water depth. It is essentially linked to the preceeding group of variables (the Reynolds Number) and is necessary in order to define the vertical velocity profile and the bed shear stress given by the mean velocity of the approach flow. According to Peterka et al. (1985), a rougher boundary upstream causes the wake to disappear more quickly and the evidence of the horseshoe vortex in the wake to diminish.

13. $\bar{U}/(\gamma_{sb}\bar{d}/\rho)^{0.5}$ and $\bar{U}/(\gamma_{so}'b/\rho)^{0.5}$ are variants of the well-known Shields parameter for incipient motion of the bed particles and the obstacle ($F_{\bar{d}}$ and F_b, respectively), in which the shear velocity is replaced by the mean flow velocity (Jain and Fischer, 1980). The Shields parameter greatly affects the nature of the time evolution of scour depth and obstacle movement. Since the γ_{sb}' value is nearly a constant in alluvial sand and/or gravel bed rivers, if the obstacle is limited to a single specific gravity, then the $F_{\bar{d}}$ and F_b values are constant ratios of F_r and can be replaced by the F_r value for the given flow velocity and water depth.

The preceding interpretation may provide a little insight into the phenomenon of local scour.

When the flow is fully turbulent over a rough boundary and when only those obstacles with constant specific gravity and equivalent width, length and height are considered, Equation 3.5 can be reduced to

$$d_s/D, \ V_s/D^3, \ S_i/D, \ \Delta\Theta_{ij} = f \ (\beta, \ b/D, \ \bar{U}t/D, \ F_r, \ \bar{d}/D) \qquad 3.6$$

If only the equilibrium state of local scour is to be considered, Equations 3.6 can be further reduced to

$$d_{se}/D, \ V_{se}/D^3, \ S_{ie}/D, \ \Delta\Theta_{ije} = f \ (\beta, \ b/D, \ F_r, \ \bar{d}/D) \qquad 3.7$$

Equation 3.7 will be used to guide the design of the experimental research work that is discussed in the following chapters of this dissertation.

IV. EXPERIMENTAL STUDIES

Overview of Experimental Plan

The complex nature of local scour has hindered its analysis and has made experimental studies necessary. Flume study offers an experimental approach which can provide a better controlled environment for the large number of influencing parameters involved in local scour. Flume investigation can be used for improving the physical understanding of the processes and quantifying the variables of interest.

In this research, a series of movable-bed experiments were conducted on local scour at some isolated obstacles on sand/gravel beds. The desired variables of interest were maximum scour depths, scour volumes, and induced obstacle movements. Prior to these movable-bed experiments, a few fixed-bed experiments were conducted to learn about the mean flow field at the obstacle. All tests were performed in a flume located in the Hydraulic Laboratory of Oregon State University.

Experimental Apparatus

The flume system is shown in Figure 20. The flume used was 8.23 m long with a rectangular cross section 46 cm wide and 61 cm deep. It was constructed of plexiglass and aluminum and could be tilted. A flow straightener and a wave damper near the flume
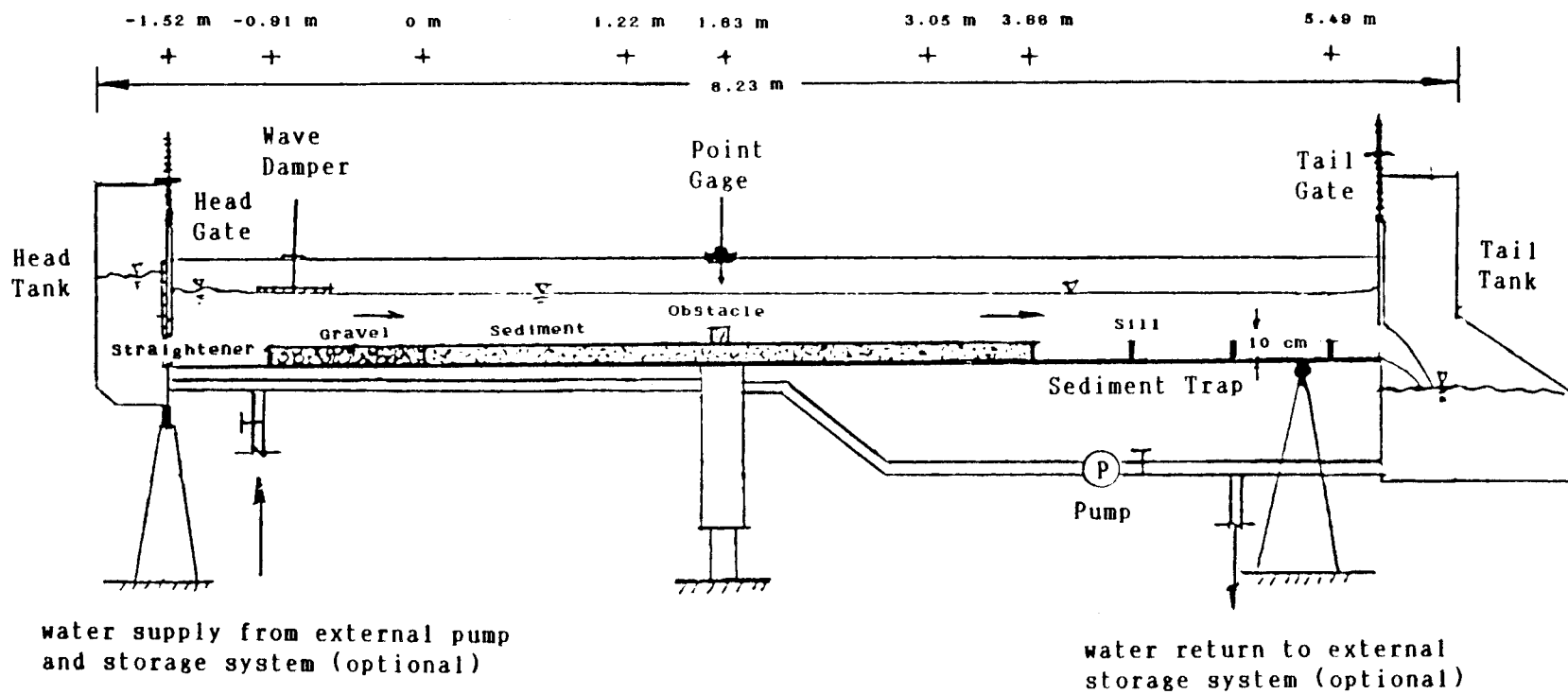
Figure 20. Flume system used for experiments.

entrance dampened the excess flow disturbance from the head tank. The flume floor contained a 91 cm long gravel bed extending downstream from a point at a distance of 61 cm downstream from the head gate; this bed was part of the flow "approach" section. Continuing from this section was a 3.66 m long test section filled with sediment, followed by three consecutive 61 cm long sediment traps. Each trap was divided with a 10 cm high wood sill. The plexiglass sides of the flume permitted visual observations and the recording and photographing of changes in conditions in the test section.

The hydraulic system control consisted of a water storage tank, pump, head tank, head gate, flume, tailgate and tail tank. The flume could be used with a recirculating pump (Figure 20) or as a throughflow system (external pump and storage tank not shown in Figure 20). The throughflow system provided larger discharges and was used for this research. The water depth and velocity in the flume were controlled by a combination of pump speed, pump discharge valve setting, flume slope and tailgate height at the outlet. Discharge was determined by measuring the total weight of water flowing into a volumetric tank during a measured time interval. The maximum discharge of this hydraulic system is 26 liters per second (l/s).

A point gage with 0.3 mm accuracy was mounted on a carriage travelling on the edges of the flume and was used to measure the bed and water surface profile and the obstacle movements. A Nover Nixon streamflow prob 403 mini propeller current meter of 1% velocity

accuracy was connected to the point gage to measure the water velocity at the obstacle. The propeller had a diameter of 11.6 mm and was composed of fine blades mounted on a hard stainless steel spindle.

Aluminum cubes, circular cylinders (aspect ratio h/b = 1) and spheres with specific gravity of 2.79 were used as the testing obstacles. The cube sizes were 2.54 cm (1.00 inch), 5.08 cm (2.00 inch), 7.62 cm (3.00 inch) and 10.16 cm (4.00 inch); the circular cylinders and spheres had diameters of 5.08 cm (2.00 inch) and 7.62 cm (3.00 inch). The cube, circular cylinder and sphere were used as the testing obstacles because of their simple geometries and basic shapes among the countless obstacle shapes in nature. The cube was further chosen as the major testing obstacle in the experiments because of the larger flow obstruction it offered, as compared to that of the circular cylinder and the sphere. The circular cylinder and sphere were tested for comparision to reveal the effect of obstacle shape.

The bed material used in the experiments was of two types: medium sand ($\bar{d}$ = 0.39 mm) and very fine gravel ($\bar{d}$ = 3.0 mm), each with specific gravity of 2.60. The grain size distributions for these bed materials are shown in Figure 21.

Experimental Design

The experimental design of the flume study was based on the dimensional analysis of the problem summarized by Equation 3.7 (see

Figure 21. Grain size distributions of the flume sediment.
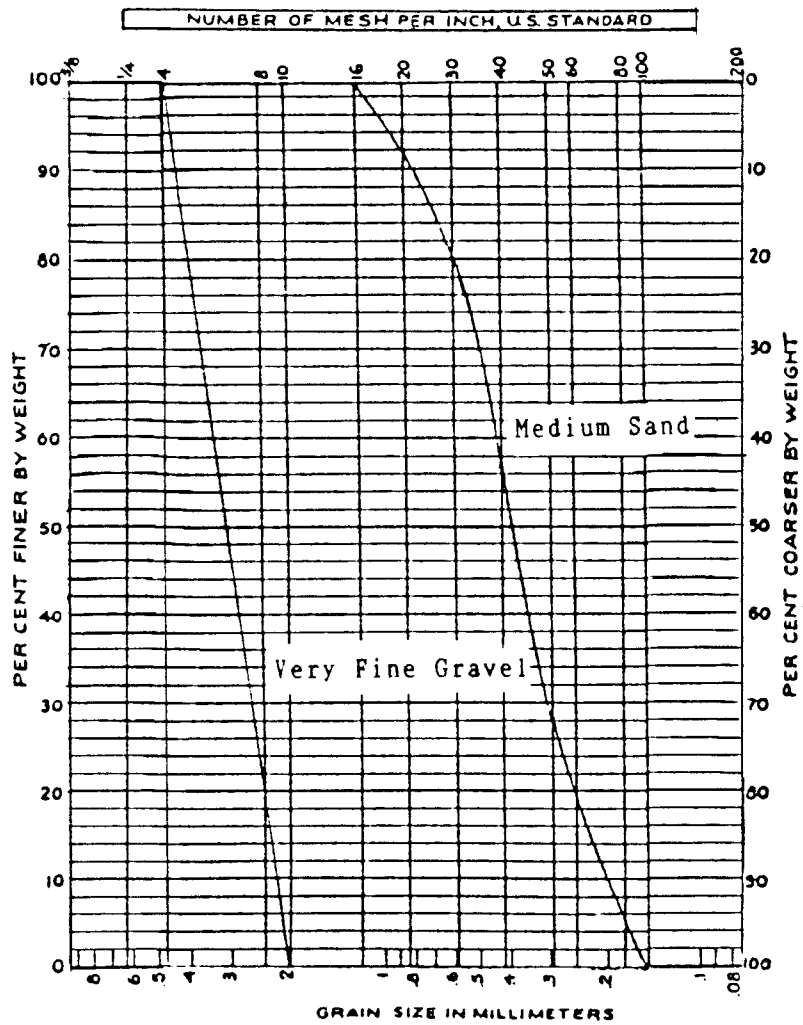
chapter 3). This investigation was limited to the clear-water scour case. Study scope was also limited by the nature of the available experimental apparatus, mainly its limited size for large-scale study of obstacles. The measurements were mainly focused on the maximum scour depth, the scour volume and the induced obstacle movement at an isolated cube on a flat bed under steady upstream flow conditions.

Prior to the intensive series of movable-bed experiments, a few fixed-bed experiments were designed to reveal the mean flow field at the obstacle. This is shown in Table 1. Figure 22 gives a definition sketch for the symbols used. Fixed-bed tests are identified by the symbol "CU" for cube, "CY" for circular cylinder and "SP" for sphere. Experiments were performed with the 7.62 cm (3 inch) obstacles. Due to the symmetric property of the obstacle, measurements were limited to the mean horizontal velocity distributions at the right half-plane of the obstacle near the bed. This velocity is intimate with the movement of bed material. The water surface profiles and mean horizontal velocity distributions on the plane of symmetry were also measured to indicate the changes of the flow fields due to the flow obstruction caused by the obstacle.

Table 2 shows the experimental design for the movable-bed experiments. The definition sketch for symbols used in table 2 is shown in Figure 22. For movable-bed tests, the symbols "C", "Y" and "S" used with the run numbers identify the obstacle shape: cube (C), circular cylinder (Y) and sphere (S). There are a total of forty four runs in Table 2. Among these, runs C1 to C34 were tests with

Table 1. Experimental design for fixed-bed experiments.

Obstacle Shape	Run No.	b (cm)	D (cm)	Ū (cm/s)	Q (l/s)	Fr	b/D
Cube	CU1	7.62	15.24	24.44	17.05	0.20	0.50
	CU2	7.62	9.52	19.35	8.44	0.20	0.80
	CU3	7.62	3.81	12.22	2.12	0.20	2.00
	CU4	7.62	9.52	43.56	19.00	0.45	0.80
	CU5	7.62	3.81	27.50	4.79	0.45	2.00
Cylinder	CY	7.62	9.52	43.56	19.00	0.45	0.80
Sphere	SP	7.62	9.52	43.56	19.00	0.45	0.80
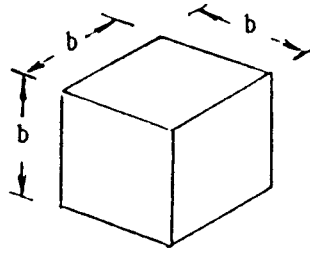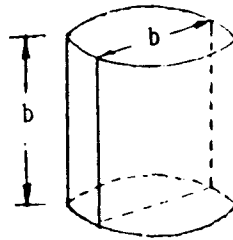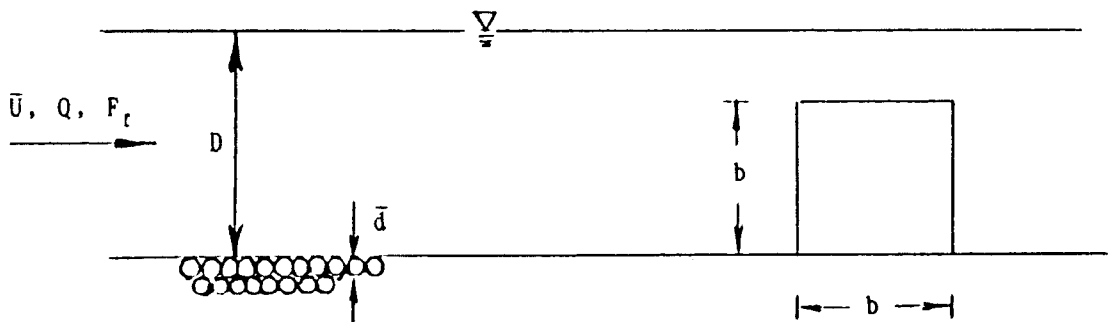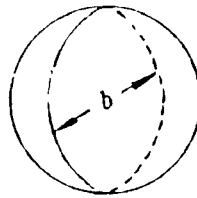
Figure 22. Definition sketch for symbols used in Tables 1 and 2.

cubes, Y1 to Y4 were tests with a circular cylinder, and S1 to S3
were tests with a sphere. The b/D values ranged from 0.25 to 4.0.
The F_r values ranged from from 0.1 to 0.8. The $\bar{d}/D$ values ranged
from 0.13 x 10^{-2} to 11.81 x 10^{-2}. Among the cube experiments (runs
C1 to C34), C1 to C17 were tests with a medium sand bed and C18 to
C34 were tests with a very fine gravel bed. The designed
experiments systematically considered the individual effects of each
independent dimensionless parameter (e.g., C2, C7 and C17 for b/D;
C29, C32 and C34 for F_r; C5, C9 and C16 for $\bar{d}/D$.) or the effects of
two independent dimensionless parameters at a time (e.g., C5 to C8
for b/D and $\bar{d}/D$) on the dependent dimensionless parameters shown in
Equation 3.7.

<div align="center">Experimental Procedures</div>

In the fixed-bed experiments, the selected obstacle was placed
in midstream of the flume on a flat medium sand bed that had been
previously fixed in place with a thin layer of cement. The water
surface profiles and the mean horizontal velocity distributions were
measured at the desired locations under the designed steady flow
conditions. The thin layer of cement was removed after the
fixed-bed experiments were finished. Then the series of movable-bed
experiments were initiated.

The basic procedures followed in conducting the movable-bed
experiments were as follows:

1. Establish a flat, smooth bed 10 cm deep. Carefully fill
the flume to at least a 15 cm water depth above the sediment bed by

Table 2. Experimental design for movable-bed experiments.

Obstacle Shape	Bed Material	Run No.	$\bar{d}$ (mm)	b (cm)	D (cm)	$\bar{U}$ (cm/s)	Q (1/s)	Fr	b/D	$\bar{d}$/D
Cube	Sand	C1	0.39	2.54	3.81	12.22	2.12	0.20	0.67	1.02E-02
		C2	0.39	2.54	7.62	17.28	6.03	0.20	0.33	5.12E-03
		C3	0.39	5.08	10.16	9.97	4.64	0.10	0.50	3.84E-03
		C4	0.39	5.08	20.32	14.14	13.14	0.10	0.25	1.92E-03
		C5	0.39	5.08	2.54	9.84	1.16	0.20	2.00	1.54E-02
		C6	0.39	5.08	5.08	14.12	3.28	0.20	1.00	7.68E-03
		C7	0.39	5.08	7.62	17.28	6.03	0.20	0.67	5.12E-03
		C8	0.39	5.08	10.16	19.96	9.26	0.20	0.50	3.84E-03
		C9	0.39	7.62	3.81	12.22	2.12	0.20	2.00	1.02E-02
		C10	0.39	7.62	7.62	17.28	6.03	0.20	1.00	5.10E-03
		C11	0.39	7.62	9.52	19.35	8.44	0.20	0.80	4.09E-03
		C11A	0.39	7.62	11.43	21.18	11.07	0.20	0.67	3.41E-03
		C11B	0.39	7.62	15.24	24.44	17.05	0.20	0.50	2.56E-03
		C12	0.39	10.16	10.16	9.97	4.64	0.10	1.00	3.84E-03
		C13	0.39	10.16	20.32	14.14	13.14	0.10	0.50	1.92E-03
		C14	0.39	10.16	30.48	17.28	24.10	0.10	0.33	1.28E-03
		C15	0.39	10.16	2.54	9.84	1.16	0.20	4.00	1.54E-02
		C16	0.39	10.16	5.08	14.14	3.28	0.20	2.00	7.68E-03
		C17	0.39	10.16	7.62	17.28	6.03	0.20	1.33	5.12E-03
	Gravel	C18	3.00	2.54	3.18	25.08	3.62	0.45	0.80	9.45E-02
		C19	3.00	5.08	5.08	21.21	4.93	0.30	1.00	5.91E-02
		C20	3.00	5.08	10.16	29.93	13.90	0.30	0.50	2.95E-02
		C21	3.00	5.08	15.24	36.70	25.57	0.30	0.33	1.97E-02
		C22	3.00	5.08	2.54	22.46	2.60	0.45	2.00	1.18E-01
		C23A	3.00	5.08	6.35	35.51	10.28	0.45	0.80	4.72E-02
		C23B	3.00	5.08	6.35	35.51	10.28	0.45	0.80	4.72E-02
		C24	3.00	5.08	10.16	44.93	20.84	0.45	0.50	2.95E-02
		C25	3.00	5.08	2.54	39.93	4.64	0.80	2.00	1.18E-01
		C26	3.00	5.08	5.08	45.93	10.70	0.65	1.00	5.91E-02
		C27	3.00	5.08	7.62	47.55	15.56	0.55	0.67	3.94E-02
		C28	3.00	7.62	9.52	43.56	19.00	0.45	0.80	3.15E-02
		C29	3.00	10.16	5.08	21.21	4.93	0.30	2.00	5.91E-02
		C30	3.00	10.16	10.16	29.93	13.90	0.30	1.00	2.95E-02
		C31	3.00	10.16	15.24	36.70	25.57	0.30	0.67	1.97E-02
		C32	3.00	10.16	5.08	31.82	7.39	0.45	2.00	5.91E-02
		C33	3.00	10.16	10.16	44.93	20.84	0.45	1.00	2.95E-02
		C34	3.00	10.16	5.08	45.93	10.70	0.65	2.00	5.91E-02
Cylinder	Sand	Y1	0.39	5.08	2.54	9.84	1.16	0.20	2.00	1.54E-02
		Y2	0.39	5.08	5.08	14.12	3.28	0.20	1.00	7.68E-03
		Y3	0.39	5.08	10.16	19.96	9.26	0.20	0.50	3.84E-03
	Gravel	Y4	3.00	5.08	6.35	35.51	10.28	0.45	0.80	4.72E-02
Sphere	Sand	S1	0.39	5.08	5.08	14.12	3.28	0.20	1.00	7.68E-03
		S2	0.39	5.08	10.16	19.96	9.26	0.20	0.50	3.84E-03
	Gravel	S3	3.00	5.08	6.35	35.51	10.28	0.45	0.80	4.72E-02

introducing water from the downstream end of the flume. Place the selected obstacle on the sediment bed in midstream and normal to the flow, as shown in Figure 23.

2. Establish a steady uniform flow over the sediment bed at the desired water depth, velocity and/or discharge. Measure the water level at the locations 61 cm upstream and 122 cm downstream of the obstacle and measure the water temperature. If the desired water depth cannot be established under the given flow discharge, the sediment bed slope must be adjusted.

3. Carefully measure the position of the obstacle at the center of its top surface during the test.

4. Remeasure the discharge, water level and water temperature at the end of each run, when no significant change of the obstacle movement can be observed.

5. Stop the flow and drain most of the flume water slowly; then measure the position of the obstacle based on four preselected points on its surface. These are points 0, 1, 2 and 3 shown in Figure 24.

6. Place contour line markers along the water marks in the scour hole around the obstacle with 0.2 mm thick threads at each desired increment of water level for the residual flume water, removing incremental amounts of water to produce the desired change of water level. The water levels in the scour hole were well controlled by the water levels in two artificially dug holes in the bed at approximately 1 m distance upstream and downstream of the obstacle, as shown in Figure 25. Then document the scour pattern at

Figure 23. Preparation of the movable bed experiment with filling
water and the installed obstacle.

Cube

Flow ⟶

1

0

2   3
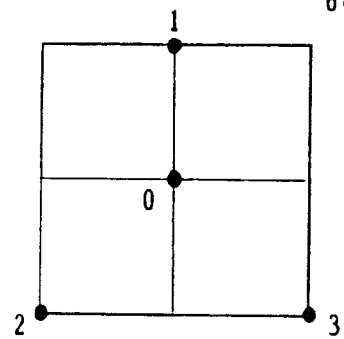
Top View

Circular Cylinder

Flow ⟶

1

2   0

3
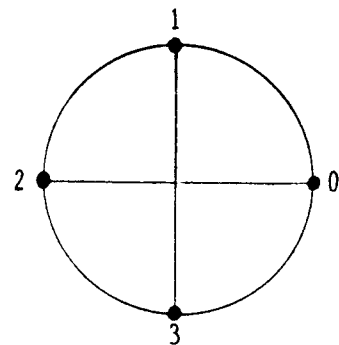
Top View

Sphere

Flow ⟶

2   1 3   0

45 45
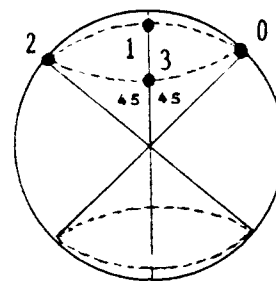
Side View

Figure 24. Four pre-selected points on the obstacle for the
measurement of obstacle movement (before scouring).

Figure 25.   Control of the water level in the scour hole for
            measurement of scour pattern at the obstacle.

the obstacle with photos.

7. Carefully cover the scour hole and the obstacle with a piece of 0.3 mm thick water-proof, transparent drop cloth. Then slowly pour water into the plastic until it completely conforms to the shape of the scour hole. Measure the scour volume at the obstacle based on the volume of water retained by the filled plastic drop cloth in the scour hole, as shown in Figure 26.

8. Remove the water and drop cloth from the scour hole carefully; then remove the obstacle and measure the maximum scour depth in front of the obstacle.

Measurements of the water surface, bed surface and obstacle movement were made from an established datum above the flume. Position coordinates were based on a horizontal grid system, with X corresponding to the longitudinal position, Y corresponding to the lateral position, and Z corresponding to the vertical position (the point gage reading). The measured coordinates of four preselected points on the obstacle were then used to calculate the displacement and the inclination of the obstacle.

(Note: replicate runs 23A and 23B produced nearly identical scour patterns. This demonstrated the repeat ability of the experimental results.)

Figure 26   Measurement of the scour volume at the obstacle with given volume of filled water.

V. DISCUSSION OF EXPERIMENTAL RESULTS

Flow Fields for Fixed Beds

Water surface profiles and longitudinal velocity profiles along the plane of symmetry are shown in Figure 27 for the experimental runs in Table 1 (see chapter 4). In these figures, distances from the obstacle and from the fixed bed to any point in the flow are normalized with the obstacle width. Velocities are normalized with the approach mean velocity. The supporting data are given in Tables B-1 to B-4 of Appendix B.

These figures all indicate that the approaching flow is retarded in front of the obstacle. The lower part of the flow, approaching near the bed, is retarded earlier than the upper part of the flow. These figures also indicate that the flow separates and creates a back flow immediately behind the obstacle. The separated flow reattaches downstream but only gradually recovers to the profile of the upstream approach flow.

In Figure 27(a) to 27(c) (runs CU1 to CU3), the flow Froude Number, F_r, is constant at 0.20. These figures indicate that for cubes the successive decrease of relative water depth (D/b) from 2.0 to 1.25 to 0.5 leads to increased values of relative longitudinal velocity (u/Ū) upstream but decreased values near the bed downstream of the cube. The shapes of the velocity profiles downstream of the cube also change. When the value of the downstream relative distance x/b is greater than 4.0, the location of the maximum
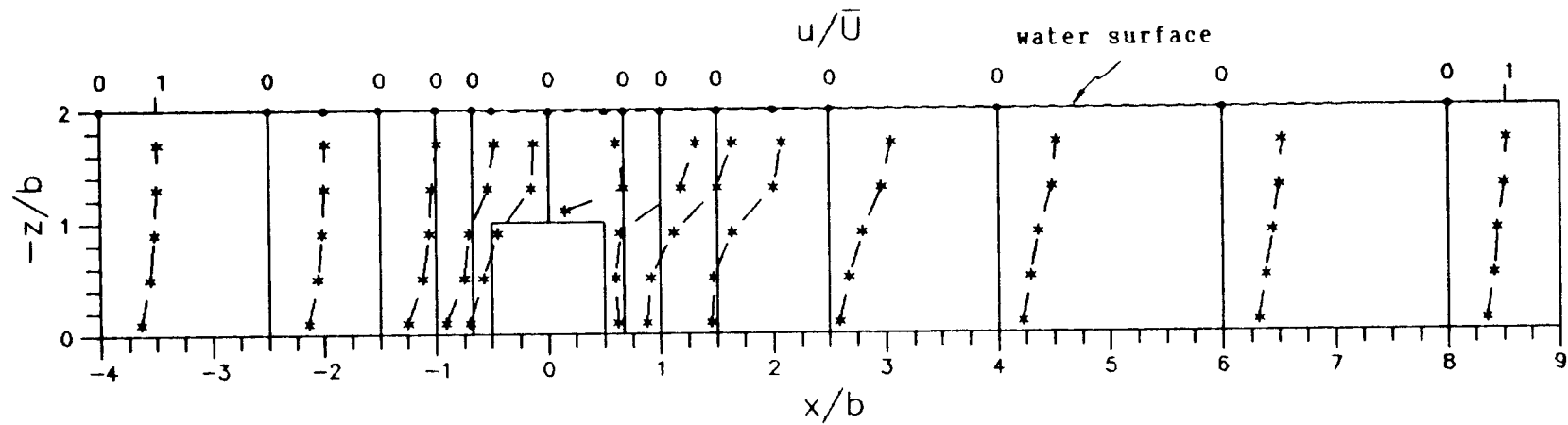
(a) run CU1
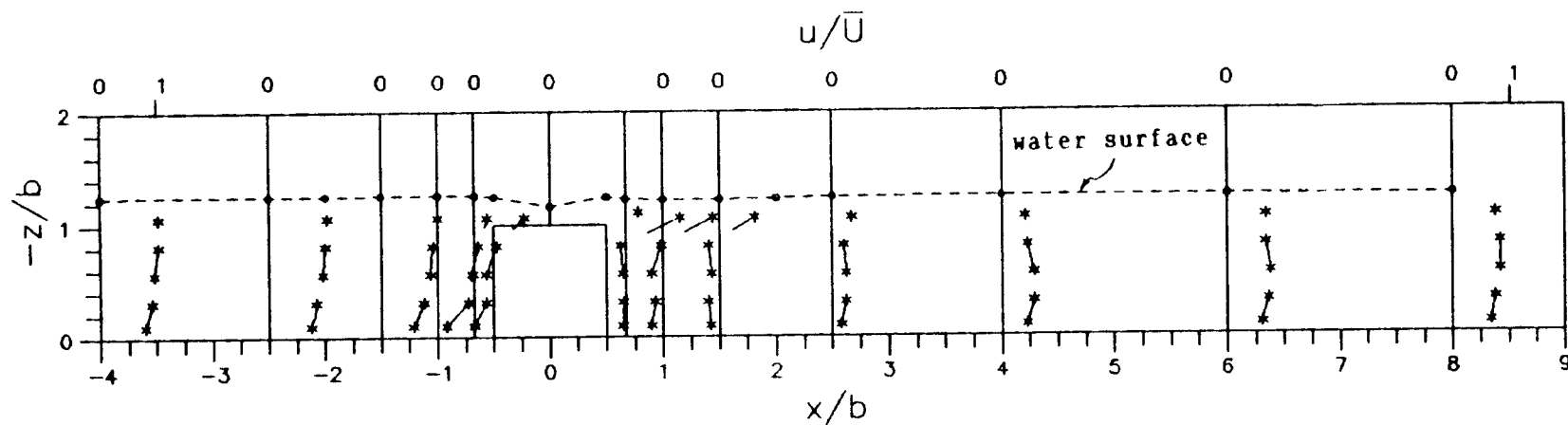
(b) run CU2

Figure 27. Water surface and longitudinal velocity profiles on planes of symmetry of cube, circular cylinder and sphere during fixed-bed runs CU1-to-CU5, CY and SP. (Note: flow is from left to right)
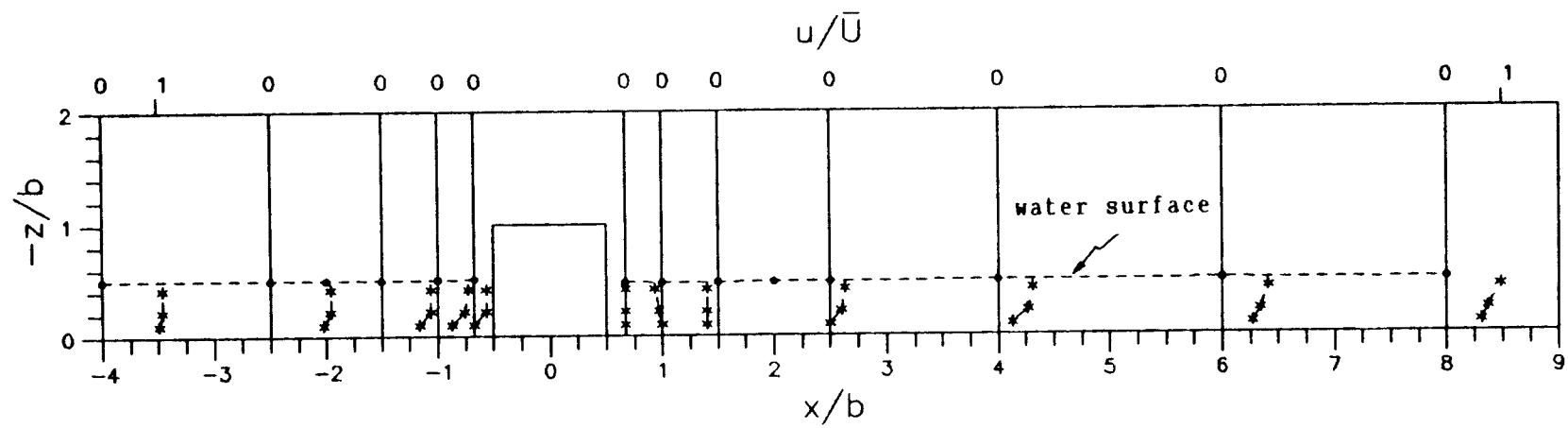
(c) run CU3
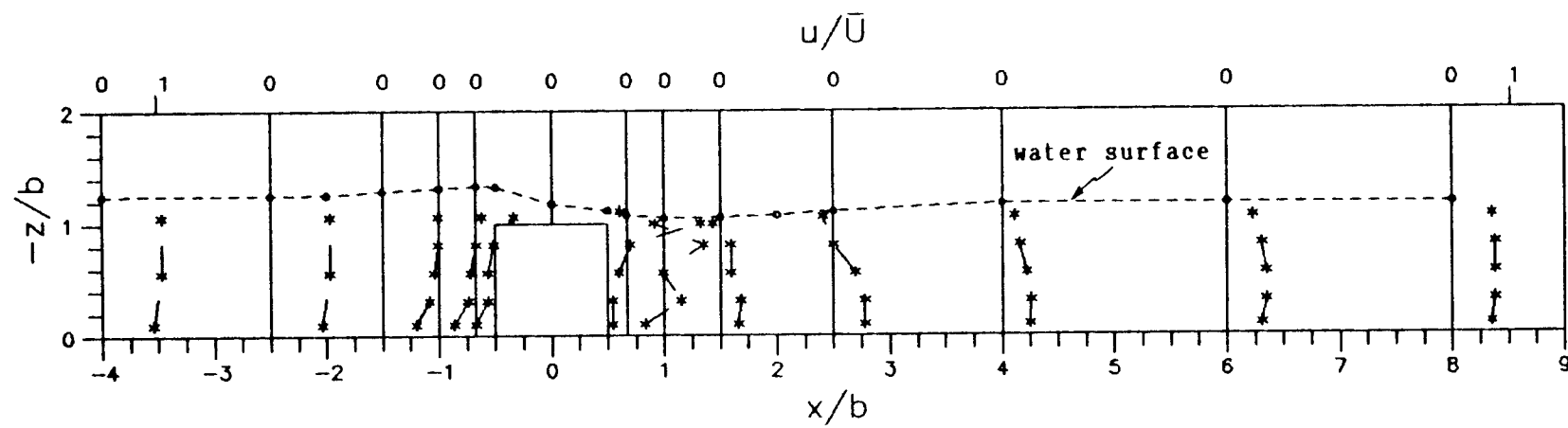
(d) run CU4

Figure 27. Continued.

(e) run CU5

(f) run CY

Figure 27.   Continued.

(g) run SP
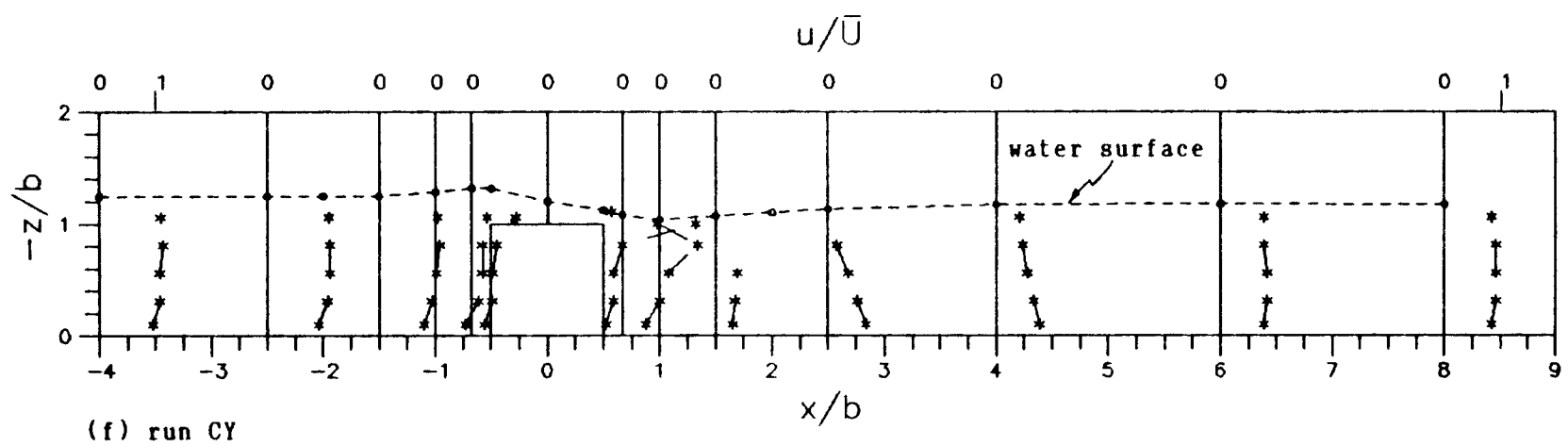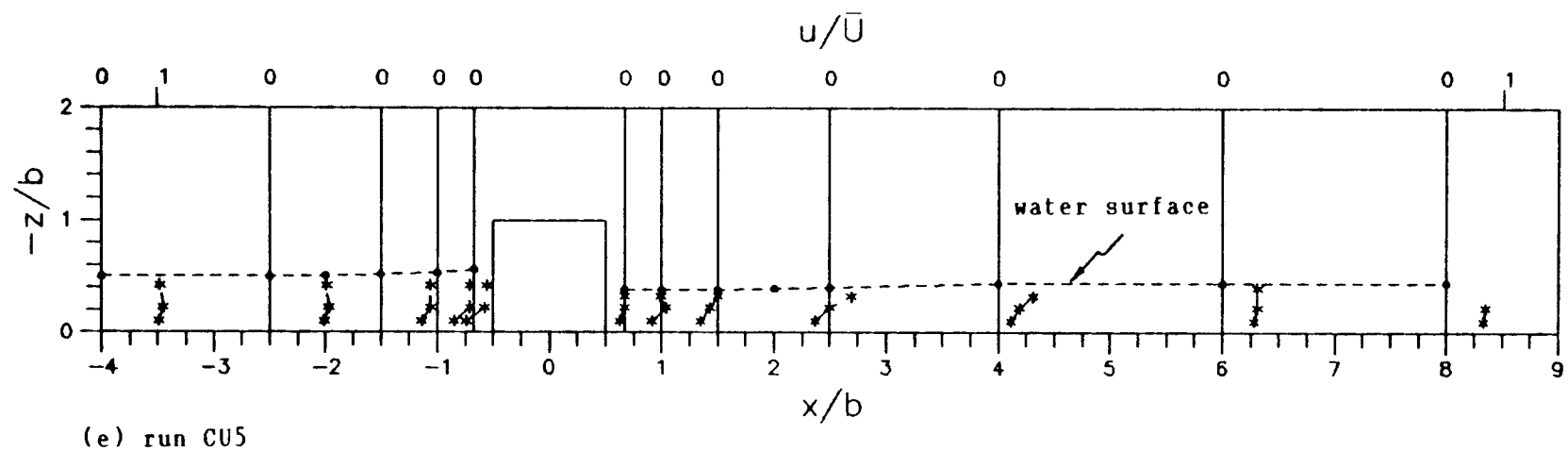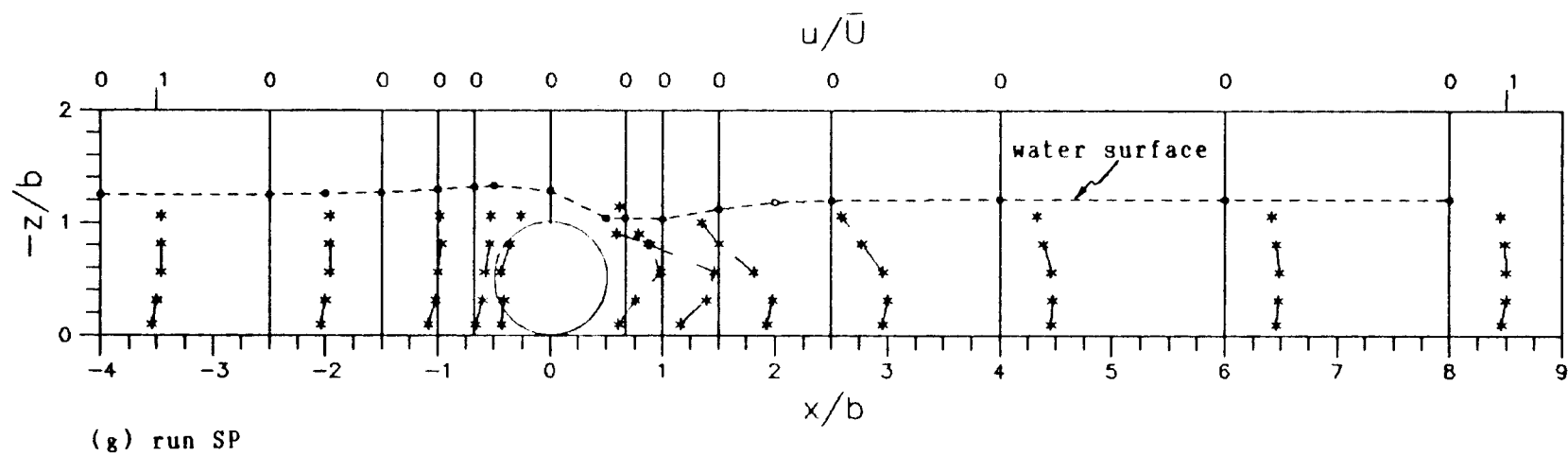
Figure 27. Continued.

velocity for each velocity profile is near the water surface in
Figure 27(a) and 27(c) (well-submerged cube and exposed cube). For
the slightly submerged cube in Figure 27(b), the maximum velocity
moves into the lower part of the flow at x/b = 4.0. At greater
distance downstream, the maximum velocity tends to move upward
toward the water surface.

The water surface profiles do not change significantly with the
decrease of relative water depth at F_r = 0.20, except that there is
a slight depression of the water surface on the cube in Figure 27(b)
for D/b = 1.25.

In Figure 27(d) and 27(e) (runs CU4 and CU5), the flow Froude
Number is constant at F_r = 0.45 but the relative water depth (D/b)
changes from 1.25 to 0.5. The influence of relative water depth
(D/b) upon the longitudinal veloocity profiles (u/$\bar{U}$) is similar to
that at F_r = 0.20. But the increase of the flow Froude Number
causes a significant change of the water surface profile. This is
shown in Figure 28. The water depths along the plane of symmetry
(D_x) are normalized with the approach water depth. The results are
listed in Table 3. The backwater effects all start at a point about
2.5 b upstream of the cube. Water surface drops occurred in runs
CU4 and CU5 between x = -0.67 b and x = 1.0 b; these drops are
0.23 D and 0.36 D, respectively. At relative water depth
D/b = 1.25, the increase of the flow Froude Number from 0.20 to 0.45
causes the water surface depression on the cube to become lower and
move farther downstream. It then leads to a small hydraulic jump at
x = 1 b behind the cube, which creates a back flow near the water
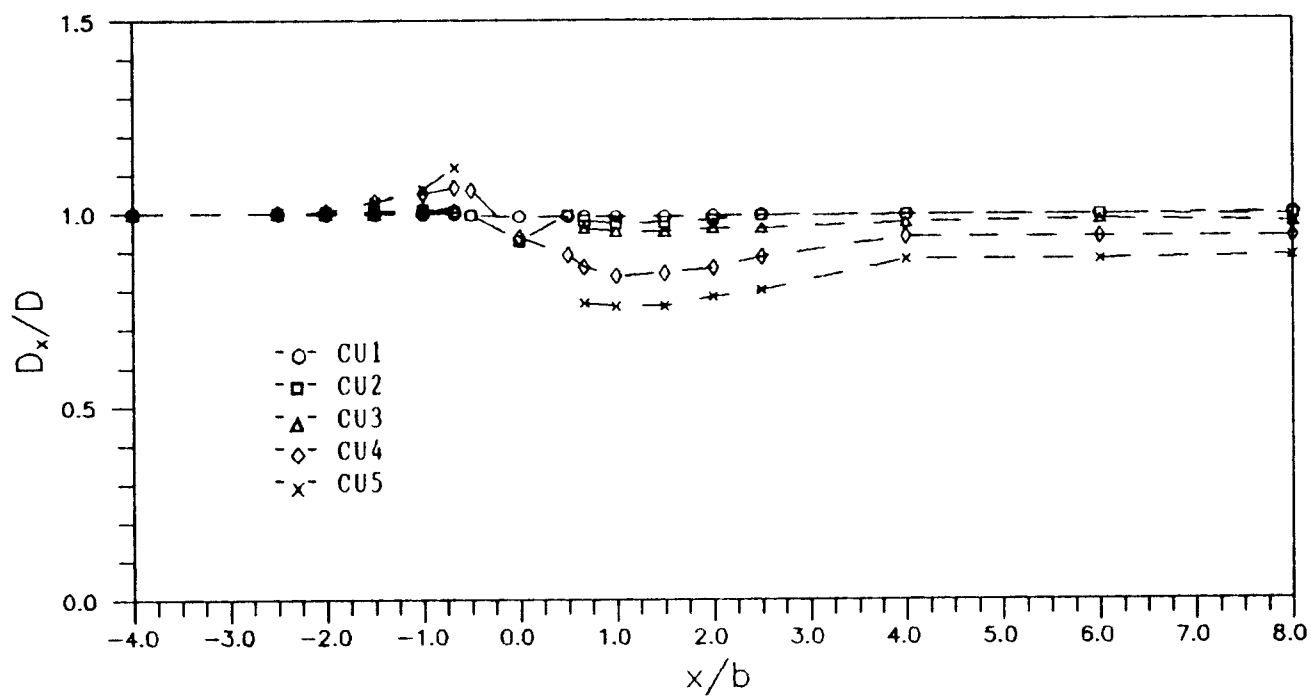
Figure 28. Comparison of water surface profiles on the plane of
symmetry of cube during fixed-bed runs CU1 to CU5.
(Note: flow is from left to right)

Table 3. Water depths along planes of symmetry of cube, circular
cylinder and sphere during runs CU1-to-CU5, CY and SP.

Run No.	CU1	CU2	CU3	CU4	CY	SP	CU5
x/b	D_x/D	D_x/D	D_x/D	D_x/D	D_x/D	D_x/D	D_x/D
-8.00	1.002	1.006	1.016	1.016	1.003	1.023	1.024
-4.00	1.000	1.000	1.000	1.000	1.000	1.000	1.000
-2.50	1.000	1.003	1.000	1.003	1.000	1.000	1.000
-2.00	0.998	1.003	1.000	1.006	1.000	1.007	1.008
-1.50	1.000	1.006	1.000	1.032	1.000	1.013	1.032
-1.00	1.000	1.010	1.008	1.052	1.029	1.036	1.064
-0.67	1.000	1.006	1.016	1.068	1.055	1.056	1.120
-0.50	0.996	0.997		1.061	1.055	1.063	
0.00	0.992	0.929		0.939	0.961	1.026	
0.50	0.992	0.997		0.893	0.899	0.828	
0.67	0.992	0.981	0.961	0.861	0.864	0.831	0.768
1.00	0.992	0.974	0.953	0.838	0.831	0.825	0.760
1.50	0.992	0.977	0.953	0.845	0.857	0.894	0.760
2.00	0.994	0.984	0.961	0.858	0.883	0.944	0.784
2.50	0.996	0.994	0.961	0.887	0.906	0.957	0.800
4.00	0.996	0.996	0.976	0.939	0.938	0.967	0.880
6.00	0.996	0.997	0.984	0.939	0.942	0.964	0.880
8.00	1.000	0.994	0.976	0.939	0.938	0.964	0.888
12.00		0.994	0.976	0.939	0.935	0.964	0.880
16.00	0.998	1.000	0.992	0.939	0.938	0.964	0.888

surface between x = 1 b and 2.5 b. The reattachment length of the flow is reduced but the relative velocity $(u/\bar{U})$ near bed is increased in this region. This is shown in Figure 27(d), as compared to Figure 27(b).

The simultaneous increase of relative water depth and flow Froude Number, from D/b = 0.5 and F_r = 0.20 to D/b = 1.25 and F_r = 0.45, causes significant changes of the water surface and longitudinal velocity profiles. The comparision of Figure 27(c) and 27(d) (runs CU3 and CU4) indicates these changes. In Figure 27(d), the downstream relative longitudinal velocity $(u/\bar{U})$ near bed is significantly increased due to the severe change of the water surface of the hydraulic jump behind the cube.

Figure 27(d), 27(f) and 27(g) (runs CU4, CY and SP) indicate the obstacle shape effect upon the water surface and longitudinal velocity profiles at D/b = 1.25 and F_r = 0.45. They have similar shapes of water surface and longitudinal velocity profiles. There is no significant increase of the relative water depth (D_x/D) in front of the obstacle due to the change of obstacle shape. The relative water depth (D_x/D) of the cube and the circular cylinder are very close but it is significantly increased on the top and downstream of the sphere within x = 4 b. These are shown in Figure 29. The location of the hydraulic jump of the sphere is closer to the obstacle than those for the circular cylinder and the cube. The jump decreases the flow reattachment length of the sphere. When the obstacle shape is changed from cube to circular cylinder or sphere, the approaching flow is less retarded. The value of the relative
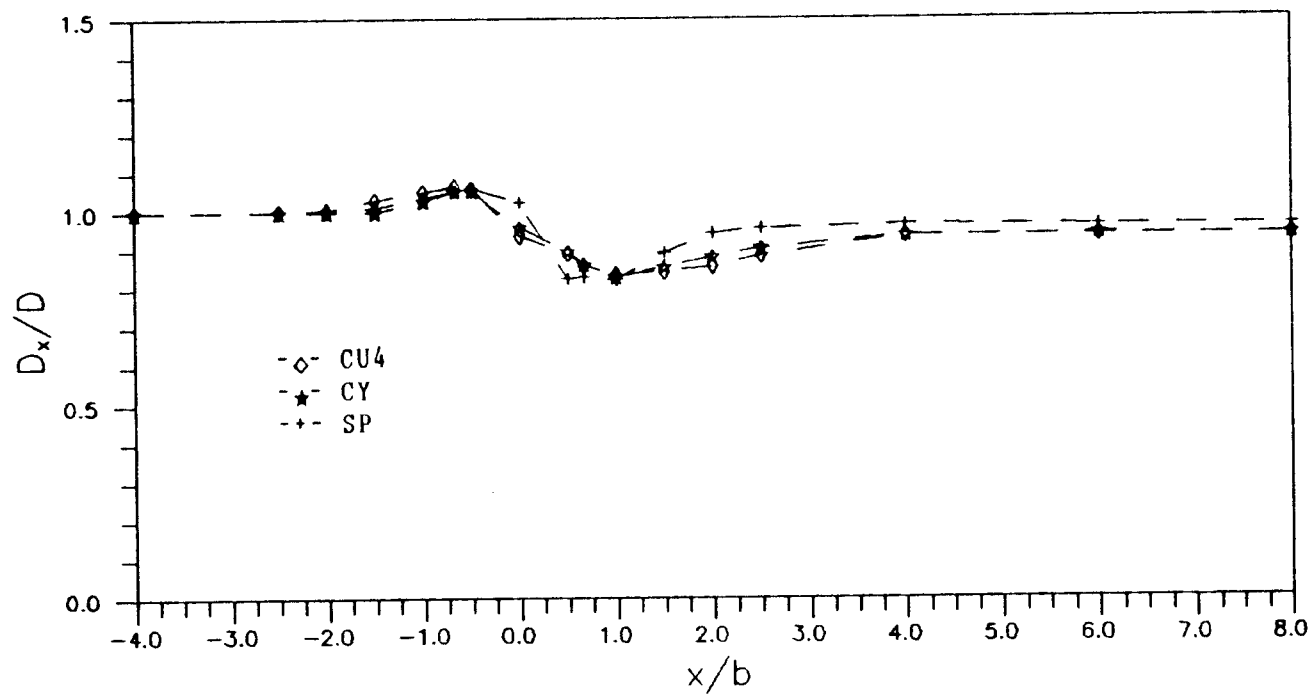
Figure 29. Comparison of water surface profiles on planes of symmetry of cube, circular cylinder and sphere during runs CU4, CY and SP. (Note: flow is from left to right)

longitudinal velocity profiles $(u/\bar{U})$ in front of the obstacle is
increased significantly. The change of obstacle shape also
increases the value of the lower part of the relative longitudinal
velocity profiles $(u/\bar{U})$ downstream of the circular cylinder and the
sphere between x = 1 b and 8 b. The sphere has the highest value of
$u/\bar{U}$.

The distributions of the horizontal velocity (V) near the bed
at -z/b = 0.1 for the experimental runs in Table 1 are shown in
Figure 30. In these figures, the longitudinal and lateral distances
from the obstacle are normalized with the obstacle width, and the
velocity is normalized with the approach flow velocity (u) at
-z = 0.1 b. The results are listed in Tables B-5 to B-11 of
Appendix B. These figures are shown in three-dimensional plots with
the right half plane from the obstacle removed and with the relative
horizontal velocity (V/u) as the third dimension . Each figure is
viewed from the downstream right side with the figure rotated sixty
degrees horizontally and tilted forty five degrees vertically. A
local increase of the horizontal velocity is represented by a
protrusion on the surface. These increases occurred closely around
the obstacle. A significant local decrease of the horizontal
velocity occurred immediately in front of and behind the obstacle.
The distribution of the horizontal velocity farther downstream of
the obstacle tends to recover to the upstream approach flow
velocity. In Figures 30(a) to 30(c) (runs CU1 to CU3), the flow
Froude Number is constant at F_r = 0.20. The decrease of relative
water depth (D/b) from 2.0 to 0.5 leads to increased average
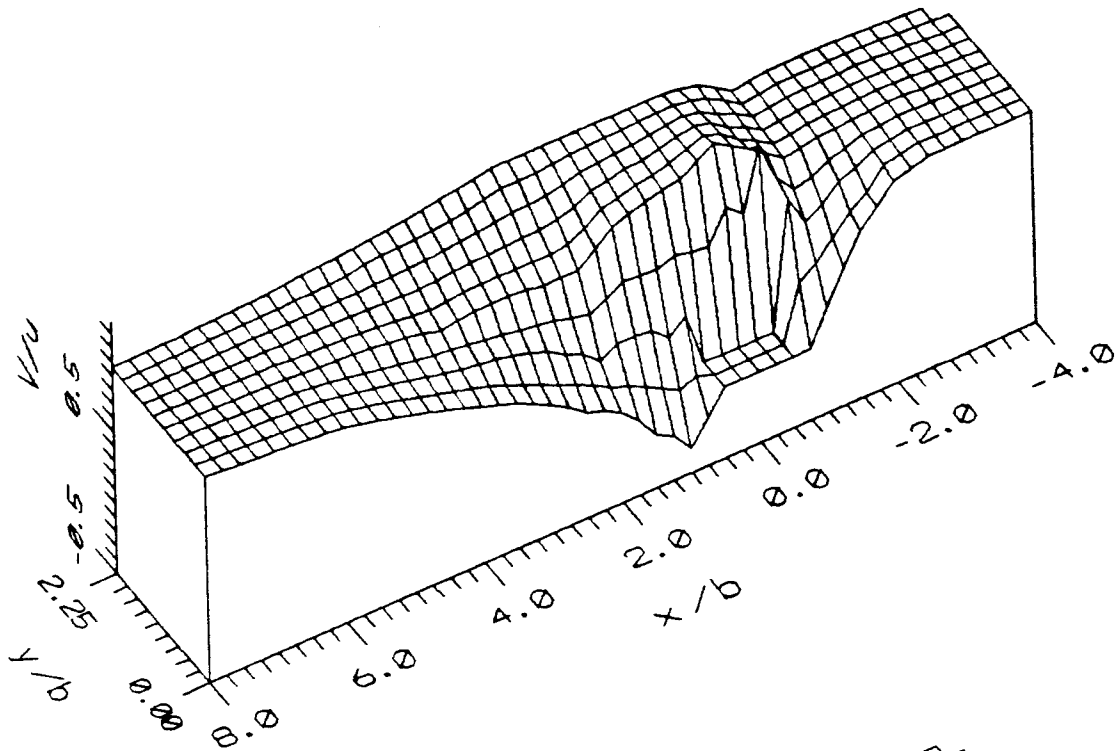
(a) run CU1
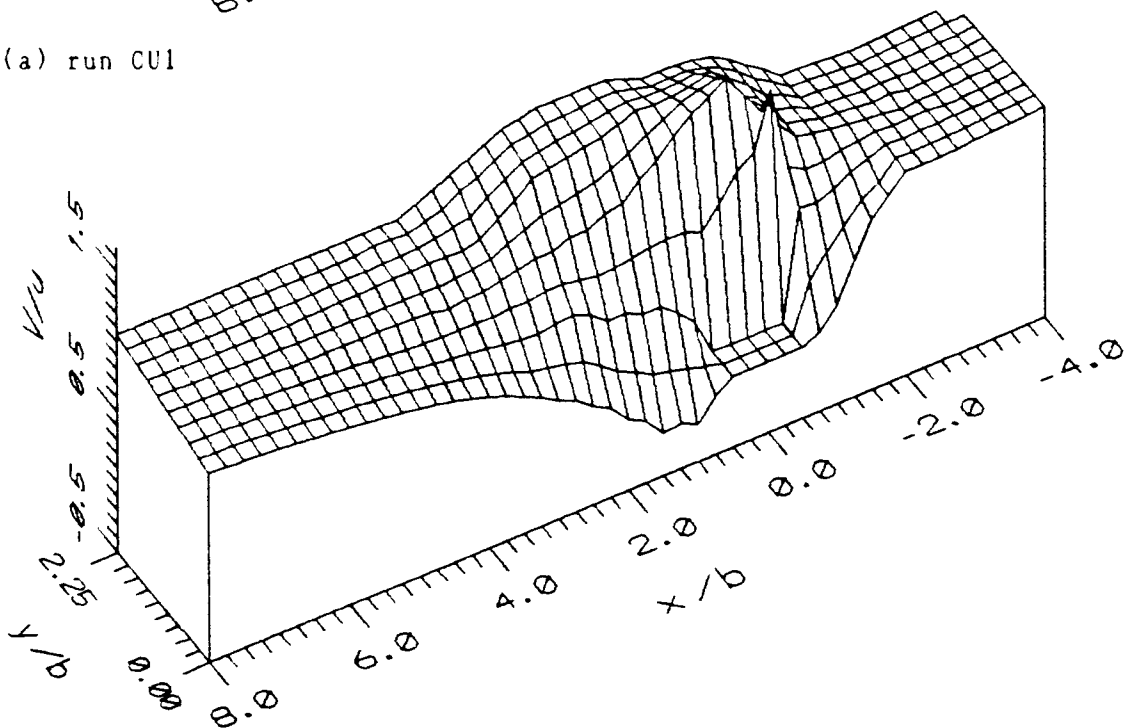
(b) run CU2

Figure 30.   Distribution of horizontal component of velocity around
             cube, circular cylinder and sphere at ⁻z = 0.1 b during
             fixed⁻bed runs CU1⁻to⁻CU5, CY and SP. (Note: flow is
             from right to left)
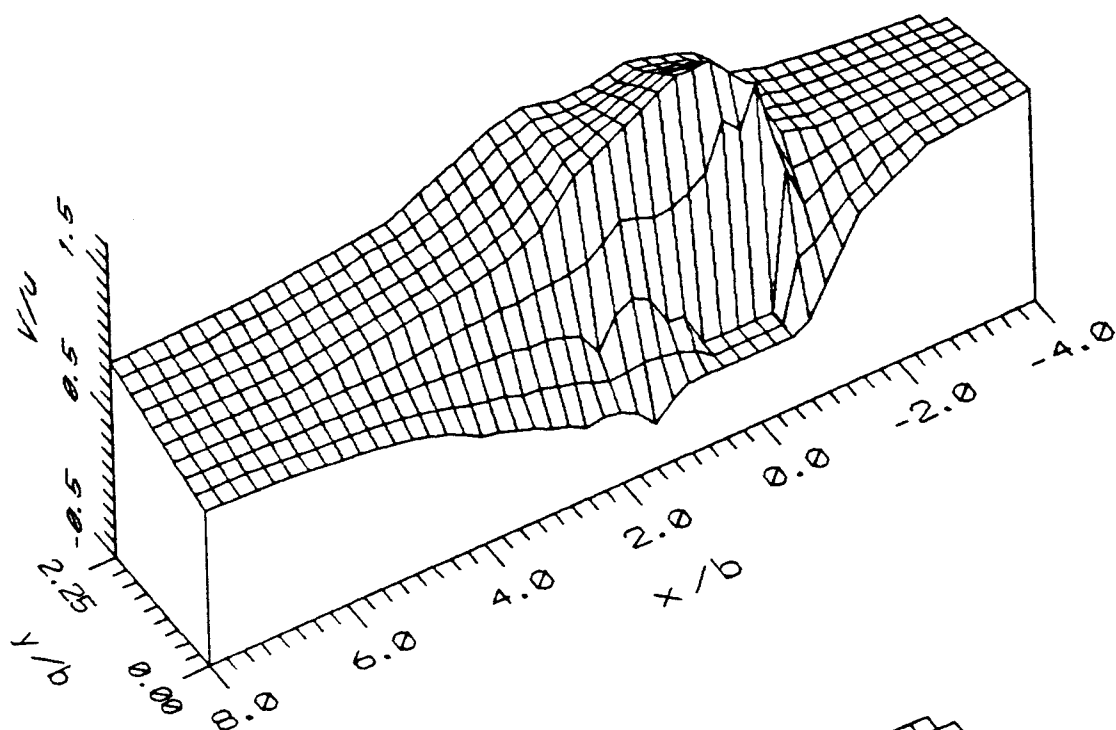
(c) run CU3
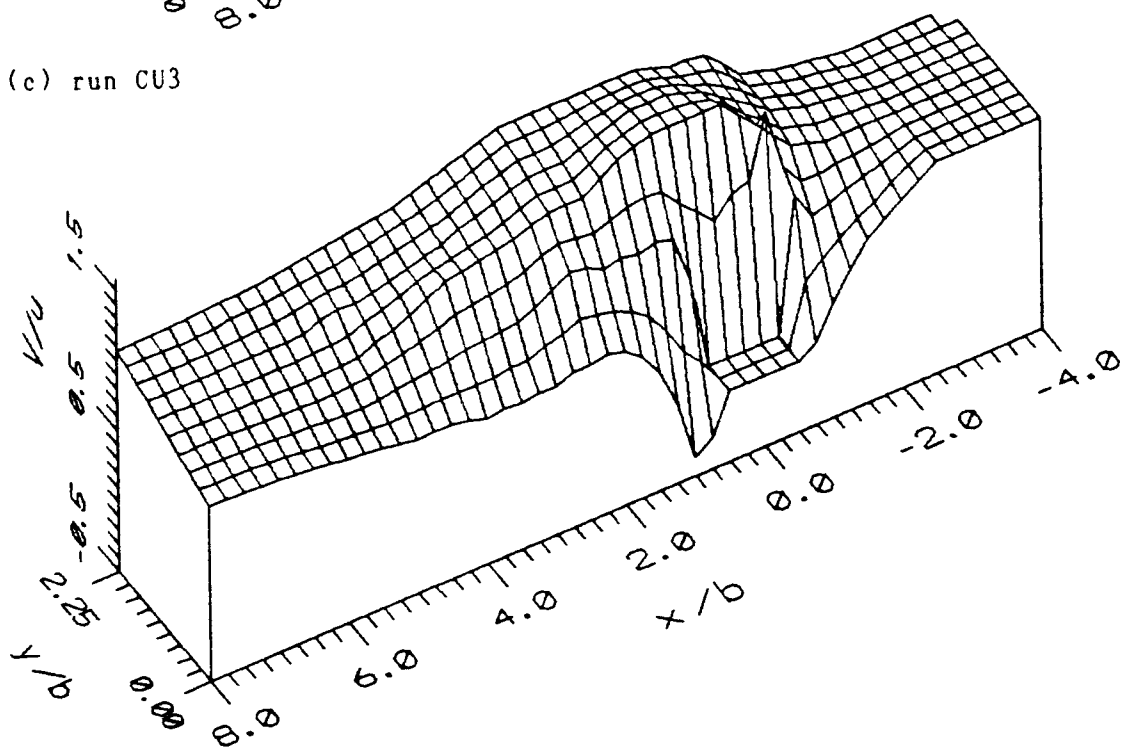
(d) run CU4

Figure 30. Continued.
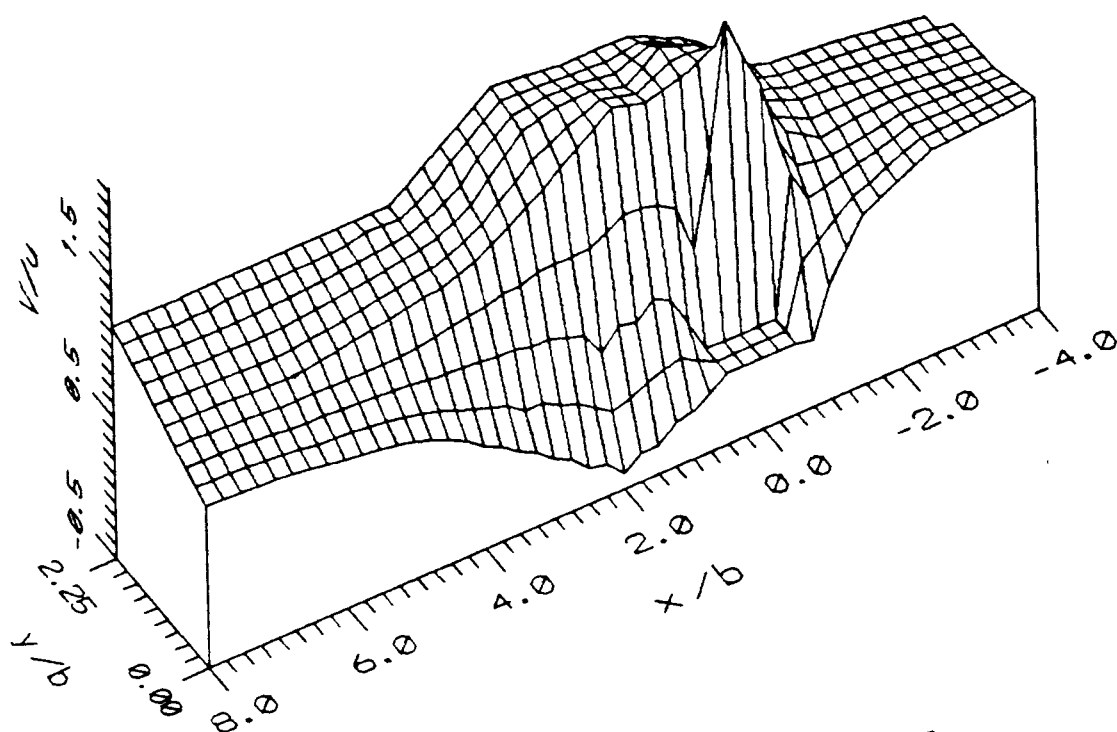
(e) run CU5
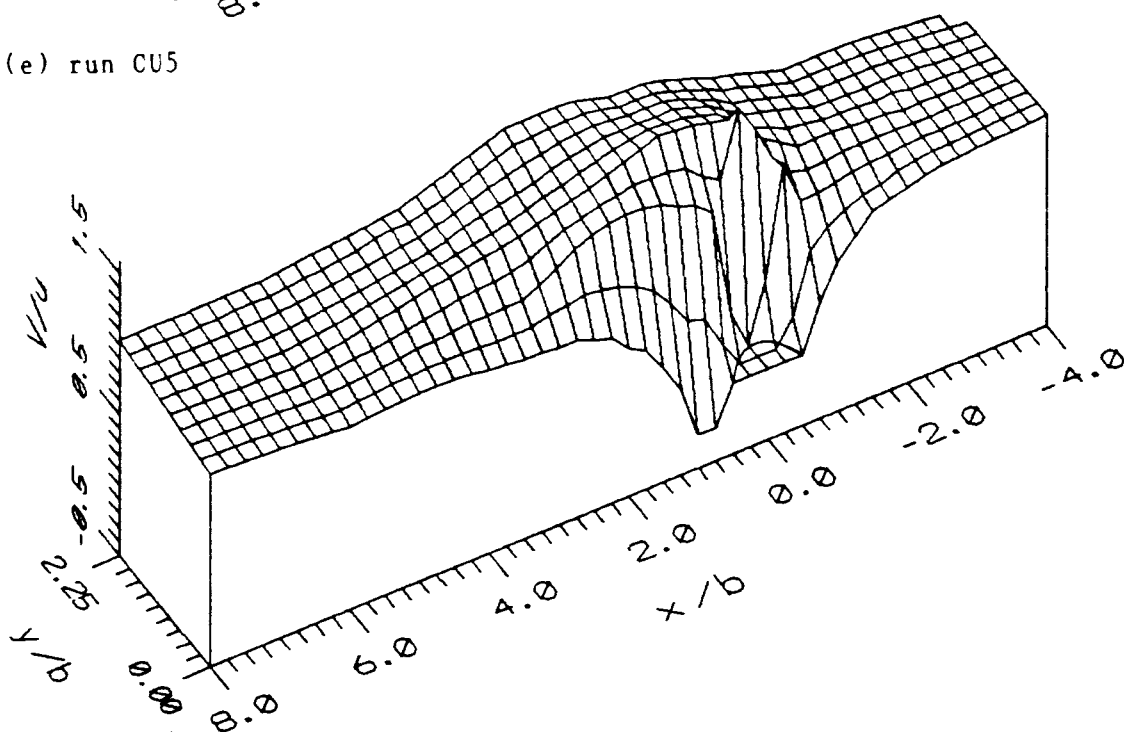
(f) run CY

Figure 30. Continued.
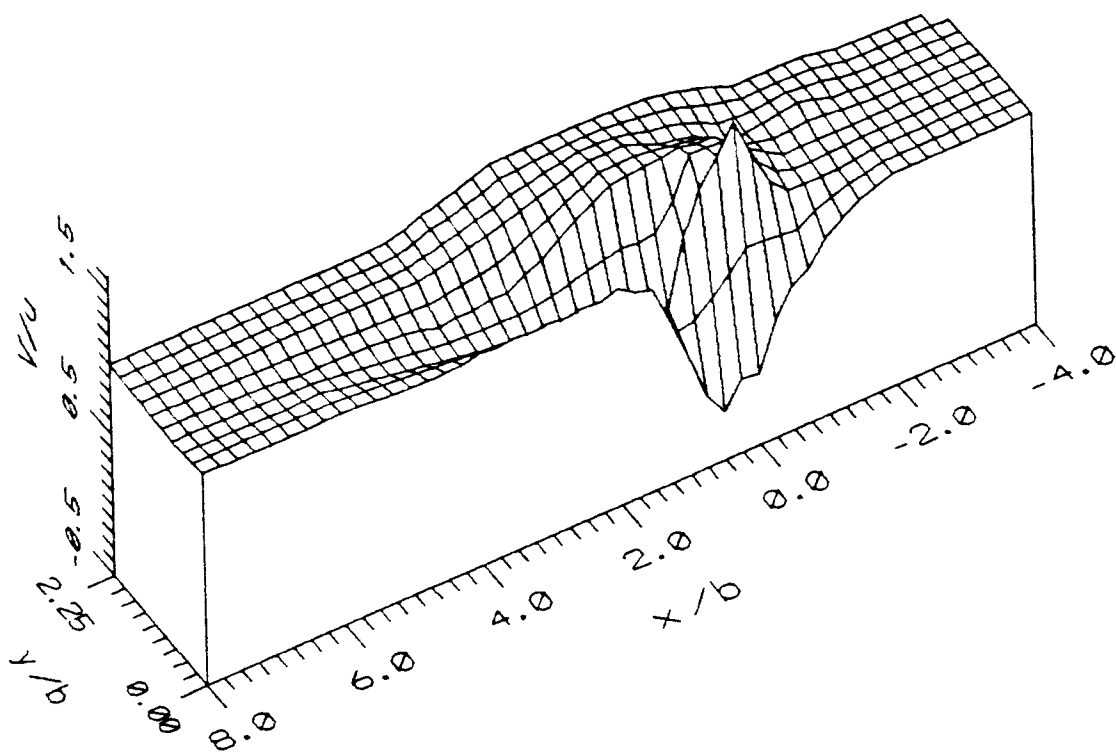
(g) run SP

Figure 30. Continued.

relative horizontal velocity (V/u) for those points that have locally increased velocity near the cube. This is indicated by greater protrusion on the surface in these figures. The averaged V/u values is 1.18 for run CU1 and increases to 1.38 for run CU2 and 1.43 for run CU3. These values are calculated from the arithmetic average of the V/u values that are locally increased within the region of $-1.0 < x/b < 4.0$ and $0 < y/b < 2.17$ in Tables B-5 to B-7 of Appendix B. The maximum values of V/u are 1.28, 1.94 and 1.92, respectively. In Figures 30(d) and 30(e) (runs CU4 and CU5), the flow Froude Number is constant at $F_r = 0.45$ but the relative water depth (D/b) decreases from 1.25 to 0.5. The decrease of the D/b value also leads to increased average V/u values. The averaged V/u value is 1.41 for run CU4 and increases to 1.54 for run CU5. The maximum values of V/u are 1.66 and 2.13, respectively.

At a constant relative water depth, D/b = 1.25, the increase of the flow Froude Number (F_r) from 0.20 to 0.45 causes only a slight increase of the average relative horizontal velocity (V/u) for those points that have locally increased velocity near the cube. In Figure 30(d), a significant increase of the V/u values occurs in the near-wake zone right behind the cube, but it is still not greater than the approach V/u value. The increase is due to the severe change of the water surface in the hydraulic jump zone of run CU4 as compared to that of run CU2. The increase of average V/u value due to the increase of F_r value is more significant when D/b = 0.5 than for D/b = 1.25. This is indicated from comparision of Figure 30(c) and 30(e). As for the comparision of Figures 30(d) and 30(c), the

simultaneous increase of the relative water depth and flow Froude

Number (from $D/b = 0.5$ and $F_r = 0.20$ to $D/b = 1.25$ and $F_r = 0.45$)

does not cause significant increase of the average V/u values. The

values are very close to 1.42. The increase of the V/u values in

the near-wake zone right behind the cube is because of the severe

disturbance of the hydraulic jump.

The influence of obstacle shape upon relative horizontal

velocity (V/u) near the bed are shown in Figure 30(d), 30(f) and

30(g) (runs CU4, CY and SP). In these figures, the relative water

depth (D/b) is 1.25 and the flow Froude Number (F_r) is 0.45. The

average V/u values for those points that have locally increased

velocities near the obstacles are 1.24, 1.28 and 1.41 for sphere,

circular cylinder and cube, respectively. The cube has the highest

average V/u value due to its largest obstruction of the flow. The

maximum V/u values at these obstacles are nearly equal to 1.66.

Local Scour Processes at Movable Isolated Obstacles

The increase of the near-bed flow velocity and drag force as

the flow passes around an isolated obstacle can cause the local

scour of the bed particles and hence the movement of the obstacle on

the river bed. Figure 31 demonstrates the local scour process at a

cube on a sand bed during run C11B. The approach flow Froude Number

is $F_r = 0.20$, the relative obstacle width is $b/D = 0.5$, and the

relative roughness of the bed material is $\bar{d}/D = 0.0026$. The local

scour begins at the upstream corners of the cube, as indicated in
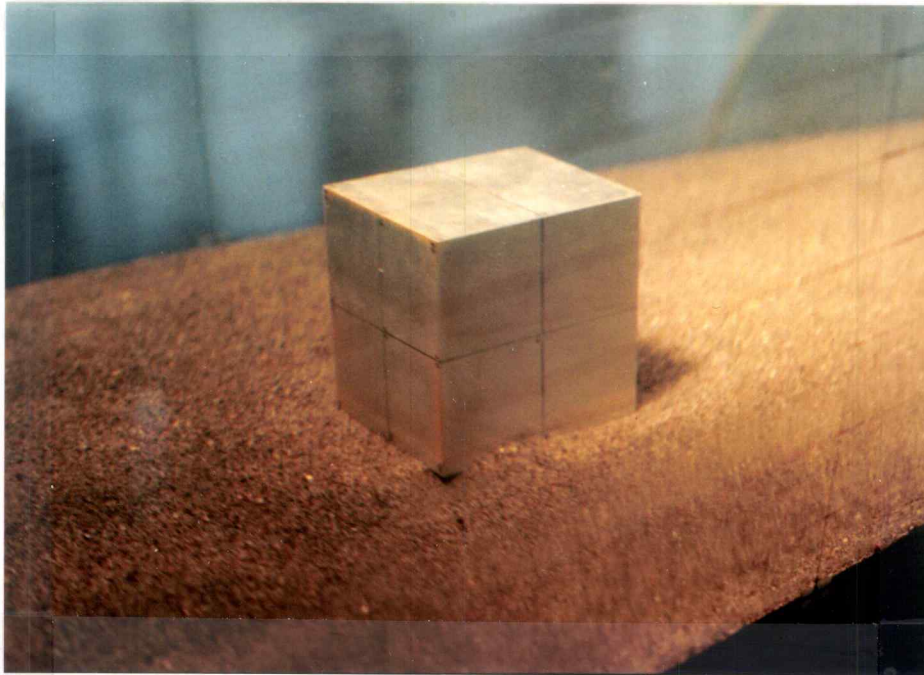
(a) t $\doteq$ 0
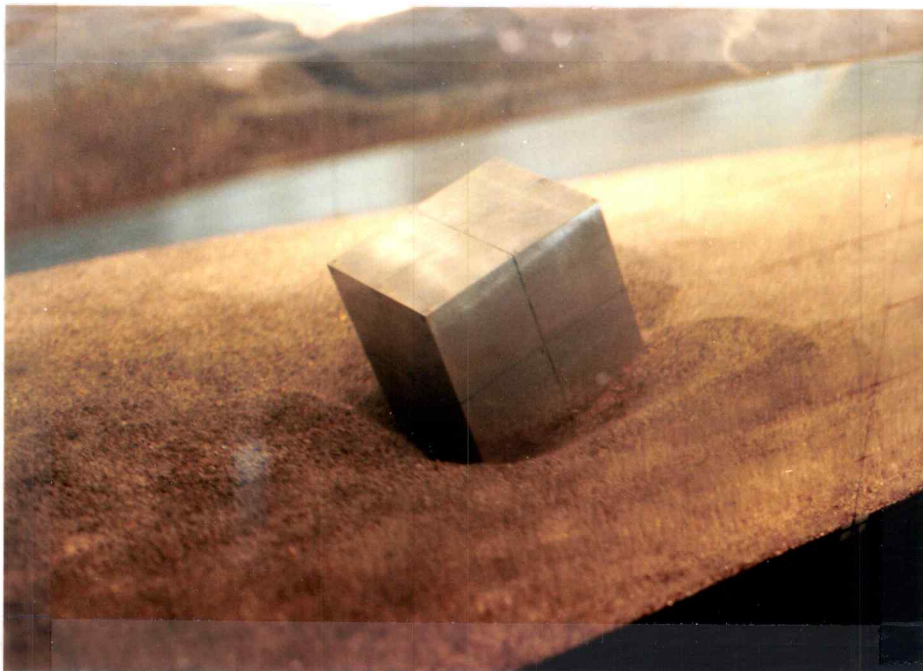
(b) t = 11 minutes

Figure 31. Local scour process at cube on sand bed during run C11B.
(Note: flow is from left to right)
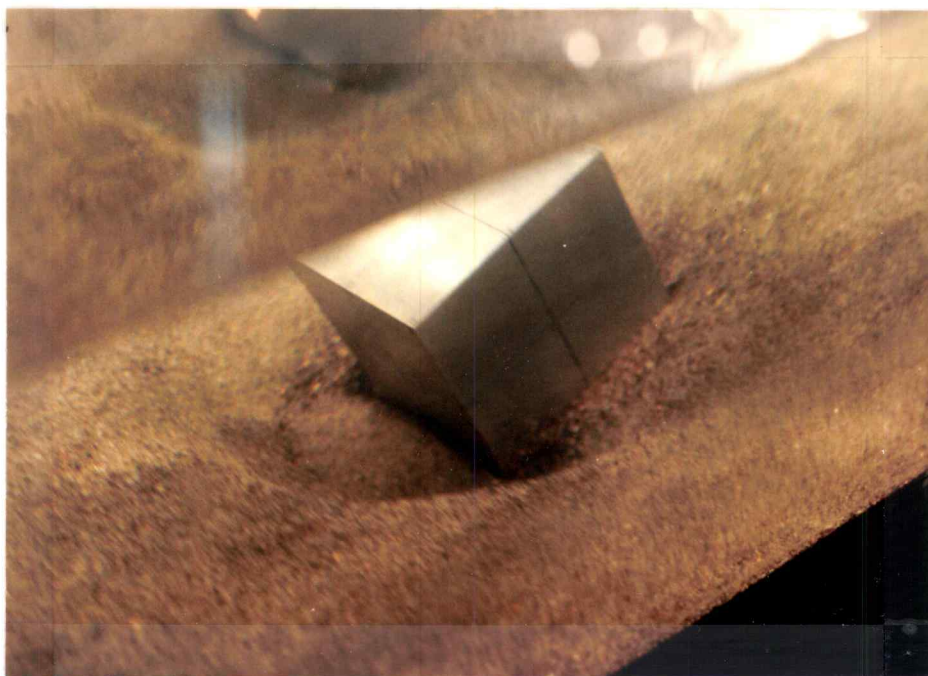
(c) t = 38 minutes
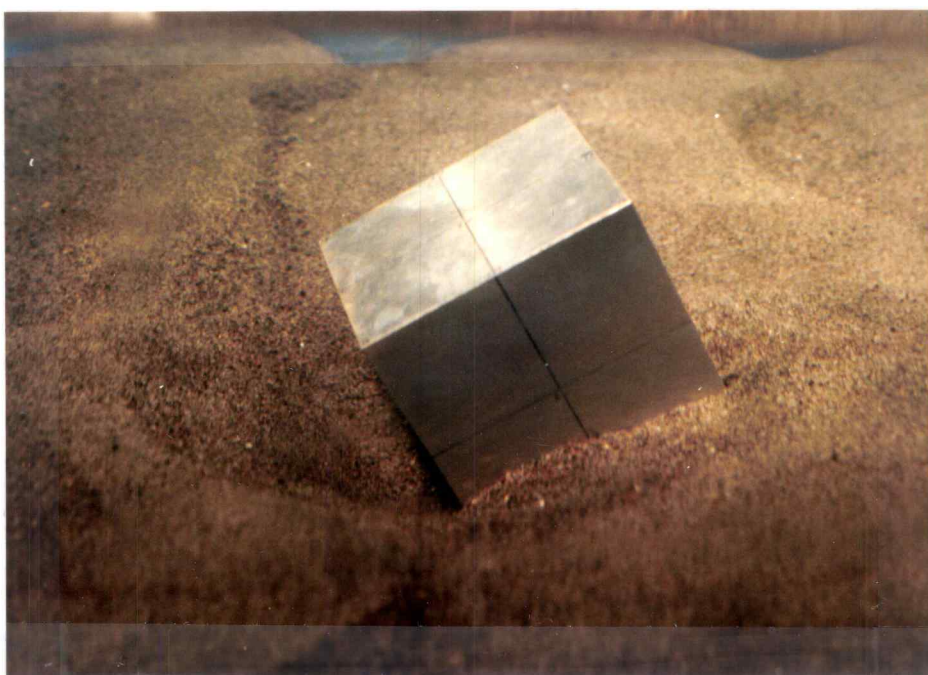
(d) t = 6.24 hours

Figure 31. Continued.
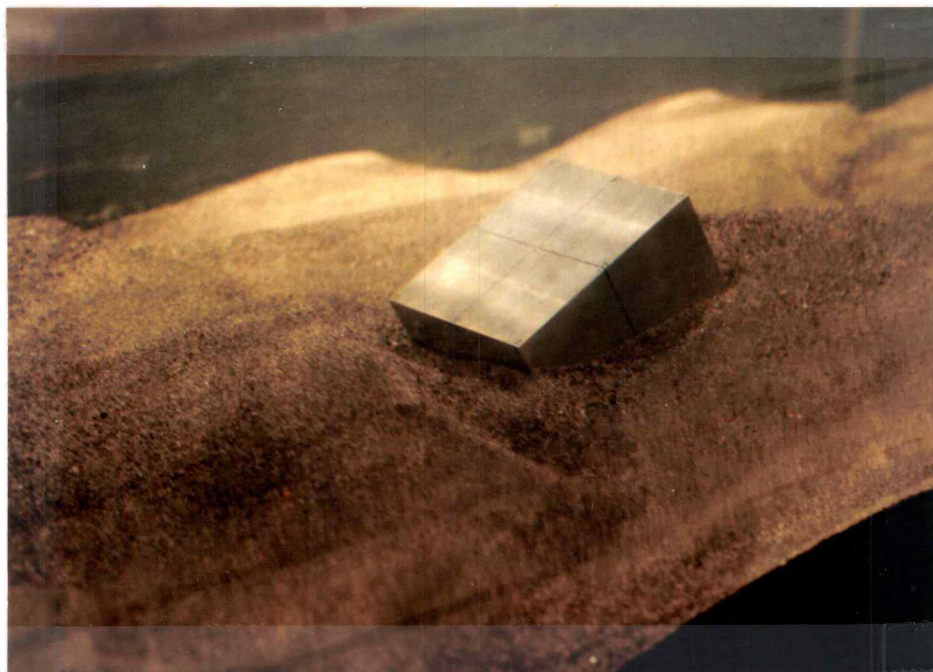
(e) t = 13.74 hours
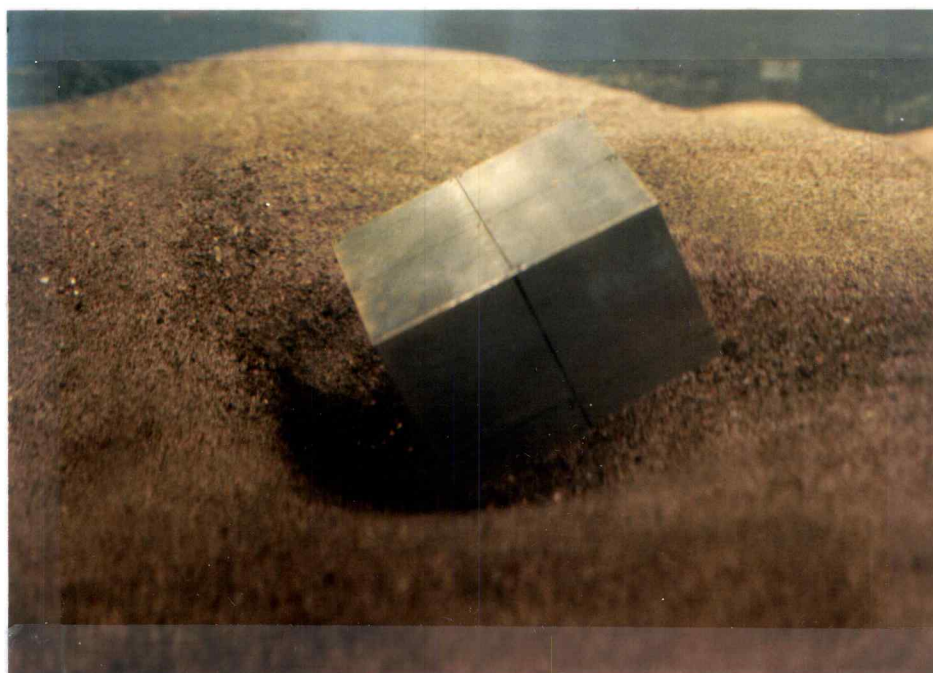
(f) t = 21.53 hours

Figure 31. Continued.

Figure 31(a). The disturbances of the sand bed at the two corners

of the cube begin to grow radially. They rapidly merge at the plane

of symmetry in front of the cube and undercut the bed material

beneath the cube. The overhanging cube then rotates forward and

slides into the upstream scour hole when the equilibrium of the cube

on the sand bed is no longer maintained. Figure 31(b) indicates the

moved cube and the scour pattern at the time t = 11 minutes. The

horseshoe vortex in front of the cube continues to pick up bed

material from the upstream side of the scour hole and carry it

downstream around the cube. The scour hole is gradually deepened

and enlarged. This leads to continuing movement of the cube in the

scour hole, indicated in Figure 31(c) at time t = 38 minutes.

In clear-water scour, without the general movement of the bed

material upstream of the cube, the aforementioned scour process will

continue until the flow is no longer capable of moving the bed

material out of the scour hole at the cube. At this time, the

maximum scour depth is attained and the cube movement stops. In

contrast, when there is general movement of bed material upstream of

the cube after the development of the scour hole, such as during a

rising hydrograph, the scour hole can be filled in by upstream

sediment supply, which can lead to the burial of the cube. When the

sediment supply later decreases on the falling hydrograph, the scour

hole can redevelop and the cube can be reexposed. Figure 31(d),

31(e) and 31(f) reveal this situation at the times t = 6.24 hours,

13.74 hours and 21.53 hours, respectively. In these figures, the

varying sediment supply to the scour hole is because of the

propagation of a bed form, rather than a change of discharge. The
bed form is triggered by the flow disturbance upon the sand bed at
the flume entrance.

Figure 32 indicates the changes of bed pattern behind a cube
during the local scouring process for run C11A at F_r = 0.20,
b/D = 0.67 and $\bar{d}$/D = 0.0034. In the early stage of local scour, the
scoured bed material is soon deposited around the two rear corners
of the cube, as indicated in Figure 32(a) at the time t = 12
minutes. The deposits rapidly merge at the plane of symmetry behind
the cube and continue to grow, as indicated in Figuure 32(b) at the
time t = 26 minutes. As local scour continues, the two mounds of
deposits behind the cube on both sides are pushed away downstream,
and a scour hole begins to form immediately behind the cube. The
two mounds of deposits also generate a train of bed forms that
propagate downstream. These are shown in Figure 32(c) at the time
t = 46 minutes.

In clear-water scour, the scouring will continue until
equilibrium is reached and a scour hole has formed around the cube.
This scour process has occurred in run C11. Figure 33 indicates the
equilibrium scour pattern around the cube for run C11 at F_r = 0.20,
b/D = 0.8 and $\bar{d}$/D = 0.0041. A scour hole is well formed around the
cube and the maximum scour depth has occurred immediately in front
of the cube.

Figure 34 indicates similar behavior for a cube on a gravel
bed. The initiation and merging of scour holes is followed by
general undercutting beneath the cube at times t = 7 minutes and 15

(a) t = 12 minutes
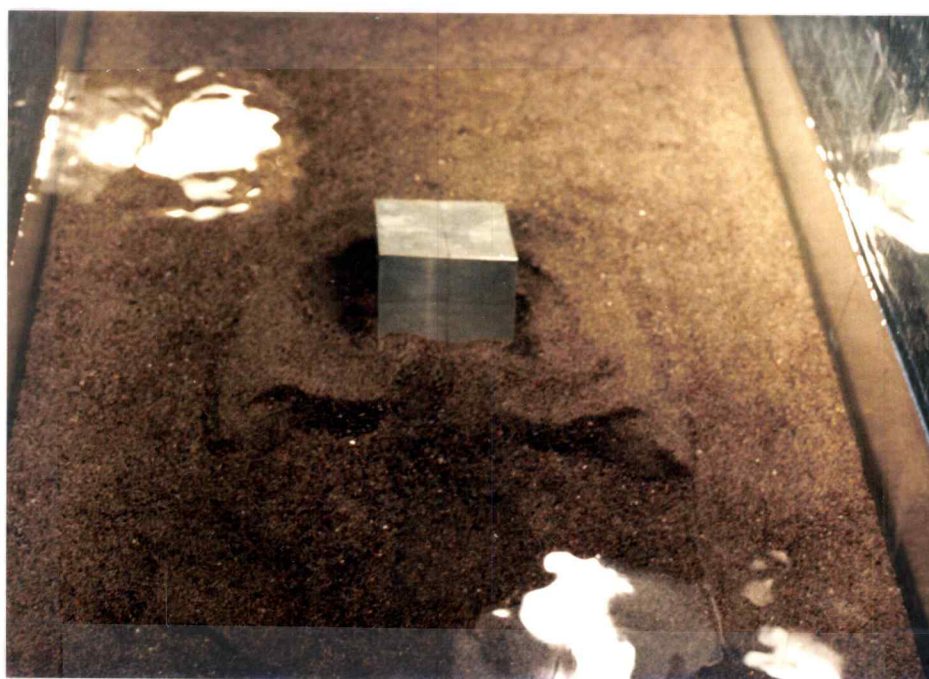
(b) t = 26 minutes

Figure 32. Changes of bed pattern behind cube due to local scour
process during run C11A. (Note: flow is from top to
bottom of photo)
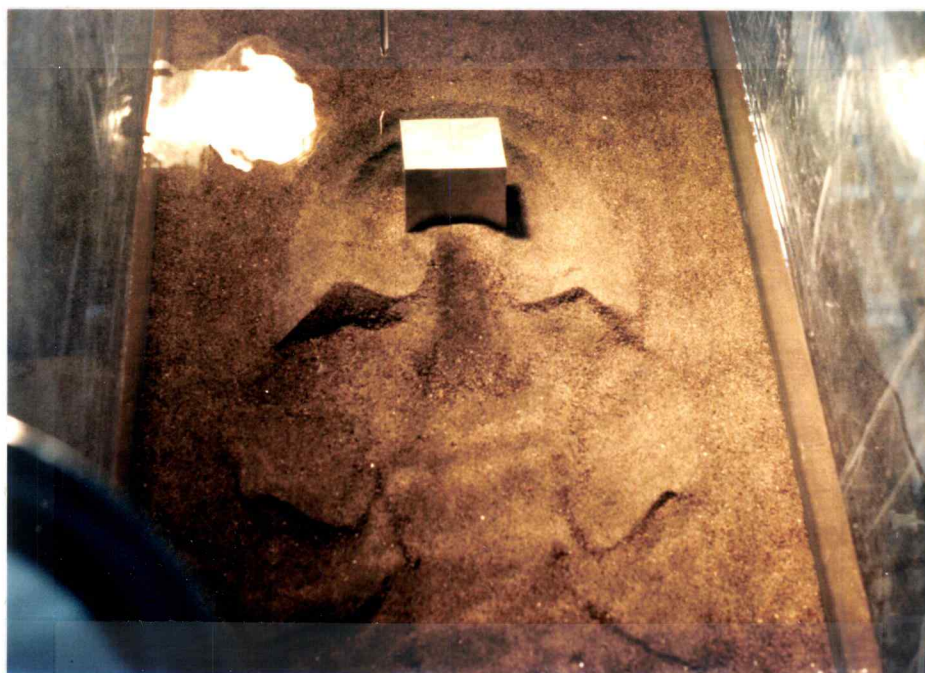
(c) t = 46 minutes

Figure 32.   Continued
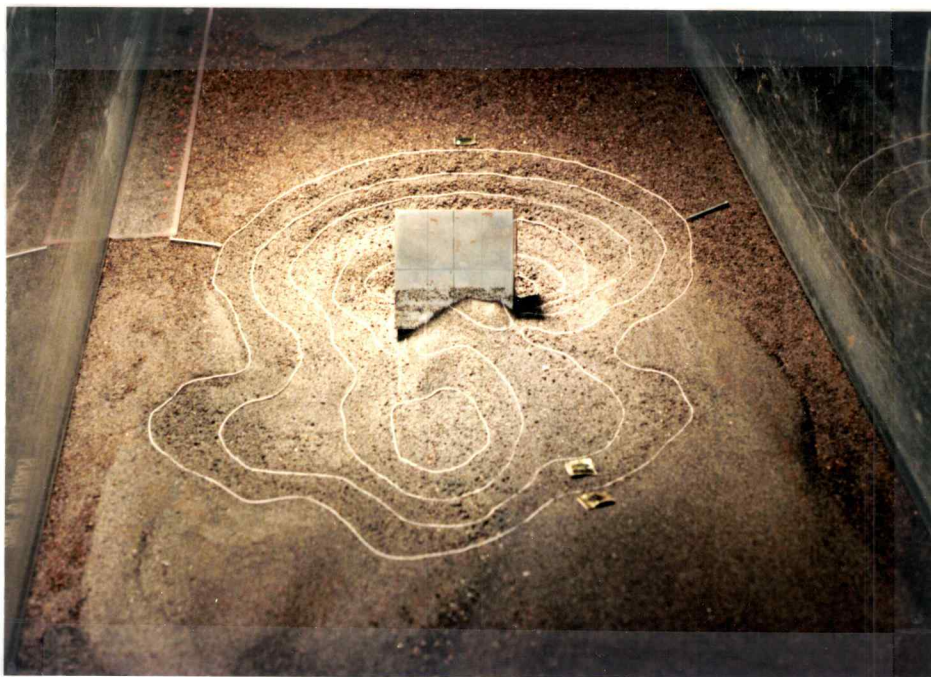
(a) Rear View
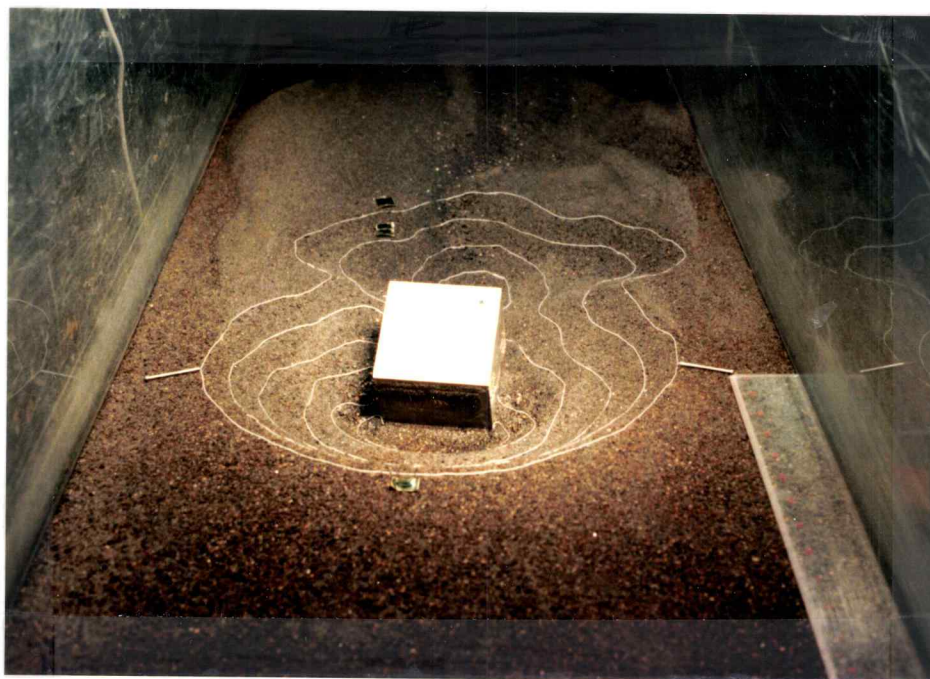
(b) Front View

Figure 33.   Equilibrium scour pattern around cube at end of run C11.
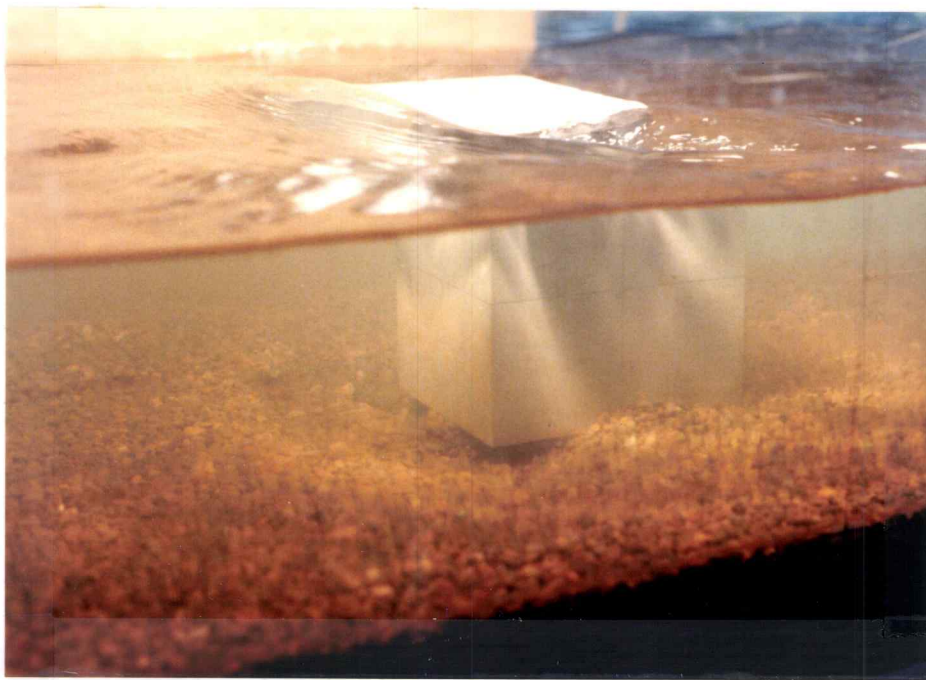
(a) t = 7 minutes
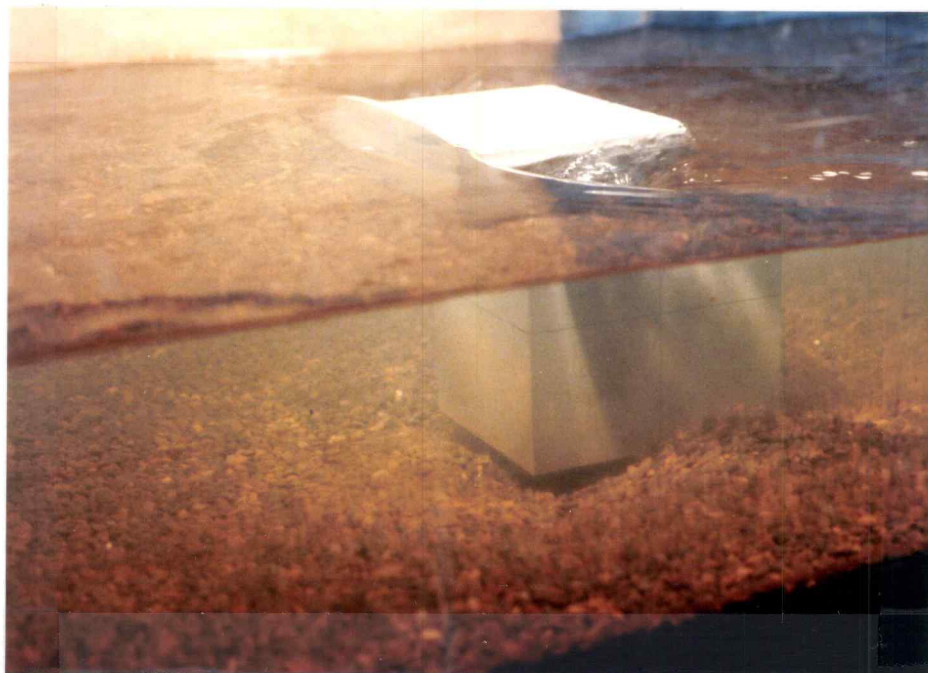
(b) t = 15 minutes

Figure 34.   Initiation and merging of corner scour holes, followed
             by general undercutting of cube on gravel bed during run
             C30. (Note: flow is from left to right)

minutes for run C30. Here, F_r = 0.30, b/D = 1.00 and $\bar{d}$/D = 0.0295.

A local water surface drop and hydraulic jump are evident in Figure 35 just behind the cube. However, no scour hole results there. Furthermore, changing the flow Froude Number and relative submergence as in runs C18, C23A and C28 does not cause any change in scour immediately behind the cube. Figure 35 supports this observation for run C23A at F_r = 0.45, b/D = 0.8 and $\bar{d}$/D = 0.0472. Instead of scour immediately behind the cube, the gravel particles scoured from upstream corners are deposited immediately behind the cube. This occurs progressively and is quite evident at time t = 17 minutes in Figure 35(b).

The experimental observations for clear-water scour show that the local scour process at a cube on a gravel bed is generally similar to that for a cube on a sand bed. Furthermore, experimental observations of local scour at a circular cylinder and a sphere on a movable bed reveal the same local scour process which has been depicted above for a cube.

In the process of local scour, the obstacle movement has been quantified by the displacement of a center point and by the inclination of the unit normal vector and tangent vector on the obstacle top surface. The displacement (S_i, i = x, y and z) is obtained from the changes of the coordinate values of the center point o' on the obstacle top surface, as indicated in Figure 19 (chapter 3). The inclination is indicated by changes of the angles of the direction cosine of the unit normal and tangent vectors on the obstacle top surface ($\Delta\theta_{ij}$, i = x, y, and z, j = z' and x').

(a) t = 4 minutes; little scour or deposition
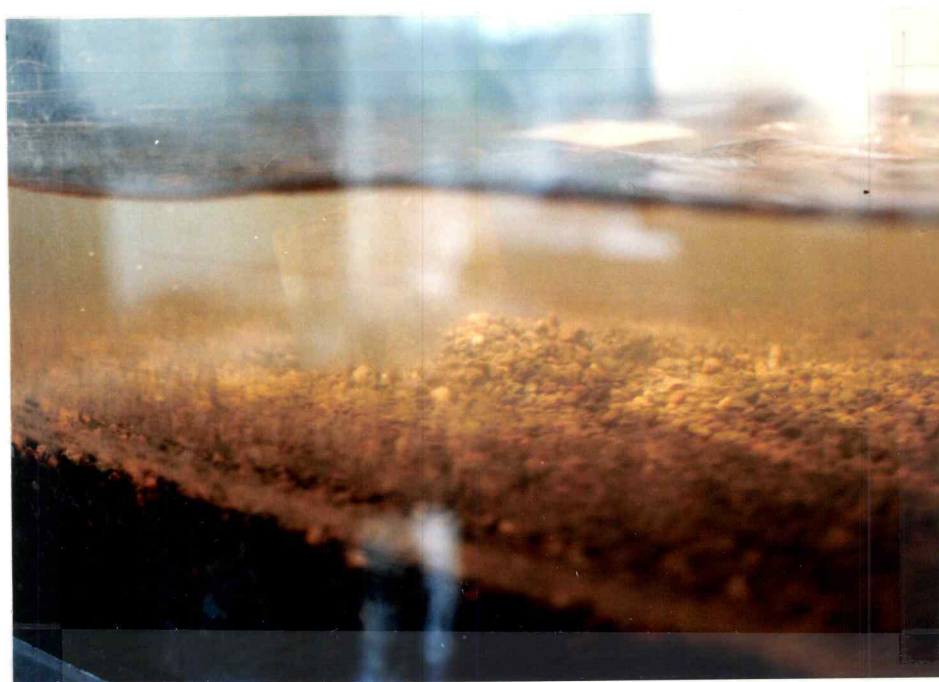
(b) t = 17 minutes; scour upstream and deposition behind cube

Figure 35.   Water surface drop and hydraulic jump behind cube on gravel
             bed during run C23A do not produce scour immediately behind
             cube. (Note: flow is from left to right)

The normal vector $\overrightarrow{o'z'}$ on the obstacle top surface in Figure 19

(chapter 3) is calculated from the "cross product" of the two

vectors (Kaplan, 1981), which are calculated from the measured

coordinate values of the preselected points on the obstacle top

surface in Figure 24 (chapter 4). These two vectors are $\overrightarrow{31}$ and $\overrightarrow{32}$

for the cube, $\overrightarrow{01}$ and $\overrightarrow{02}$ for the circular cylinder, and $\overrightarrow{02}$ and $\overrightarrow{03}$ for

the sphere in Figure 24. The tangent vector $\overrightarrow{o'x'}$ on the top surface

of the cube is obtained directly from the negative value of the

vector $\overrightarrow{32}$. The tangent vector $\overrightarrow{o'x'}$ on the top surface of the

circular cylinder and the sphere is obtained directly from the

negative value of the vector $\overrightarrow{02}$.

Figure 36 indicates the time history of the local scour depth

at a section that passes along the side of the cube ($y/b = 0.54$) for

run C13. The flow Froude Number is $F_r = 0.10$, the relative obstacle

width is $b/D = 0.5$ and the relative roughness is $\bar{d}/D = 0.0019$. The

results of the relative scour depth (d_s/D) and the longitudinal

position (x/b) are listed in Table 4. The induced cube movement is

shown in Figure 37 and the results are listed in Table 5.

Figure 36 clearly indicates the growth of the scour hole and

the propagation of the deposited mount before the time $t = 9.20$

hours. The trough of the scour hole is located just around the

corner of the cube but the peak of the deposited mound is propagated

downstream. In the same period, the cube is barely moved, as

indicated in Figure 37. However, by the time $t = 22.72$ hours, the

cube has rotated and slided into the scour hole significantly; also,

the trough of the scour hole has shifted upstream. After the time
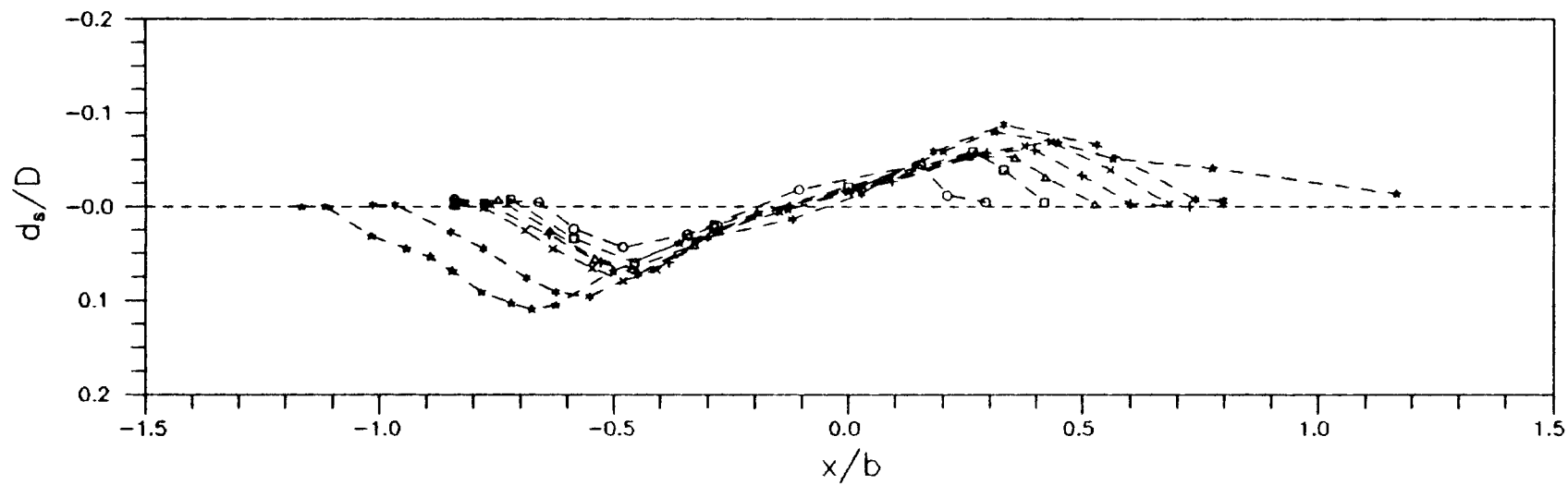
Key: --o--, t = 0.38 hour; --□--, t = 1.38 hour; --△--, t = 2.34 hour;
       --+--, t = 4.44 hour; --x--, t = 9.12 hour; --*--, t = 22.62 hour;
       --★--, t = 47.79 hour.

Figure 36.   Time history of the local scour depth at y/b = 0.54 along
             the side of the cube during run C13.   (Note: flow is from
             left to right)

Table 4. Time history of the local scour depth at y/b = 0.54 along the side of the cube during run C13.

t (hr)	x/b	ds/D	t (hr)	x/b	ds/D	t (hr)	x/b	ds/D	t (hr)	x/b	ds/D
0.33	-0.840	-0.007	1.32	-0.840	-0.004	2.26	-0.840	-0.001	47.60	-1.167	0.000
0.34	-0.660	-0.004	1.34	-0.720	-0.007	2.27	-0.747	-0.007	47.62	-1.116	0.000
0.36	-0.585	0.024	1.35	-0.585	0.034	2.29	-0.636	0.025	47.63	-1.017	0.031
0.37	-0.480	0.044	1.36	-0.456	0.060	2.31	-0.540	0.056	47.65	-0.942	0.045
0.38	-0.342	0.030	1.38	-0.285	0.019	2.33	-0.459	0.066	47.66	-0.891	0.054
0.40	-0.105	-0.018	1.40	0.000	-0.021	2.33	-0.328	0.041	47.67	-0.846	0.069
0.41	0.153	-0.045	1.41	0.264	-0.059	2.34	-0.195	0.006	47.69	-0.783	0.091
0.43	0.210	-0.012	1.42	0.330	-0.039	2.35	0.000	-0.018	47.70	-0.720	0.103
0.44	0.291	-0.004	1.44	0.417	-0.004	2.36	0.255	-0.054	47.71	-0.675	0.109
						2.38	0.354	-0.053	47.73	-0.624	0.105
						2.39	0.420	-0.031	47.74	-0.501	0.069
						2.41	0.525	-0.003	47.76	-0.360	0.039
									47.77	-0.129	0.003
4.36	-0.840	-0.001	9.03	-0.840	-0.001	22.52	-1.014	-0.001	47.78	0.030	-0.022
4.37	-0.771	-0.003	9.04	-0.780	0.001	22.54	-0.966	-0.001	47.80	0.201	-0.059
4.38	-0.639	0.030	9.05	-0.690	0.025	22.55	-0.849	0.027	47.81	0.309	-0.079
4.39	-0.528	0.060	9.06	-0.630	0.045	22.56	-0.780	0.045	47.84	0.447	-0.068
4.40	-0.450	0.072	9.07	-0.546	0.066	22.57	-0.687	0.076	47.86	0.564	-0.051
4.42	-0.381	0.060	9.08	-0.480	0.079	22.58	-0.624	0.091	47.88	0.774	-0.041
4.44	-0.270	0.022	9.10	-0.408	0.068	22.60	-0.552	0.096	47.91	1.167	-0.013
4.45	-0.126	-0.001	9.11	-0.291	0.025	22.61	-0.447	0.072	47.93	1.530	-0.012
4.46	0.093	-0.027	9.12	-0.147	0.006	22.63	-0.300	0.033	47.97	2.310	-0.004
4.47	0.294	-0.057	9.14	0.000	-0.015	22.64	-0.120	0.013			
4.48	0.396	-0.060	9.15	0.261	-0.056	22.65	0.027	-0.013			
4.49	0.498	-0.033	9.16	0.375	-0.065	22.66	0.180	-0.059			
4.51	0.600	-0.003	9.18	0.432	-0.069	22.68	0.330	-0.087			
4.52	0.726	0.000	9.19	0.558	-0.039	22.69	0.528	-0.066			
			9.20	0.684	-0.003	22.71	0.738	-0.007			
						22.72	0.798	-0.006			

S_i (cm)

t (hour)

Key: $--o--$, S_x; $--\square--$, S_y; $--\triangle--$, S_z.

(a) displacement

$\Delta\Theta_{ij}$ (degree)

t (hour)

Key: $--o--$, $\Delta\theta_{xx'}$; $--\square--$, $\Delta\theta_{yz'}$; $--\triangle--$, $\Delta\theta_{zz'}$; $--\diamond--$, $\Delta\theta_{xx'}$;
$--+--$, $\Delta\theta_{yx'}$; $--x--$, $\Delta\theta_{zx'}$.
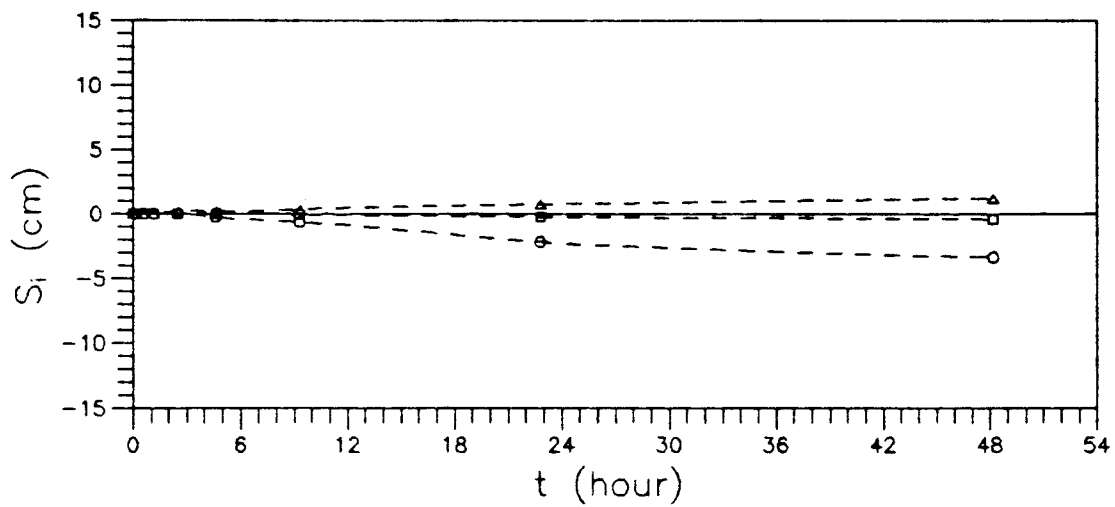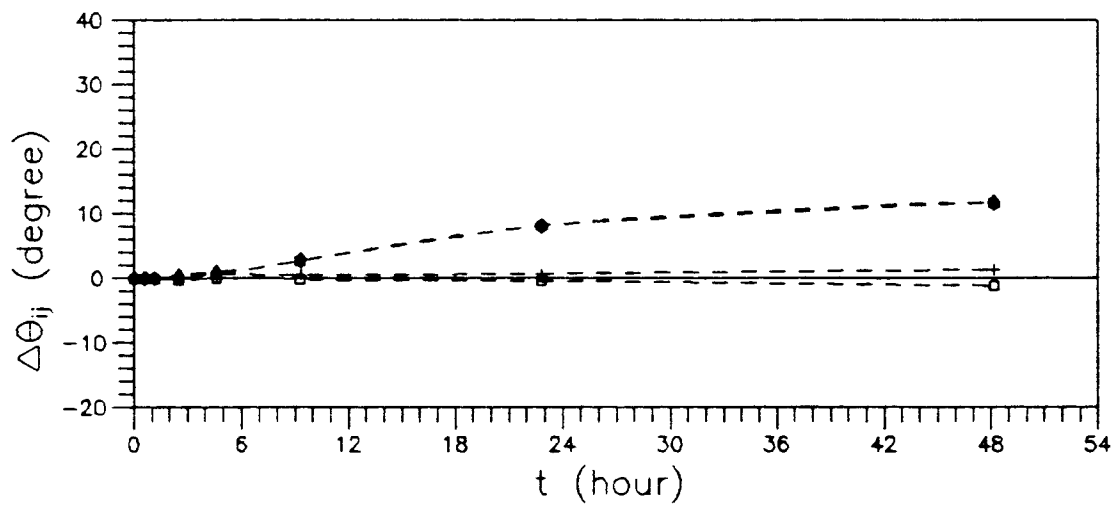
(b) inclination

Figure 37. Time history of cube movement during run C13.

Table 5. Time history of cube movement during run C13.

t (hr)	S_x (cm)	S_y (cm)	S_z (cm)	$\Delta\theta_{xz}$ (deg)	$\Delta\theta_{yz}$ (deg)	$\Delta\theta_{xz}$ (deg)	$\Delta\theta_{xy}$ (deg)	$\Delta\theta_{yx}$ (deg)	$\Delta\theta_{zx}$ (deg)
0.00	0.00	0.00	0.00	0.00	0.00	0.00	0.00	0.00	0.00
0.60	0.00	0.00	0.00	0.00	0.00	0.00	0.00	0.00	0.00
1.16	0.00	0.00	0.00	0.00	0.00	0.00	0.00	0.00	0.00
2.51	0.00	0.00	0.18	0.17	-0.26	0.31	0.55	0.52	0.17
4.61	-0.27	0.00	0.18	0.69	-0.00	0.69	0.98	0.69	0.69
9.29	-0.64	-0.06	0.34	2.77	-0.15	2.77	2.82	0.52	2.77
22.81	-2.19	-0.24	0.73	8.15	-0.45	8.16	8.18	0.69	8.15
48.15	-3.35	-0.43	1.19	11.61	-1.20	11.67	11.71	1.34	11.64

t = 22.72 hours, the shifting of the scour hole and the movement of the obstacle continue but increase very slowly until equilibrium is reached.

The major movement of the cube is the displacement S_x and S_z and the inclination $\Delta\theta_{xz'}$, $\Delta\theta_{zz'}$, $\Delta\theta_{xx'}$ and $\Delta\theta_{zx'}$ shown in Figure 37. The values of $\Delta\theta_{xz'}$, $\Delta\theta_{zz'}$, $\Delta\theta_{xx'}$ and $\Delta\theta_{zx'}$ are nearly identical. Figure 38 shows the time history of cube displacement and cube inclination of run C11 at $F_r = 0.20$, $b/D = 0.8$ and $\bar{d}/D = 0.0041$. The test duration is six days and the results are shown in Table 6. As indicated in Figure 38, the cube movement increases rapidly during the active period of local scour and then gradually reaches equilibrium. A practical equilibrium movement of the cube seems to be reached at about 24 hours.

Figure 39 allows comparision of the time histories for the major relative displacements (S_x/D and S_z/D) and the major inclination ($\Delta\theta_{xz'}$) for runs C30 and C33 at $b/D = 1.0$ and $\bar{d}/D = 0.0295$. The flow Froude Numbers of runs C30 and C33 are 0.30 and 0.45, respectively. The results are shown in Table 7. The time scale is nondimensionlized as $\bar{U}t/D$. As indicated in these figures, the increase of the flow Froude Number increases the cube movement and causes the obstacle to reach an equilibrium earlier. Fisher (1984) conducted flume experiments on local scour at natural boulders. He considered the 24-hour test duration for sand beds and 12-hour test duration for gravel beds to be adequate for near-equilibrium scour to develop in the flume. In the present research, the duration of each test is in general more than one day and the
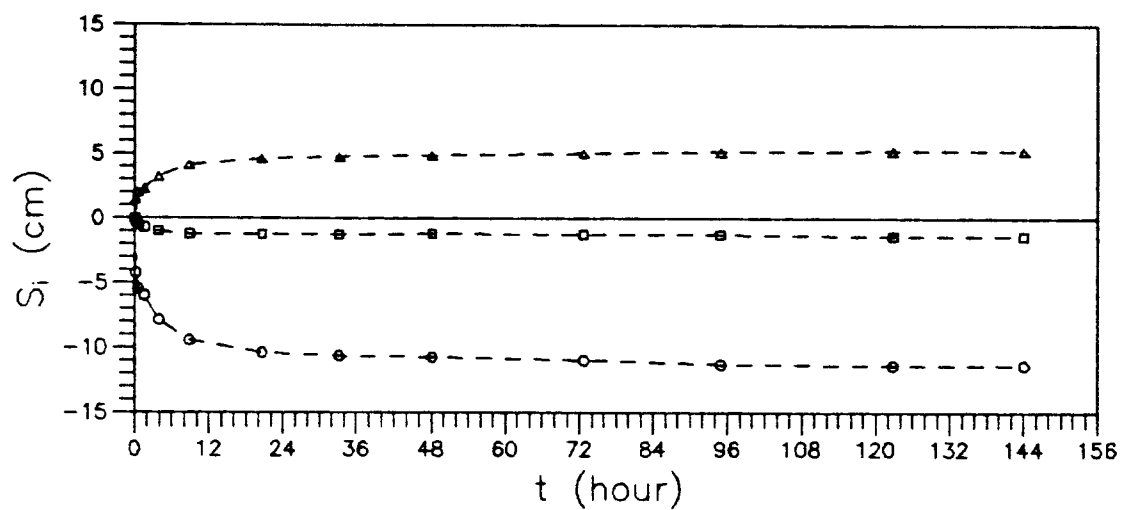
Key: --o--, S_x; --□--, S_y; --△--, S_z.

(a) displacement
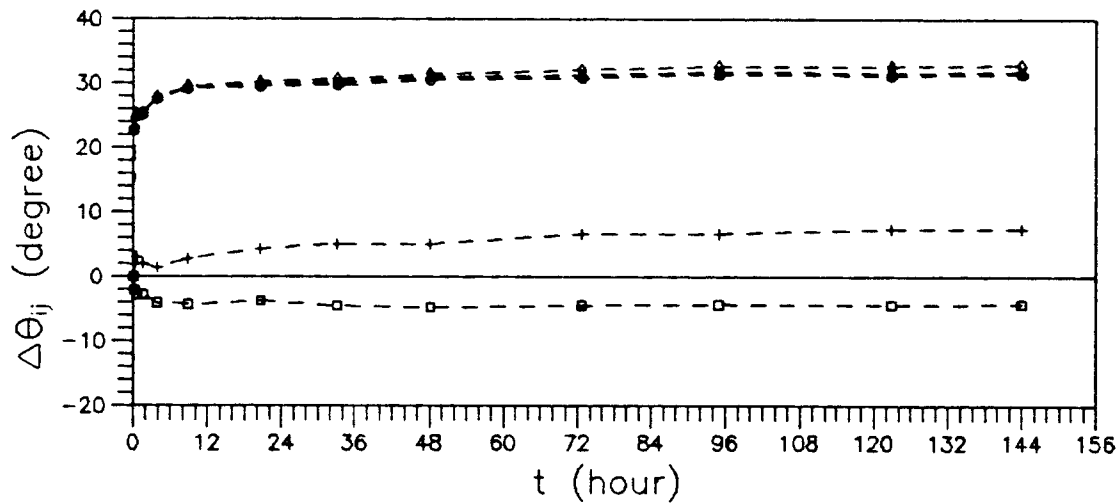
Key: --o--, $\Delta\theta_{xz'}$; --□--, $\Delta\theta_{yz'}$; --△--, $\Delta\theta_{zz'}$; --◇--, $\Delta\theta_{xx'}$;
      --+--, $\Delta\theta_{yx'}$; --x--, $\Delta\theta_{zx'}$.

(b) inclination

Figure 38.   Time history of cube movement during run C11.

Table 6. Time history of cube movement during run C11.

t (hr)	S_x (cm)	S_y (cm)	S_z (cm)	$\Delta\theta_{xx}$ (deg)	$\Delta\theta_{yx}$ (deg)	$\Delta\theta_{zx}$ (deg)	$\Delta\theta_{xx}$ (deg)	$\Delta\theta_{yx}$ (deg)	$\Delta\theta_{xx}$ (deg)
0.00	0.00	0.00	0.00	0.00	0.00	0.00	0.00	0.00	0.00
0.17	-4.27	-0.34	1.46	22.81	-2.10	22.91	22.96	1.88	22.88
0.53	-5.49	-0.58	1.98	24.84	-2.82	25.02	25.18	3.00	24.98
1.51	-6.00	-0.73	2.26	25.19	-2.77	25.37	25.40	2.08	25.31
3.89	-7.89	-1.04	3.20	27.64	-4.03	27.98	27.84	1.39	27.80
8.84	-9.48	-1.25	4.11	29.16	-4.29	29.54	29.58	2.77	29.42
20.57	-10.42	-1.28	4.60	29.59	-3.77	29.87	30.23	4.34	29.85
33.17	-10.67	-1.28	4.75	29.79	-4.50	30.20	30.67	5.07	30.16
48.14	-10.76	-1.22	4.88	30.58	-4.77	31.03	31.49	5.08	30.99
72.73	-11.00	-1.28	5.03	30.90	-4.43	31.28	32.14	6.65	31.28
94.93	-11.31	-1.28	5.15	31.48	-4.29	31.83	32.70	6.71	31.83
122.77	-11.40	-1.40	5.21	31.29	-4.38	31.66	32.71	7.37	31.66
143.99	-11.40	-1.40	5.24	31.51	-4.24	31.86	32.89	7.35	31.86
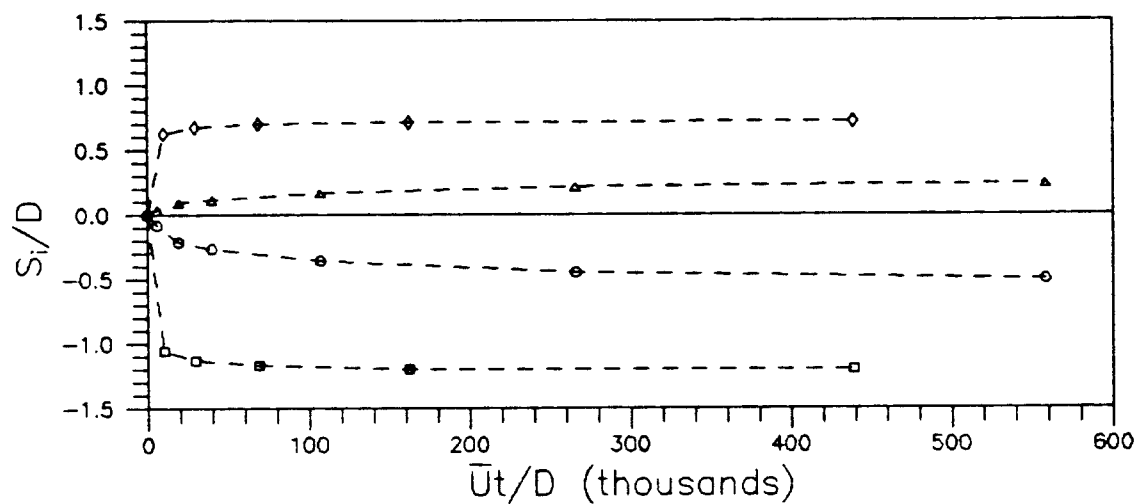
Key: --o--, S_x/D (C30); --□--, S_x/D (C33); --▲--, S_z/D (C30); --◇--, S_z/D (C33).

(a) displacement
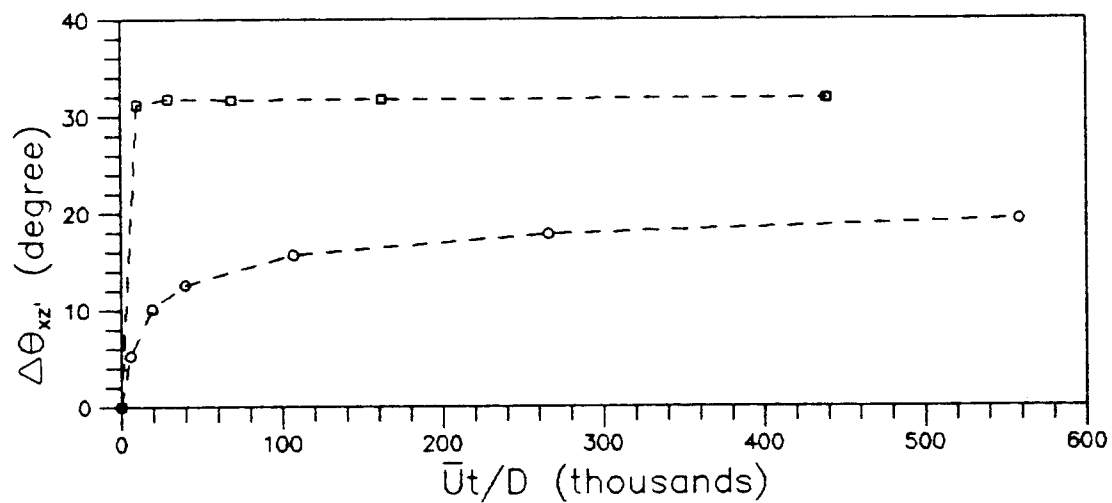
Key: --o--, C30; --□--, C33.

(b) inclination

Figure 39. Comparison of the time histories for the major movement of the cube during runs C30 and C31.

Table 7. Time history of cube movement during runs C30 and C33.

Run No.	t (hr)	$\bar{U}t/D$	S_x/D	S_y/D	S_z/D	$\Delta\theta_{xz}$ (deg)	$\Delta\theta_{yz}$ (deg)	$\Delta\theta_{zz}$ (deg)	$\Delta\theta_{xx}$ (deg)	$\Delta\theta_{yx}$ (deg)	$\Delta\theta_{zx}$ (deg)
	0.00	0.00B+00	0.000	0.000	0.000	0.00	0.00	0.00	0.00	0.00	0.00
	0.57	6.04B+03	-0.084	0.000	0.039	5.26	1.76	5.55	5.31	0.84	5.24
	1.81	1.92B+04	-0.213	-0.006	0.090	10.14	0.56	10.16	10.17	0.85	10.14
C30	3.75	3.98B+04	-0.267	-0.015	0.114	12.62	-0.11	12.62	12.63	0.34	12.62
	10.05	1.07B+05	-0.360	-0.030	0.165	15.72	-0.37	15.73	15.81	1.54	15.73
	25.06	2.66B+05	-0.450	-0.045	0.213	17.84	-0.98	17.87	18.12	2.90	17.87
	52.59	5.58B+05	-0.504	-0.060	0.237	19.38	-1.64	19.46	19.65	2.75	19.45
	0.00	0.00B+00	0.000	0.000	0.000	0.00	0.00	0.00	0.00	0.00	0.00
	0.64	1.01B+04	-1.059	0.060	0.624	31.24	3.37	31.46	31.24	1.73	31.18
	1.86	2.96B+04	-1.134	0.060	0.675	31.81	2.84	31.97	31.81	1.37	31.78
C33	4.34	6.90B+04	-1.170	0.060	0.699	31.71	3.98	32.02	31.72	1.73	31.66
	10.19	1.62B+05	-1.203	0.057	0.711	31.77	3.54	32.01	31.77	1.72	31.72
	27.59	4.39B+05	-1.203	0.057	0.717	31.85	3.15	32.04	31.87	0.87	31.85

time history of the obstacle displacement is monitored to obtain the

adequate practical equilibrium of local scour.

Local Scour at Isolated Obstacles

Bed Scour Depth and Scour Volume

The equilibrium scour patterns in clear-water scour at an

isolated obstacle on a movable bed can be different under different

flow conditions. Flow Froude Number, relative obstacle size, and

relative bed roughness cause some of these differences.

Figure 40 shows the equilibrium scour patterns at a two-inch

cube on a sand bed for runs C5, C6 and C8 at the flow Froude Number

$F_r = 0.20$. The zone of local scour at the cube enlarges and

eventually surrounds the cube when the relative water depth D/b

increases from 0.5 to 2.0. Figure 41 shows the equilibrium scour

patterns at one-inch, two-inch, and four-inch cubes on a sand bed at

$F_r = 0.20$ for runs C2, C7 and C17, respectively, in a water depth of

three inches. The scour patterns look similiar around the cubes

when the relative obstacle size b/D increases from 0.33 to 1.33.

However, when the cube size becomes relatively large the scour at

the two front corners of the cube can no longer merge to form a

single deep trough across the front of the cube. This is indicated

in Figure 41(c) as compared to Figures 41(b) and 41(a).

In Figure 40, runs C8, C6 and C5 represent the successive

increase of the relative obstacle size (b/D = 0.5, 1.0 and 2.0) and
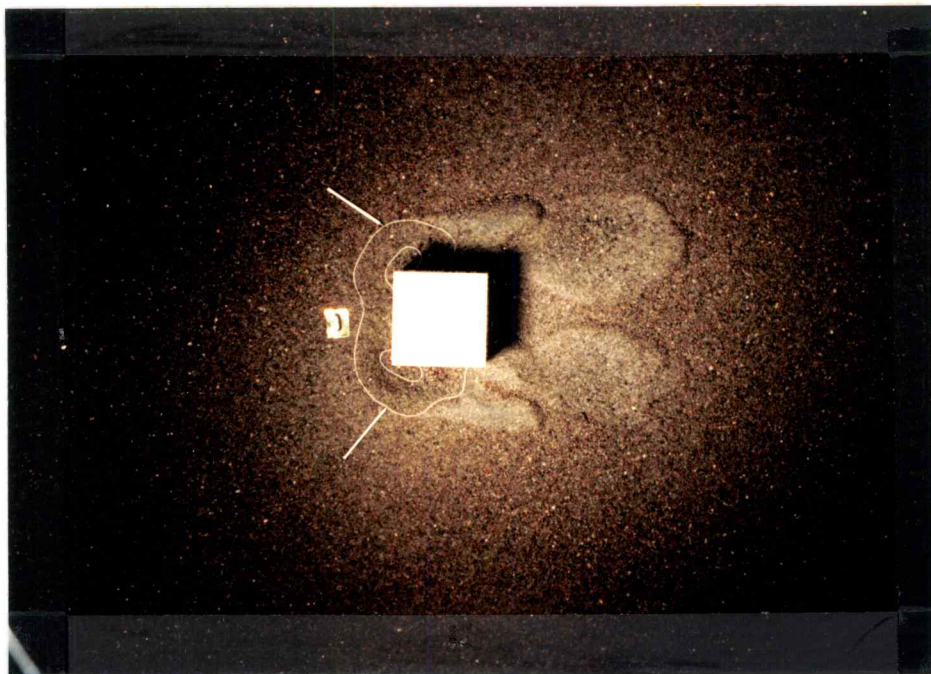
(a) run C5; D/b = 0.5 (scour depth contour interval = 0.61 cm)
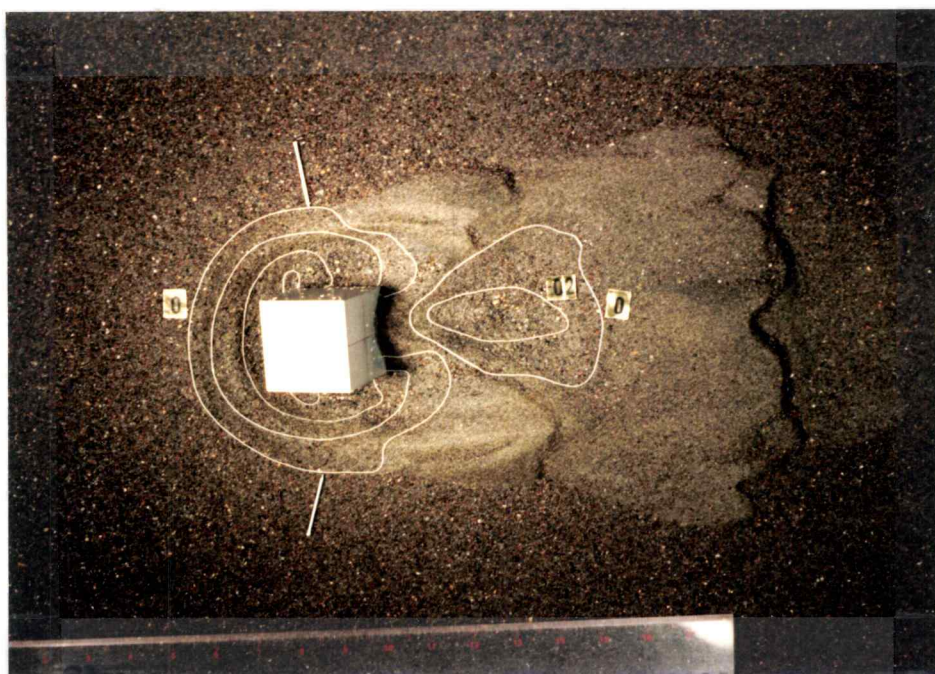
(b) run C6; D/b = 1.0 (scour depth contour interval = 0.61 cm)

Figure 40.   Equilibrium scour patterns at cube on sand bed, as
              affected by relative water depth, for runs C5, C6
              and C8. (Note: flow is from left to right)
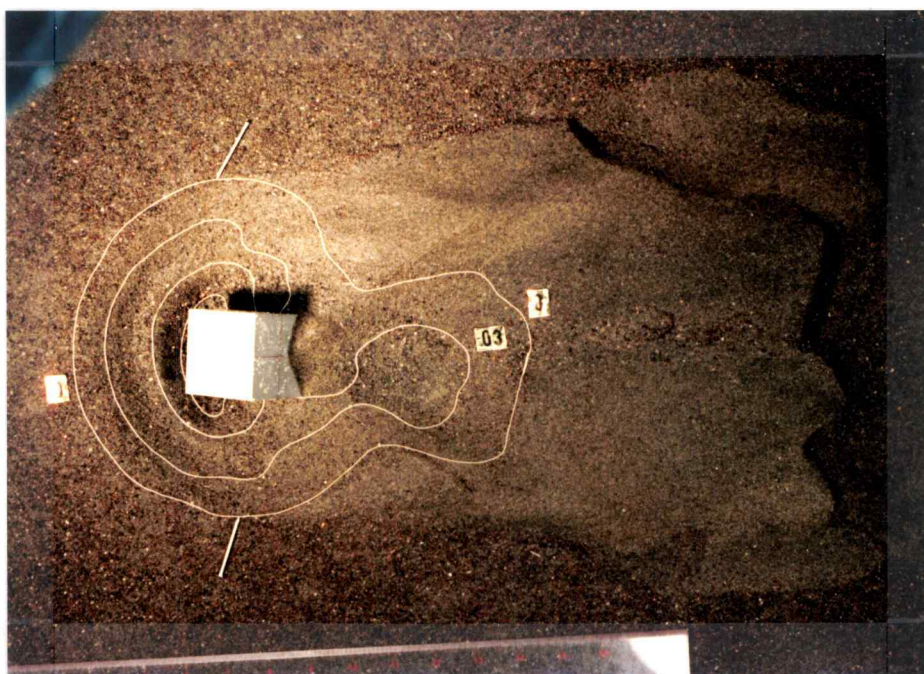
(c) run C8; D/b = 2.0 (scour depth contour interval = 0.91 cm)

Figure 40.   Continued.
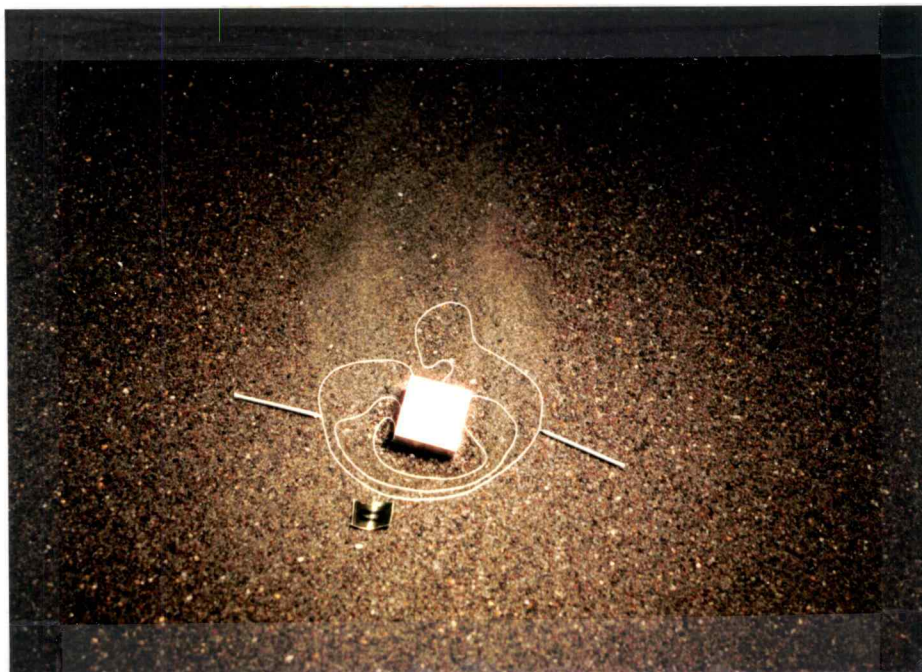
(a) run C2; 1-inch cube (scour depth contour interval = 0.46 cm)
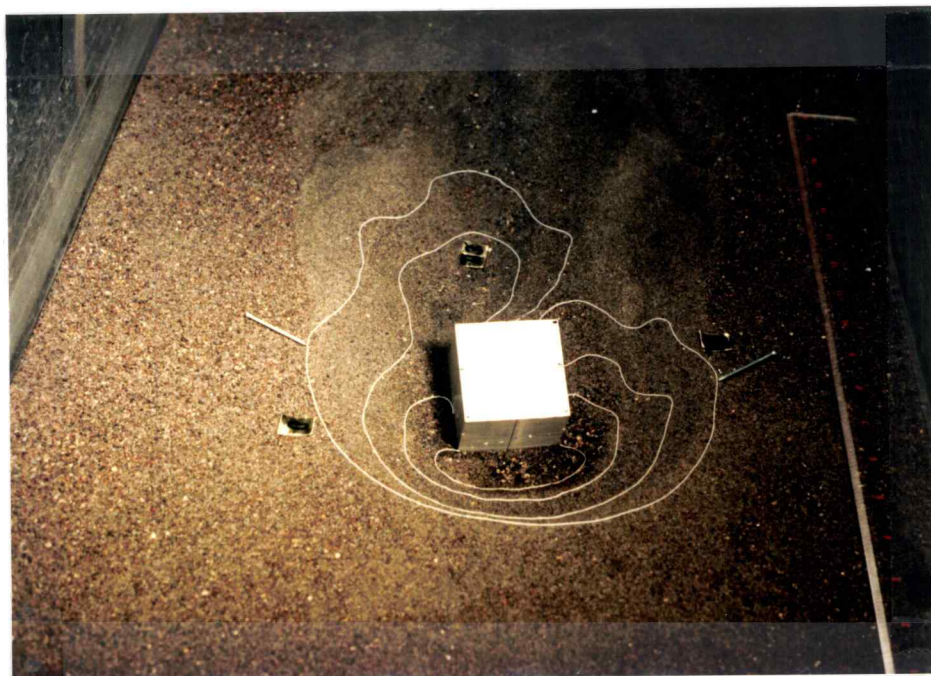
(b) run C7; 2-inch cube (scour depth contour interval = 0.91 cm)

Figure 41. Equilibrium scour patterns at cubes on sand bed, as
           affected by relative size of cube, for runs C2, C7
           and C17. (Note: view is from upstream)

(c) run C17; 4-inch cube (scour depth contour interval = 0.91 cm)

Figure 41.   Continued.

the relative roughness of the bed material ($\bar{d}/D$ = 0.0038, 0.0077 and 0.0154). Runs C2, C7 and C17 in Figure 41 maintain the same relative roughness of the bed material ($\bar{d}/D$ = 0.0051) but successively increase the relative obstacle size (b/D = 0.33, 0.67 and 1.33). The comparison of Figure 40 and Figure 41 in this order indicates that the equilibrium scour pattern at a cube and the scour zone relative to the cube size could change and reduce significantly if the roughness of the bed material become relative large.

Figure 42 shows the equilibrium scour patterns at a four-inch cube on a gravel bed for runs C29, C32 and C34 in two inches water depth. The relative obstacle size and the relative roughness of the bed material are the same (b/D = 2.0 and $\bar{d}/D$ = 0.0591) but the flow Froude Number F_r increases from 0.30 to 0.65. The equilibrium scour pattern at the two front corners of the cube is not merged yet at the lower flow Froude Number F_r = 0.30, as indicated in Figure 42(a). The scour patterns at the two front corners of the cube can merge and develop a larger scour hole to surround the cube when the flow Froude Number increases. These are indicated in Figure 42(b) (F_r = 0.45) and 42(c) (F_r = 0.65). At the same relative obstacle size, the higher flow Froude Number could develop a different and relatively smaller scour pattern if the roughness of the bed material becomes relatively larger. Comparison of Figures 42(a) and 40(a) demonstrates this situation.

In general, there is not a unique equilibrium scour pattern for clear-water scour at a cube on a movable bed. Many scour patterns have been depicted in the previous section. The

(a) run C29, F_r = 0.30 (scour depth contour interval = 0.76 cm)

(b) run C32, F_r = 0.45 (scour depth contour interval = 0.76 cm)

Figure 42. Equilibrium scour patterns at cube on gravel bed, as affected by Froude Number, for runs C29, C32 and C34. (Note: view is from upstream)
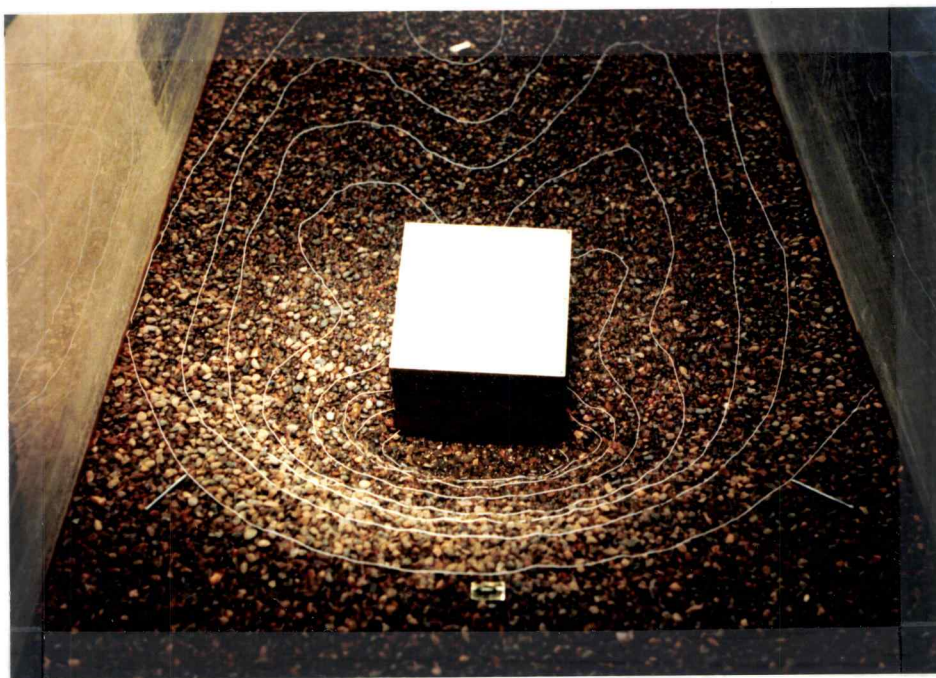
(c) run C34, F_r = 0.65 (scour depth contour interval = 0.91 cm)

Figure 42. Continued.

interaction of the relative obstacle size b/D, the flow Froude

Number F_t and the relative roughness of the bed material $\bar{d}/D$ upon

local scour can lead to several different equilibrium scour patterns

at the obstacle on a movable-bed. The maximum equilibrium scour

depth and scour volume are thus highly depend upon these parameters.

The experimental results giving maximum equilibrium scour depth

d_{se} and the scour volume V_{se} at isolated obstacles on a sand/gravel

bed are nondimensionalized and listed in Table 8. Figure 43 shows

plots of maximum relative equilibrium scour depth d_{se}/D at cubes

vs. relative obstacle size b/D, flow Froude Number F_t and relative

roughness of bed material $\bar{d}/D$, respectively. The plots clearly

indicate that the results of d_{se}/D at the cube are too scattered to

be adequately described as a function of b/D, F_t or $\bar{d}/D$ alone in

clear-water scour. Therefore, consideration is needed of the

interaction of b/D, F_t and $\bar{d}/D$ upon d_{se}/D.

In reviewing research on clear-water scour at isolated bridge

piers, several pertient results were noted. Breusers et al. (1977)

and Baker (1980) concluded that the maximum equilibrium scour depth

at a bridge pier increased with the approach water depth when the

water depth was relatively shallow as compared to the pier width.

But when the water depth was relatively deep, equilibrium scour

depth did not depend on the water depth but increased linearly with

the pier width. The effect of the sediment size could be neglected

when the sediment size was relative small as compared to the pier

width. The maximum equilibrium scour depth increased with the flow

velocity in clear-water scour and then fluctuated along a constant

Table 8. Dimensionless maximum equilibrium scour depth and scour volume at obstacle in movable-bed experiments.

Obstacle Shape	Bed Material	Run No.	t (hr)	F_r	b/D	$\bar{d}/D$	d_{s*}/D	V_{s*}/D^3
		C1	43.46	0.20	0.67	1.02E-02	0.160	0.156
		C2	24.46	0.20	0.33	5.12E-03	0.192	0.054
		C3	24.15	0.10	0.50	3.84E-03	0.033	0.002
		C4	48.31	0.10	0.25	1.92E-03	0.078	0.005
		C5	49.68	0.20	2.00	1.54E-02	0.360	0.915
		C6	48.79	0.20	1.00	7.68E-03	0.444	1.175
		C7	32.98	0.20	0.67	5.12E-03	0.440	0.791
		C8	39.93	0.20	0.50	3.84E-03	0.339	0.337
	Sand	C9	48.80	0.20	2.00	1.02E-02	0.720	4.159
		C10	44.01	0.20	1.00	5.10E-03	0.672	--
		C11	144.00	0.20	0.80	4.09E-03	0.578	2.135
		C12	47.76	0.10	1.00	3.84E-03	0.087	0.024
		C13	48.52	0.10	0.50	1.92E-03	0.119	0.021
		C14	88.64	0.10	0.33	1.28E-03	0.162	0.028
		C15	45.76	0.20	4.00	1.54E-02	0.492	3.051
		C16	49.58	0.20	2.00	7.68E-03	1.036	7.475
		C17	39.77	0.20	1.33	5.12E-03	0.792	6.057
Cube		C18	1.07	0.45	0.80	9.45E-02	0.095	0.001
		C19	1.03	0.30	1.00	5.91E-02	0.120	0.003
		C20	24.45	0.30	0.50	2.95E-02	0.123	0.010
		C21	51.25	0.30	0.33	1.97E-02	0.156	0.021
		C22	45.92	0.45	2.00	1.18E-01	0.348	0.915
		C23A	50.73	0.45	0.80	4.72E-02	0.437	0.586
		C23B	51.00	0.45	0.80	4.72E-02	0.428	0.586
		C24	48.12	0.45	0.50	2.95E-02	0.309	0.358
	Gravel	C25	47.82	0.80	2.00	1.18E-01	1.250	7.506
		C26	48.97	0.65	1.00	5.91E-02	0.672	1.747
		C27	26.70	0.55	0.67	3.94E-02	0.451	1.277
		C28	73.64	0.45	0.80	3.15E-02	0.528	2.032
		C29	9.24	0.30	2.00	5.91E-02	0.258	0.191
		C30	52.98	0.30	1.00	2.95E-02	0.384	0.415
		C31	50.00	0.30	0.67	1.97E-02	0.360	0.212
		C32	49.47	0.45	2.00	5.91E-02	1.072	10.015
		C33	28.39	0.45	1.00	2.95E-02	0.708	4.195
		C34	31.20	0.65	2.00	5.91E-02	1.502	42.312
		Y1	26.93	0.20	2.00	1.54E-02	0.204	0.244
	Sand	Y2	49.27	0.20	1.00	7.68E-03	0.377	0.610
Cylinder		Y3	48.58	0.20	0.50	3.84E-03	0.360	0.331
	Gravel	Y4	48.21	0.45	0.80	4.72E-02	0.408	0.562
	Sand	S1	48.18	0.20	1.00	7.68E-03	0.228	0.244
Sphere		S2	49.66	0.20	0.50	3.84E-03	0.315	0.210
	Gravel	S3	48.46	0.45	0.80	4.72E-02	0.235	0.176
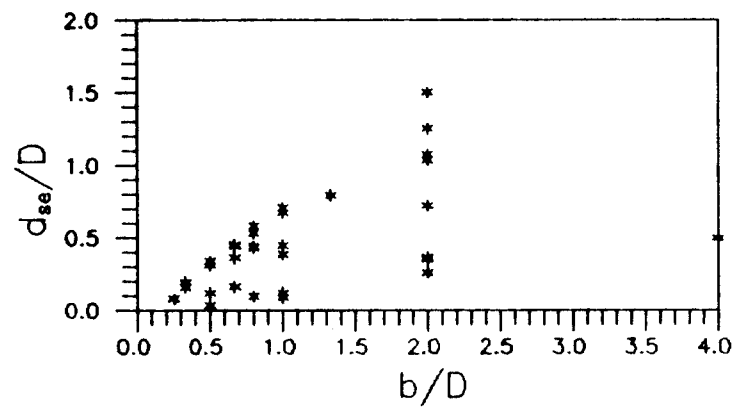
(a) d_{se}/D vs. b/D
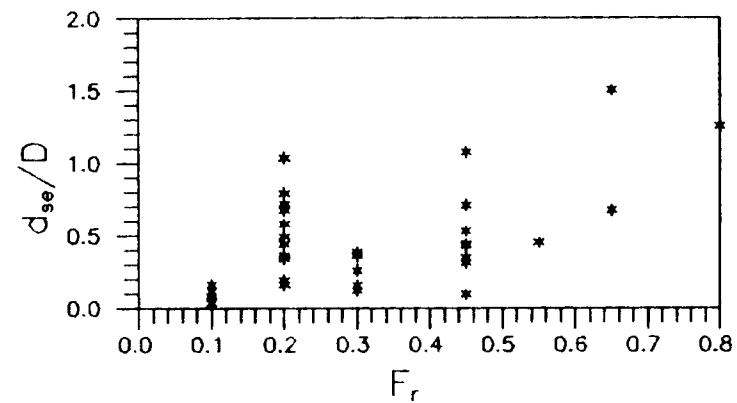
(b) d_{se}/D vs. F_r
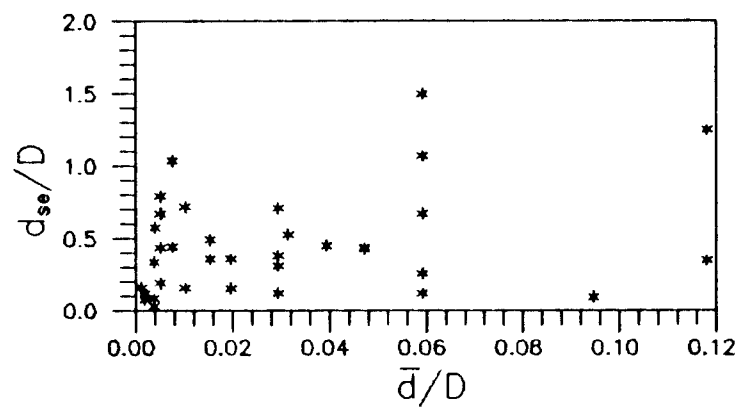
(c) d_{se}/D vs. $\bar{d}/D$

Figure 43. d_{se}/D vs. b/D, F_r and $\bar{d}/D$ at cubes in clear-water scour.

value when live-bed scour occurred.

Breusers et al. (1977), after extensive study of experimental data on maximum equilibrium scour depth at bridge piers, arrived at the following design formula for clear-water scour:

$$d_{se}/b = \beta \; [2 \; (\bar{U}/\bar{U}_c) - 1] \; [2 \; tanh(D/b)] \qquad 5.1$$

where $\beta = 1.0$ for a circular pier, and $\beta = 1.3$ for a rectangular pier; and $0.5 < \bar{U}/\bar{U}_c < 1.0$ for creating the clear-water scour at a bridge pier.

Baker (1980) derived a similar formula semi-empirically which adds more physical reasoning to Equation 5.1. Baker (1981) further modified the constant of the tanh (D/b) term in Equation 5.1 to account for the effect of the relative roughness of the bed material $\bar{d}/D$ upon d_{se}/b. This leads to the following design formula for the clear-water scour at a bridge pier in turbulent flow:

$$d_{se}/b = \beta \; [2 \; (\bar{U}/\bar{U}_c) - 1] \; [81.25 \; (\bar{d}/D) + 0.57] \; [tanh(D/b)] \qquad 5.2$$

Based on these essential findings for bridge pier scour and because the main scour mechanism at isolated obstacles in this study is the horseshoe vortex, a similar type of equation in terms of relative obstacle width is assumed in this research to fit the maximum equilibrium scour depth at isolated cubes on movable beds in clear-water scour.

Equation 5.2 is further modified in order to consider the effect of obstacle shape upon incipient local scour at the obstacle and also to consider the negligible effect of bed roughness and flow velocity, at certain values, upon maximum equilibrium scour depth at obstacle. The general form of the relationship can be given as:

$$d_{se}/D = \{k1 + [k2 \; tanh(k3 \; F_r^{k4} \; D/\bar{d})]\} \; [tanh(k5 \; b/D)] \qquad 5.3$$

where k1, k2, k3, k4 and k5 are constants which can be obtained by the best fit of the experimental results from Table 8. A nonlinear regression of Equation 5.3 by this approach yields the following formula:

$$d_{se}/D = \{-1.30 + [4.75 \; tanh(0.47 \; F_r^{2.56} \; D/\bar{d})]\} \; [tanh(0.215 \; b/D)] \qquad 5.4$$

The coefficient of determination R^2 of Equation 5.4 is 0.97. This indicates a very high correlation between the observed d_{se}/D and the predicted d_{se}/D. Figure 44 shows the results of observed d_{se}/D versus predicted d_{se}/D. The standard error of estimate is 0.062, which is 13.4% of the observed mean value of d_{se}/D.

The influence of relative cube width b/D, flow Froude Number F_r, and relative roughness of the bed material $\bar{d}/D$ on the maximum relative equilibrium scour depth d_{se}/D becomes clear when the experimental results and the predictions of Equation 5.4 are presented with each of these key parameters separately isolated. Figure 45 indicates the influence of b/D on d_{se}/D at several different $D/\bar{d}$ values when F_r is keep constant at 0.20. The d_{se}/D seems to increase linearly with b/D up to b/D = 1.5 approximately. The rate of increase of d_{se}/D then decreases as b/D continues to increase. The d_{se}/D vs. b/D curves shift upward in Figure 45 with each incremental increase of $D/\bar{d}$ but the spacing between successive curves decreases. It indicates that d_{se}/D also increases as $D/\bar{d}$ increases. However, the influence of $D/\bar{d}$ on d_{se}/D is decreased when $D/\bar{d}$ continues to increase. Figure 46 indicates a similar influence of b/D on d_{se}/D when Froude Number varies. Figure 47 directly shows
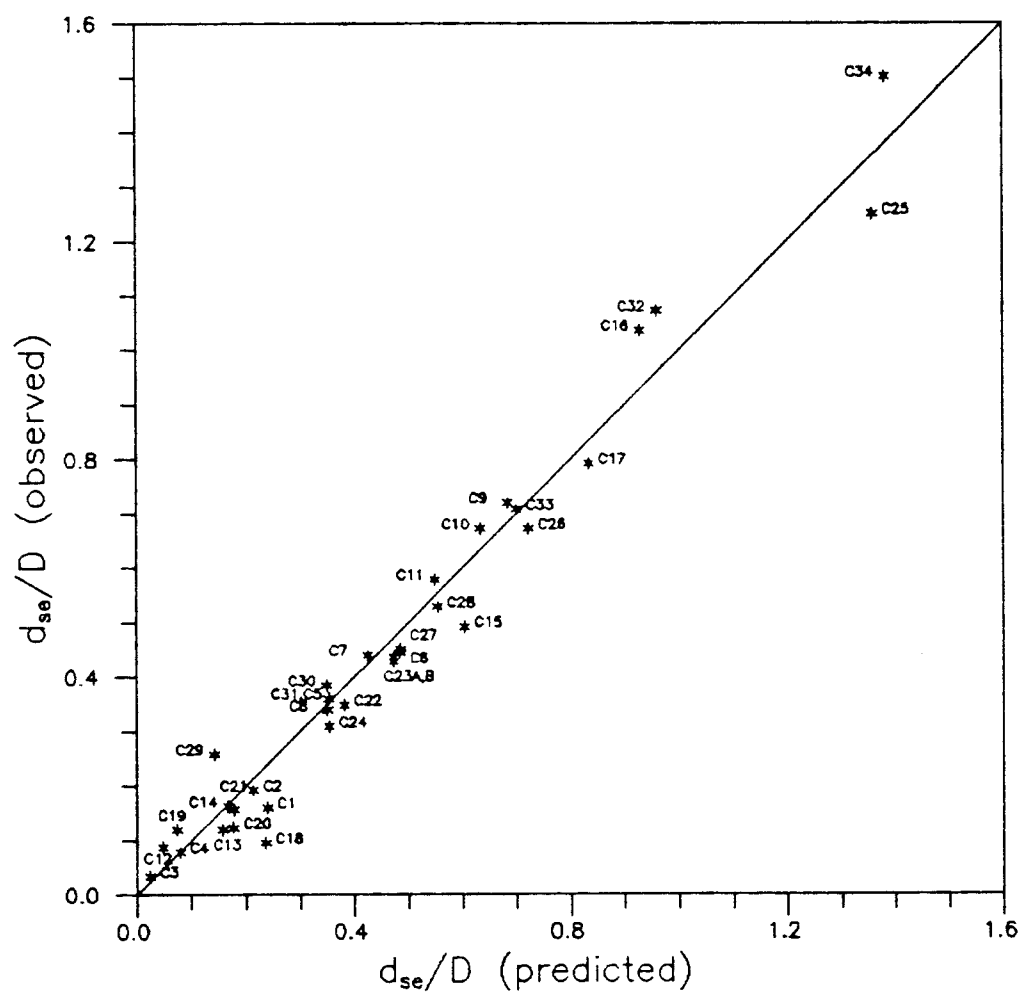
Figure 44.   Comparison of observed d_{se}/D and predicted d_{se}/D of Equation 5.4 at cube in clear-water scour.
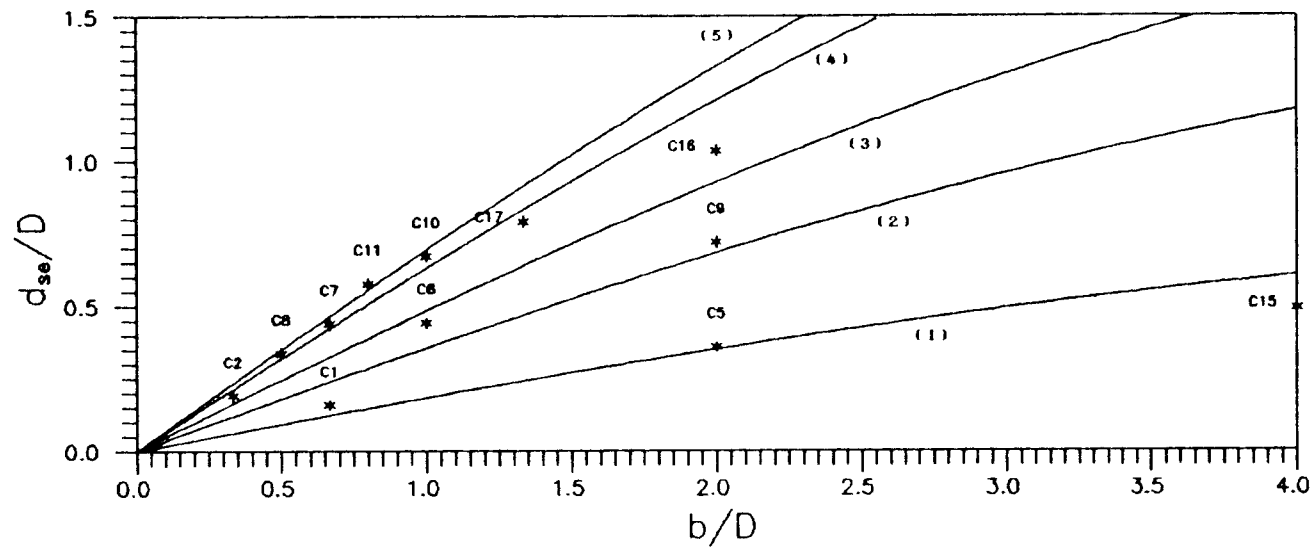
Key: (1) $D/\bar{d}$ = 65.13;   (2) $D/\bar{d}$ = 97.69;   (3) $D/\bar{d}$ = 130.26;   (4) $D/\bar{d}$ = 195.39;
       (5) $D/\bar{d}$ = 260.52.

Figure 45. d_{se}/D Vs. b/D at cube for variable flow relative roughness in
             clear-water scour at constant Froude Number (F_r= 0.20).
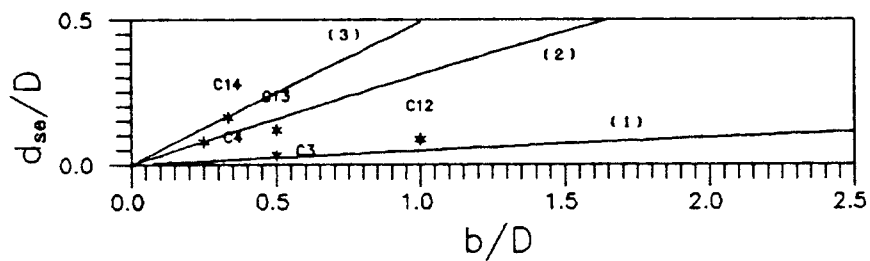
Key: (1) D/d̄ = 260.52; (2) D/d̄ = 521.03; (3) D/d̄ = 781.54.

(a) F_r = 0.10
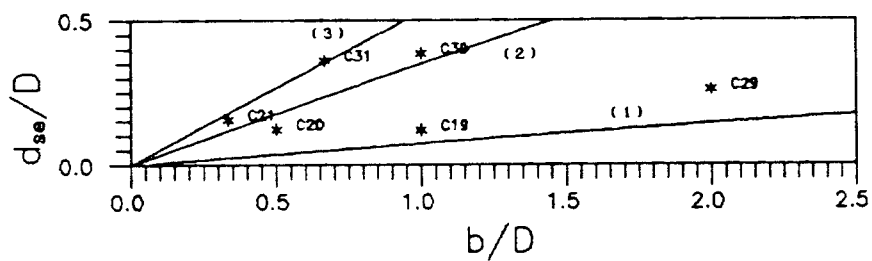
Key: (1) D/d̄ = 16.93; (2) D/d̄ = 33.87; (3) D/d̄ = 50.80.

(b) F_r = 0.30

Figure 46. d_{se}/D vs. b/D at cube for variable flow relative roughness in clear-water scour for several Froude Numbers.
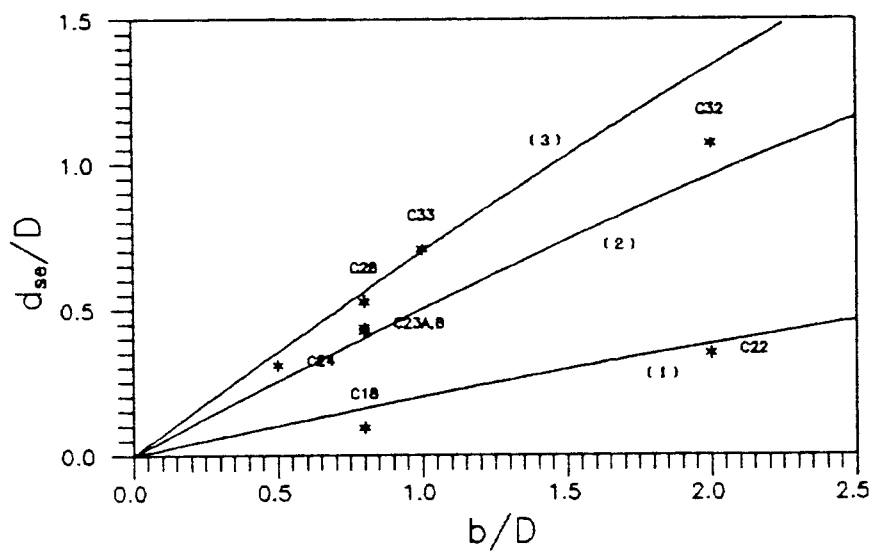
Key: (1) $D/\overline{d}$ = 8.47; (2) $D/\overline{d}$ = 16.93; (3) $D/\overline{d}$ = 33.87.

(c) F_r = 0.45
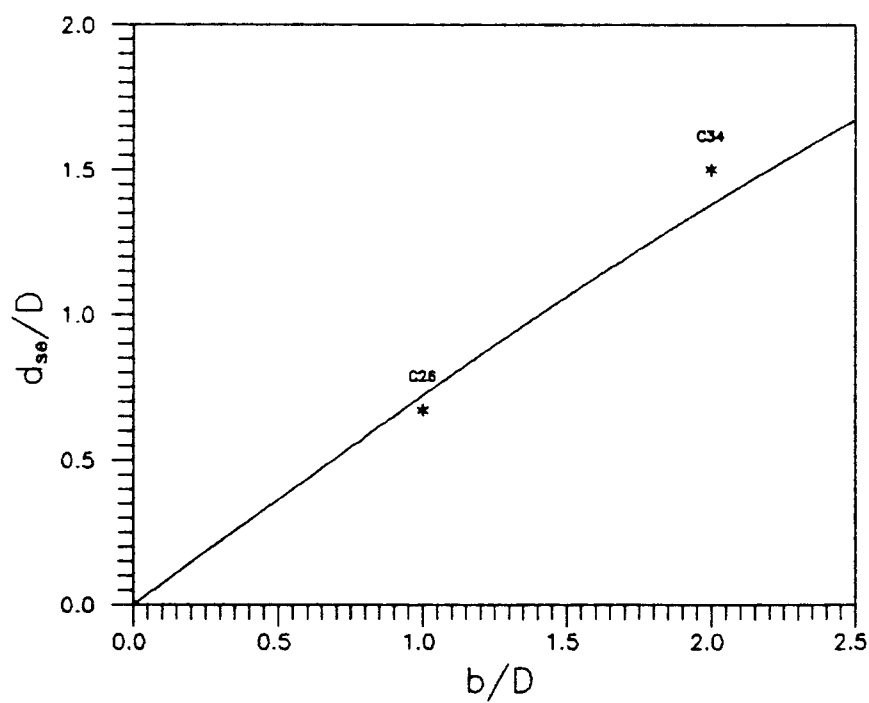
(d) F_r = 0.65 ($D/\overline{d}$ = 16.93).

Figure 46. Continued.
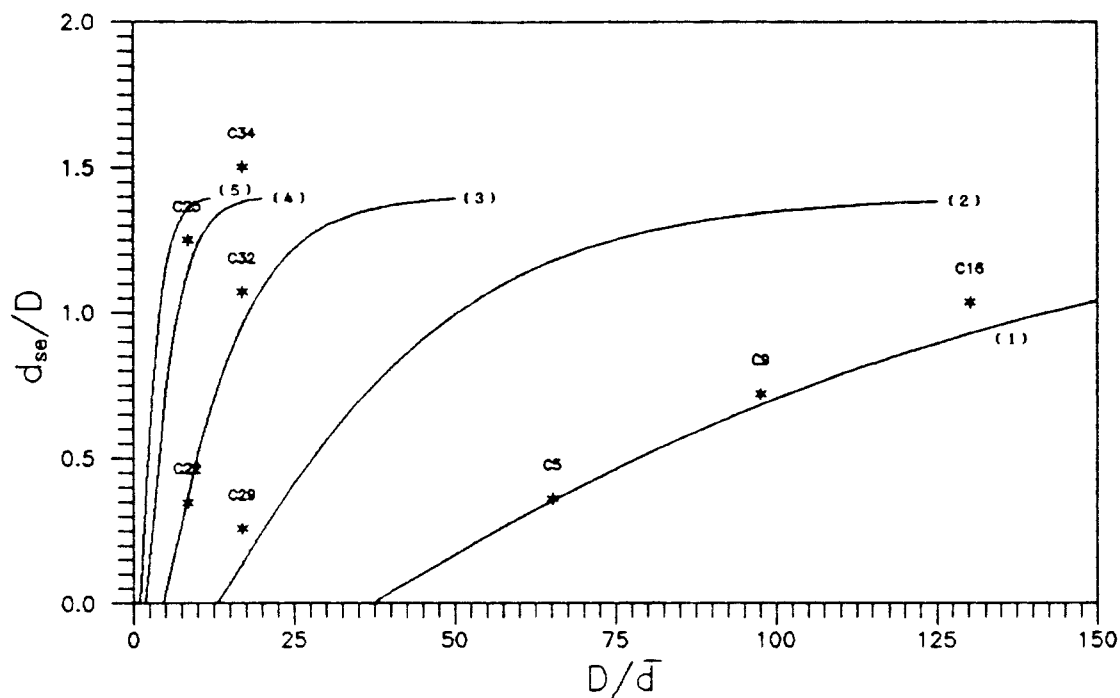
Key: (1) F_r = 0.20; (2) F_r = 0.30; (3) F_r = 0.45; (4) F_r = 0.65;
      (5) F_r = 0.80.

(a) b/D = 2.0
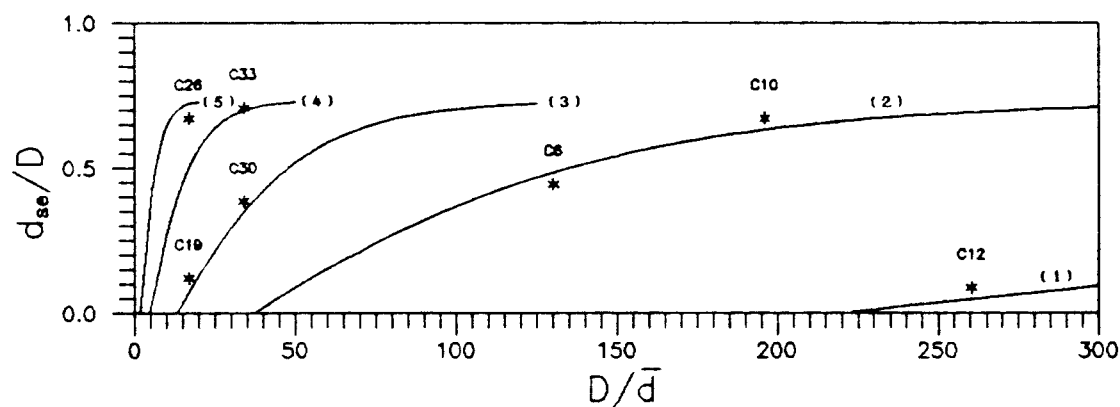
Key: (1) F_r = 0.10; (2) F_r = 0.20; (3) F_r = 0.30; (4) F_r = 0.45;
      (5) F_r = 0.65.

(b) b/D = 1.0

Figure 47. d_{se}/D vs. $D/\bar{d}$ at cube for variable Froude Number in
clear-water scour with several relative obstacle sizes.
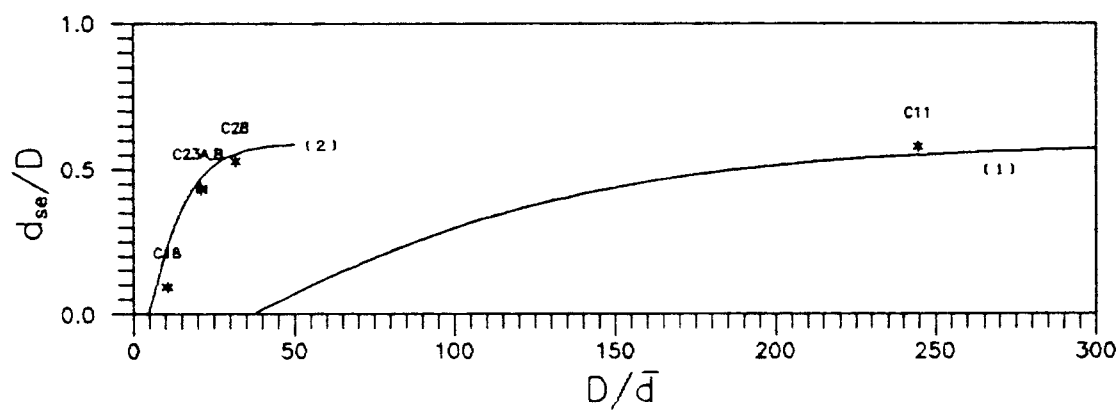
Key: (1) F_r = 0.20; (2) F_r = 0.45.

(c) b/D = 0.80
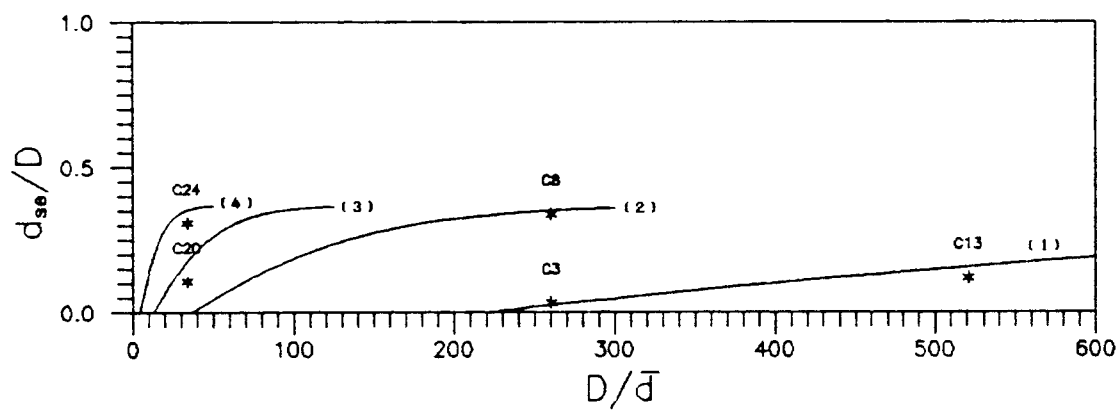
Key: (1) F_r = 0.10; (2) F_r = 0.20; (3) F_r = 0.30; (4) F_r = 0.45.

(d) b/D = 0.5

Figure 47. Continued.

the influence of $D/\bar{d}$ on d_{se}/D at several different F_r and several

values of b/D. Each curve in Figure 47 indicates that the increase

of $D/\bar{d}$ increases d_{se}/D. The influence tends to become small when

$D/\bar{d}$ is close to the critical $D/\bar{d}$ for incipient motion of the bed

material upstream of the cube. An increase of F_r in each figure

tends to move the constant F_r curve closer to the origin of $D/\bar{d}$.

This indicates that the critical $D/\bar{d}$ for incipient motion of the bed

material at a cube and upstream of a cube are both decreased as F_r

is increased. Figure 48 directly shows the influence of F_r on d_{se}/D

at several different b/D for selected values of $D/\bar{d}$. Each curve in

Figure 48 indicates that the increase of F_r increases d_{se}/D. The

influence tends to become small when F_r is close to the critical F_r

for incipient motion of the bed material upstream of the cube.

According to Graf (1971), Neill presented a conservative design

curve in 1967 for the incipient motion of coarse, uniform bed

materials. It can be given with the following equation:

$$\bar{U}^2/[(\rho_s/\rho)g\bar{d}] = 2.50 \ (\bar{d}/D)^{-0.20} \qquad\qquad 5.5$$

For sand/gravel bed materials, $\rho_s/\rho = 2.60$ is a good approximation.

Equations 5.5 can then be expressed as

$$F_r = 2.00 \ (D/\bar{d})^{-0.40} \qquad\qquad 5.6$$

This can be used as the upper limit of F_r and $D/\bar{d}$ in Equation 5.4 to

maintain clear-water scour at a cube. The critical condition for

incipient motion of the bed material at a cube in clear-water scour

can be estimated when the maximum relative equilibrium scour depth

d_{se}/D in Equation 5.4 is set to zero. This is:

$$-1.30 + [4.75 \tanh(0.47 \ F_r^{2.56} \ D/\bar{d})] = 0 \qquad\qquad 5.7$$
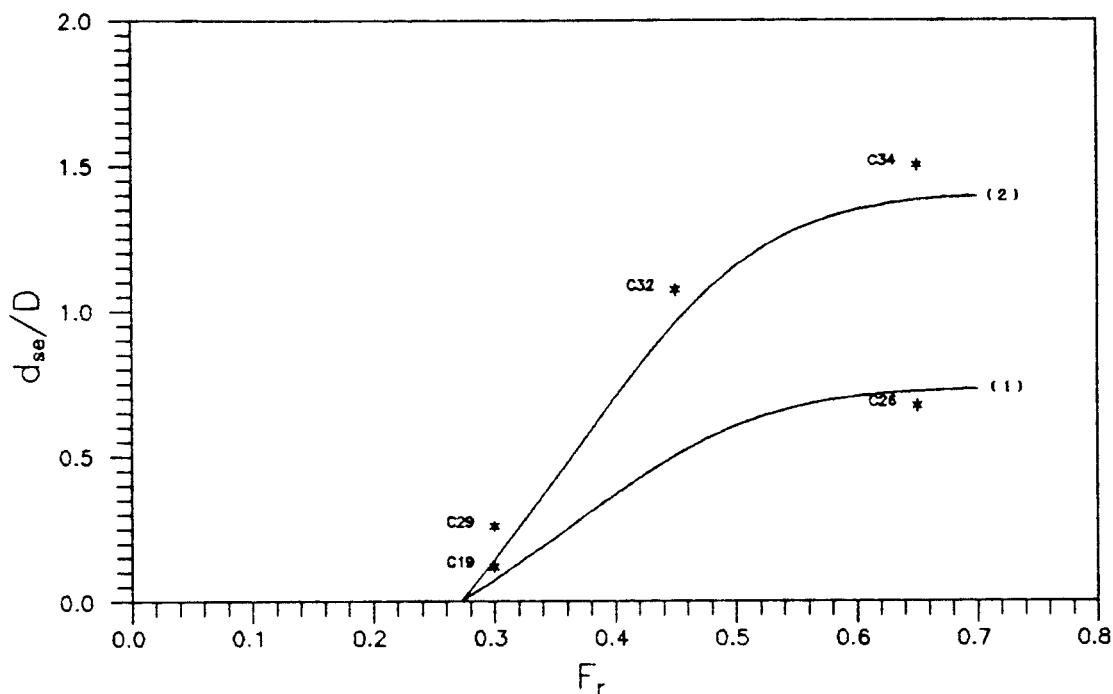
Key: (1) b/D = 1.0; (2) b/D = 2.0.

(a) D/d̄ = 16.93
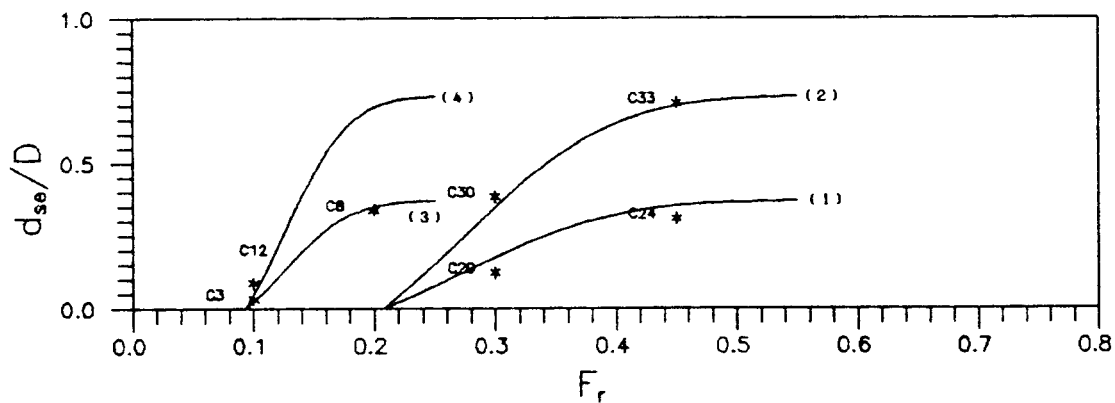
Key: (1) b/D = 0.5 (D/d̄ = 33.86); (2) b/D = 1.0 (D/d̄ = 33.86);
     (3) b/D = 0.5 (D/d̄ = 260.52); (4) b/D = 1.0 (D/d̄ = 260.52).

(b) D/d̄ = 33.86 and 260.52.

Figure 48. d_{se}/D vs. F_r at cube for variable b/D in clear-water
           scour for several flow relative roughnesses.
           (D/d̄ = 16.93, 33.86 and 260.52).

The explict solution of Equation 5.7 in term of F_r and $D/\bar{d}$ becomes

$$F_r = 0.82 \ (D/\bar{d})^{-0.39} \qquad\qquad 5.8$$

This can be used as the lower limit of F_r and $D/\bar{d}$ in Equation 5.4 to

create local scour at a cube in clear-water scour. Figure 49 shows

the experimental range of F_r and $D/\bar{d}$ and the two curves of Equation

5.6 and 5.8. The zone within these two curves indicates the F_r and

$D/\bar{d}$ values which can create local scour at a cube on a sand/gravel

bed for clear-water scour conditions.

Based on Equations 5.4 and 5.6, some inferences can be made

about the d_{se}/D at a cube on a sand/gravel bed when the clear-water

scour is near the critical condition for incipient motion of the

upstream bed material. Substituting the critical F_r of Equation 5.6

into Equation 5.4, gives the approximation

$$d_{se}/D = 3.45 \ \tanh \ (0.215 \ b/D) \qquad\qquad 5.9$$

This equation indicates that the maximum relative equilibrium scour

depth d_{se}/D at a cube only depends upon the relative cube width b/D.

If the cube size b were relatively large, say $b/D > 10$ in Equation

5.9, the maximum equilibrium scour depth d_{se} at the cube will be

approximately 3.45 times the water depth D. But if the cube size b

were relatively small, say $b/D < 1.5$, the maximum equilibrium scour

depth d_{se} at the cube will be approximately 0.74 times the cube

width b. For bridge pier scour, Breusers et al. (1977) and Baker

(1980, 1981) also concluded that the d_{se}/D at a bridge pier only

depended upon b/D as the flow condition reached the incipient motion

of the upstream bed material. According to their work, the maximum

relative equilibrium scour depth d_{se}/D at a rectangular pier can be
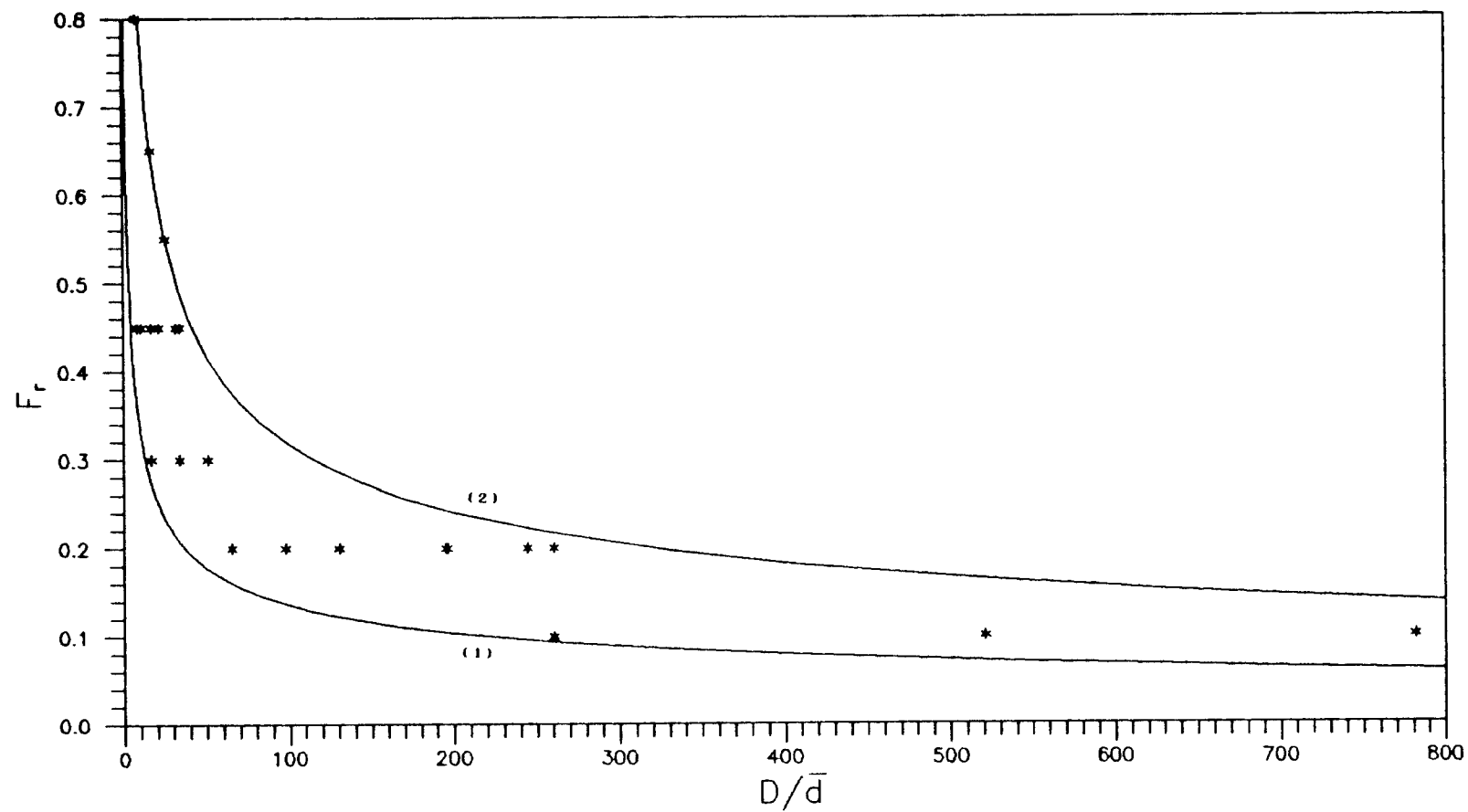
Key: (1) Equation 5.8 (Cube, present research); (2) Equation 5.6
     (Neill, 1967)

Figure 49.   The range of F_r and $D/\bar{d}$ to cause local scour at cube on
             sand/gravel bed for clear-water scour conditions.

predicted by the following equation

$$d_{se}/D = 2.60 \ (b/D) \ \tanh \ (D/b) \qquad\qquad 5.10$$

Figure 50 shows the comparison of the d_{se}/D at a cube on a

sand/gravel bed and the d_{se}/D at a rectangular pier when the flow

condition reaches the incipient motion of the upstream bed material.

It indicates that the d_{se}/D at the cube is smaller than the d_{se}/D at

the rectangular pier within the range of $0 < b/D < 4.4$. But it is

larger instead when $b/D > 4.4$.

Figure 51 shows comparisons of the maximum relative

equilibrium scour depth d_{se}/D at a cube, a circular cylinder and a

sphere on a movable bed under similar flow conditions. The obstacle

sizes b are all two inches. In Figure 51(a), the upstream approach

water depths D of each obstacle on a sand bed changes but the flow

Froude Number F_r remains constant at 0.20. In Figure 51(b), the bed

material changes to gravel and F_r increases to 0.45. The decrease

of water depth leads to the increase of relative obstacle width b/D

and relative roughness of the bed material $\bar{d}/D$ at the same time.

The d_{se}/D at the cube increases with b/D until the effect of b/D can

no longer dominate over the effect of $\bar{d}/D$. The d_{se}/D then begins to

decrease with the continuing increase of $\bar{d}/D$ until the bed material

becomes relatively too rough to be scoured away. The curves for the

cube in Figure 51(a) and 51(b) are obtained by Equation 5.4. In

Figure 51(a), the experimental results at the circular cylinder and

the sphere indicate similar trends to those for the cube but have

less d_{se}/D when the effect of $\bar{d}/D$ begins to be revealed and finally

dominate over the effect of b/D. As the water depth becomes
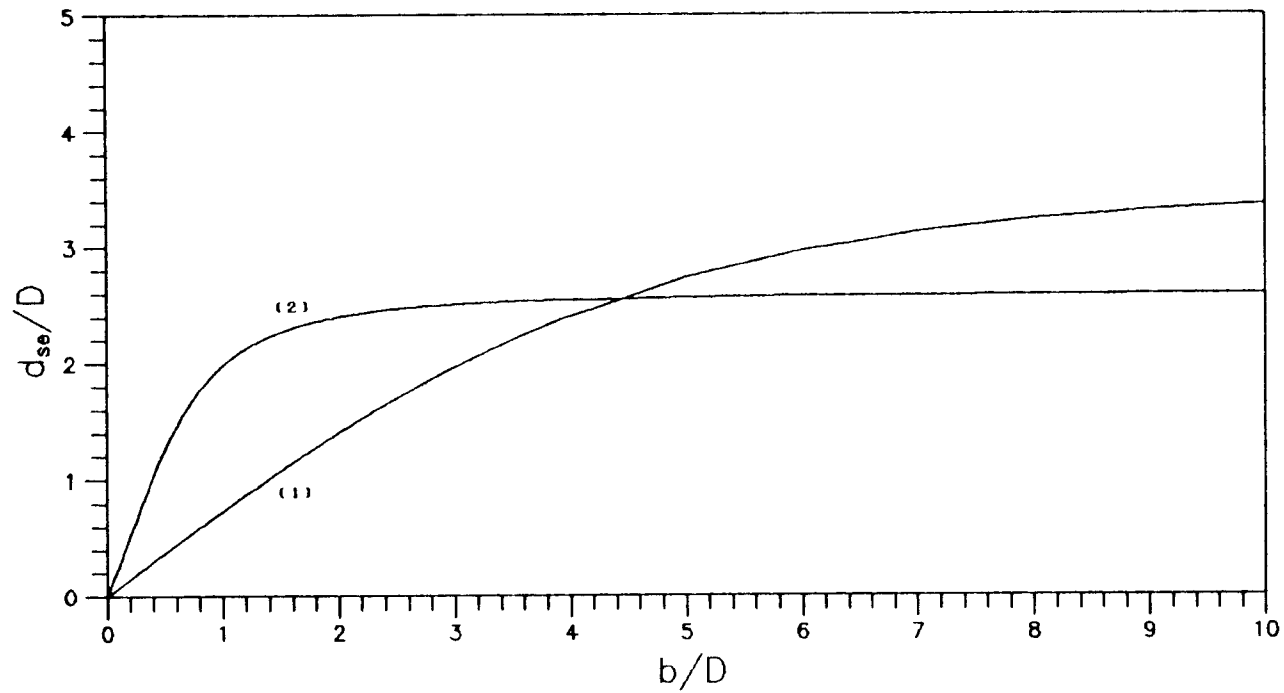
Key: (1) Equation 5.9 (Cube, present research); (2) Equation 5.10 (Rectangular bridge pier, Breusers et al. (1977) and Baker (1980, 1981)).

Figure 50. Comparison between d_{se}/D vs. b/D at cube on sand/gravel bed and that at rectangular bridge pier.
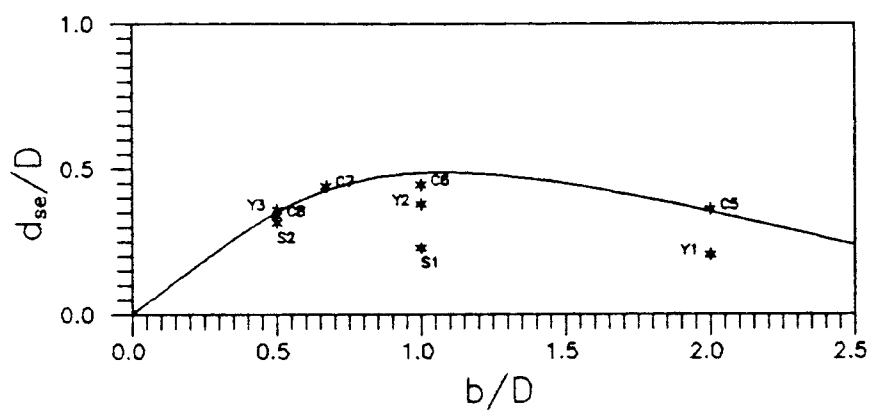
(a) $F_r = 0.20$ (sand bed)
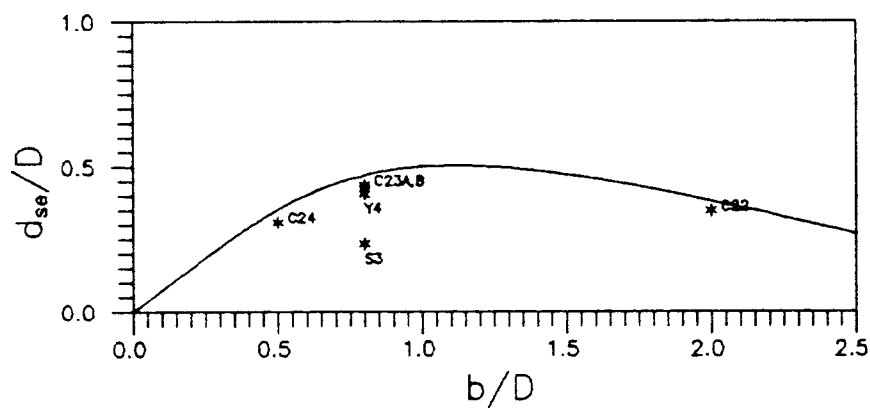
(b) $F_r = 0.45$ (gravel bed)

Figure 51. Comparison of d_{se}/D at cube, at circular cylinder and at sphere on sand/gravel bed in clear-water scour.

relatively deep, the shape effect of the circular cylinder and the sphere seems to become negligible.

Figure 52 relates the cubic root of the relative equilibrium scour volume V_{se}/D^3 to the maximum relative equilibrium scour depth d_{se}/D at isolated cubes on a sand/gravel bed in clear-water scour. It shows a simple linear relationship. The linear regression which satisfies the zero scour depth and scour volume at the origin of the coordinate axes gives the following equation

$$V_{se}^{\frac{1}{3}}/D = 2.10 \; d_{se}/D \hspace{3cm} 5.11$$

The coefficient of determination R^2 of Equation 5.11 is 0.93. This indicates a very high correlation between the observed $V_{se}^{\frac{1}{3}}/D$ and d_{se}/D. The standard error of estimate is 0.189, which is 19.7% of the observed mean value of $V_{se}^{\frac{1}{3}}/D$. Equation 5.11 represents the cubic root of the equilibrium scour volume as 2.10 times the maximum equilibrium scour depth at the cube. As the clear-water scour reaches the critical condition for incipient motion of the upstream bed material, Equations 5.11 infers that the equilibrium scour volume would be approximately 380 times the cubic power of the water depth if the cube size is relatively very large. However, It would be approximately 3.76 times the cube volume if the cube size is relatively very small compared to the water depth.

Figure 53 shows the $V_{se}^{\frac{1}{3}}/D$ vs. d_{se}/D at a cube, a circular cylinder and a sphere on a sand/gravel bed in clear-water scour at $F_r = 0.20$ and 0.45. The widths of the obstacles are all two inches but the upstream approach water depth changes. It shows a simple linear relationship between $V_{se}^{\frac{1}{3}}/D$ and d_{se}/D despite the difference of
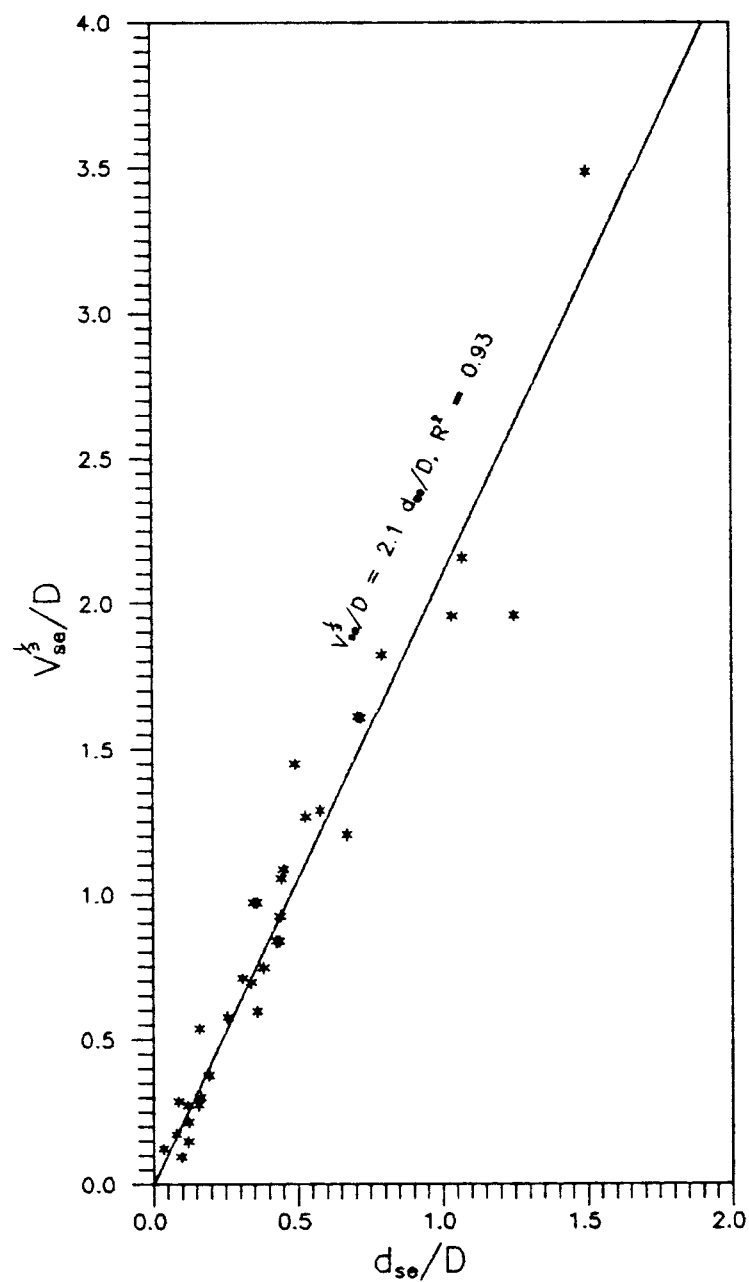
Figure 52. $V_{se}^{1/3}/D$ vs. d_{se}/D at cube in clear-water scour.
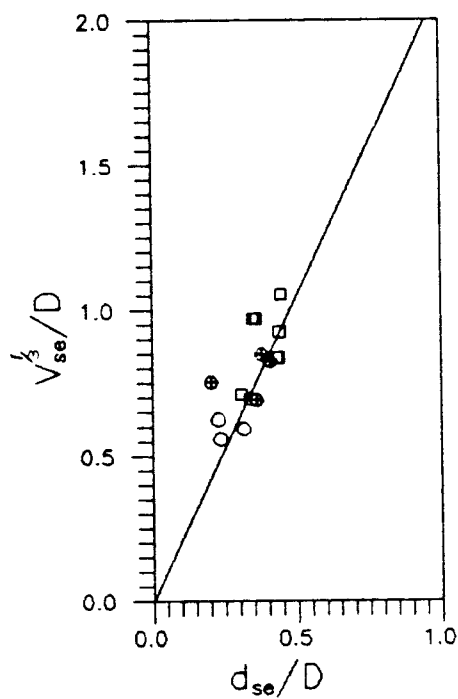
Key: □ --- cube; ⊕ --- Circular cylinder; ○ --- sphere

Figure 53. $V_{se}^{1/3}/D$ Vs. d_{se}/D at two-inch cube, circular cylinder and sphere in clear-water scour.

the obstacle shape. A simple linear regression that includes all the experimental results for the cube, the circular cylinder and the sphere gives the same equation as Equation 5.11. The coefficient of determination R^2 is 0.93. The standard error of estimate is 0.182, which is 19.8% of the observed mean value of $V_{se}^{\frac{1}{3}}/D$. The equation is shown as a straight line in Figure 53.

Obstacle Displacement and Inclination due to Scour

An isolated obstacle on a movable bed may shift upstream as a consequence of local scour. In the previous section, the movement of the obstacle is described in terms of its displacement (S_i, i = x, y, and z) and inclination ($\Delta\theta_{ij}$, i = x, y, and z; j = z' and x'). Table 9 lists the experimental results involving the relative equilibrium displacement (S_{ie}/D) and equilibrium inclination ($\Delta\theta_{ije}$) of isolated obstacles on a sand/gravel bed.

Figure 54 compares the relative equilibrium longitudinal displacement (S_{xe}/D) and the relative equilibrium side shift (S_{ye}/D) to the relative equilibrium vertical settlement (S_{ze}/D) of the cube. It shows that S_{xe}/D seems to increase linearly in the upstream (-) direction with S_{ze}/D. The S_{ye}/D is approximately zero, on average, and is not related to S_{ze}/D.

Figure 55 compares the equilibrium longitudinal inclination ($\Delta\theta_{zz'e}$, $\Delta\theta_{xx'e}$, and $\Delta\theta_{zx'e}$), the equilibrium side rotation ($\Delta\theta_{yz'e}$) and the equilibrium side twist ($\Delta\theta_{yx'e}$) to the equilibrium longitudinal inclination ($\Delta\theta_{zx'e}$) of the cube. It shows that the longitudinal

Table 9. Relative equilibrium displacement and equilibrium inclination of obstacle in movable-bed experiments.

Obstacle Shape	Bed Material	Run No.	t (hr)	Fr	b/D	ā/D	S₁ₑ/D	Sᵧₑ/D	S₁ₑ/D	Δθᵣₜ (deg)	Δθᵧₜ (deg)	Δθₜₜ (deg)	Δθₜₜ (deg)	Δθᵧₜ (deg)	Δθₜₜ (deg)
Cube	Sand	C1	43.46	0.20	0.67	1.02E-02	-0.488	-0.040	0.176	19.2	1.9	19.3	19.8	5.3	19.8
		C2	24.46	0.20	0.33	5.12E-03	-0.408	-0.044	0.164	24.4	2.7	24.6	25.4	8.4	23.8
		C3	24.15	0.10	0.50	3.84E-03	0.000	0.000	0.000	0.0	0.0	0.0	0.0	0.0	0.0
		C4	48.31	0.10	0.25	1.92E-03	-0.106	-0.009	0.038	15.0	-0.8	15.1	15.1	1.4	15.0
		C5	49.68	0.20	2.00	1.54E-02	0.000	0.080	0.000	0.0	0.0	0.0	0.0	0.0	0.0
		C6	48.79	0.20	1.00	7.68E-03	-0.788	0.060	0.288	21.1	2.6	21.3	21.2	-0.7	21.2
		C7	32.98	0.20	0.67	5.12E-03	-0.951	0.191	0.360	24.9	4.0	25.3	27.8	-8.8	25.3
		C8	39.93	0.20	0.50	3.84E-03	-0.651	-0.072	0.294	31.3	-2.8	31.4	32.3	6.9	31.4
		C9	48.80	0.20	2.00	1.02E-02	-1.096	-0.200	0.490	18.4	-2.5	18.6	18.5	1.2	18.5
		C10	44.01	0.20	1.00	5.10E-03	-1.144	0.028	0.610	30.4	0.8	30.4	30.6	3.7	30.3
		C11	144.00	0.20	0.80	4.09E-03	-1.197	-0.147	0.550	31.5	-4.2	31.9	32.9	7.3	31.9
		C12	47.76	0.10	1.00	3.84E-03	0.000	0.000	0.000	0.0	0.0	0.0	0.0	0.0	0.0
		C13	48.52	0.10	0.50	1.92E-03	-0.165	-0.021	0.058	11.6	-1.2	11.7	11.7	1.3	11.6
		C14	88.64	0.10	0.33	1.28E-03	-0.418	-0.020	0.159	25.5	-2.8	25.7	27.1	8.2	25.7
		C15	45.76	0.20	4.00	1.54E-02	-0.060	0.000	0.012	0.5	0.3	0.6	0.9	0.7	0.5
		C16	49.58	0.20	2.00	7.68E-03	-1.920	0.522	0.744	22.5	7.3	23.7	23.3	-3.1	23.0
		C17	39.77	0.20	1.33	5.12E-03	-1.792	0.396	0.660	22.7	5.4	23.4	24.3	-6.6	23.3
	Gravel	C18	1.87	0.45	0.80	9.45E-02	0.000	0.000	0.000	0.0	0.0	0.0	0.0	0.0	0.0
		C19	1.03	0.30	1.00	5.91E-02	0.000	0.000	0.000	0.0	0.0	0.0	0.0	0.0	0.0
		C20	24.45	0.30	0.50	2.95E-02	-0.030	-0.003	0.024	8.4	-0.3	8.4	8.5	1.1	8.4
		C21	51.25	0.30	0.33	1.97E-02	-0.210	-0.042	0.108	22.4	-2.2	22.5	23.1	5.1	22.5
		C22	45.92	0.45	2.00	1.18E-01	-0.336	0.000	0.072	4.6	0.1	4.6	4.7	-0.7	4.6
		C23A	50.73	0.45	0.80	4.72E-02	-0.658	0.053	0.365	26.7	-0.4	26.7	26.7	0.0	26.7
		C23B	51.00	0.45	0.80	4.72E-02	-0.624	-0.034	0.384	27.9	1.4	27.9	27.9	1.8	27.8
		C24	48.12	0.45	0.50	2.95E-02	-0.567	-0.038	0.338	34.2	-2.7	34.4	34.3	0.0	34.3
		C25	47.82	0.80	2.00	1.18E-01	-1.224	0.456	0.756	25.7	7.3	26.8	26.4	-2.0	26.2
		C26	48.97	0.65	1.00	5.91E-02	-0.780	-0.150	0.534	30.8	-6.8	31.7	31.7	3.8	31.4
		C27	26.70	0.55	0.67	3.94E-02	-0.672	0.088	0.460	36.1	5.6	36.7	36.8	-3.8	36.6
		C28	73.64	0.45	0.80	3.15E-02	-0.998	0.000	0.573	32.7	0.4	32.7	32.7	0.7	32.7
		C29	9.24	0.30	2.00	5.91E-02	0.000	0.000	0.000	0.0	0.0	0.0	0.0	0.0	0.0
		C30	52.98	0.30	1.00	2.95E-02	-0.504	-0.060	0.237	19.4	-1.6	19.5	19.6	2.8	19.4
		C31	50.00	0.30	0.67	1.97E-02	-0.606	-0.129	0.429	24.4	-3.2	24.6	24.7	2.6	24.5
		C32	49.47	0.45	2.00	5.91E-02	-2.112	-0.030	1.020	27.9	0.1	27.9	27.9	0.7	27.9
		C33	28.39	0.45	1.00	2.95E-02	-1.203	0.057	0.717	31.9	3.1	32.0	31.9	0.9	31.9
		C34	31.20	0.65	2.00	5.91E-02	-2.166	-0.162	1.308	24.6	-1.9	24.7	25.1	4.1	24.7
Cylinder	Sand	T1	26.93	0.20	2.00	1.54E-02	0.000	0.000	0.000	0.0	0.0	0.0	0.0	0.0	0.0
		T2	49.27	0.20	1.00	7.68E-03	-1.077	0.002	0.406	18.5	-2.0	18.7	20.8	8.8	18.6
		T3	48.58	0.20	0.50	3.84E-03	-1.015	0.147	0.371	27.1	4.3	27.5	28.9	-8.2	27.5
	Gravel	T4	48.21	0.45	0.80	4.72E-02	-0.581	-0.072	0.365	22.6	-2.9	22.8	24.0	7.2	22.8
Sphere	Sand	S1	48.18	0.20	1.00	7.68E-03	-0.698	0.000	0.288	41.0	-4.7	41.4	41.1	-2.0	41.0
		S2	49.66	0.20	0.50	3.84E-03	-0.859	0.105	0.699	141.2	5.2	140.8	140.8	6.6	140.7
	Gravel	S3	48.46	0.45	0.80	4.72E-02	-0.490	0.096	0.302	32.5	0.8	32.5	33.9	5.2	32.4

(a) S_{xe}/D vs. S_{ze}/D

(b) S_{ye}/D vs. S_{ze}/D
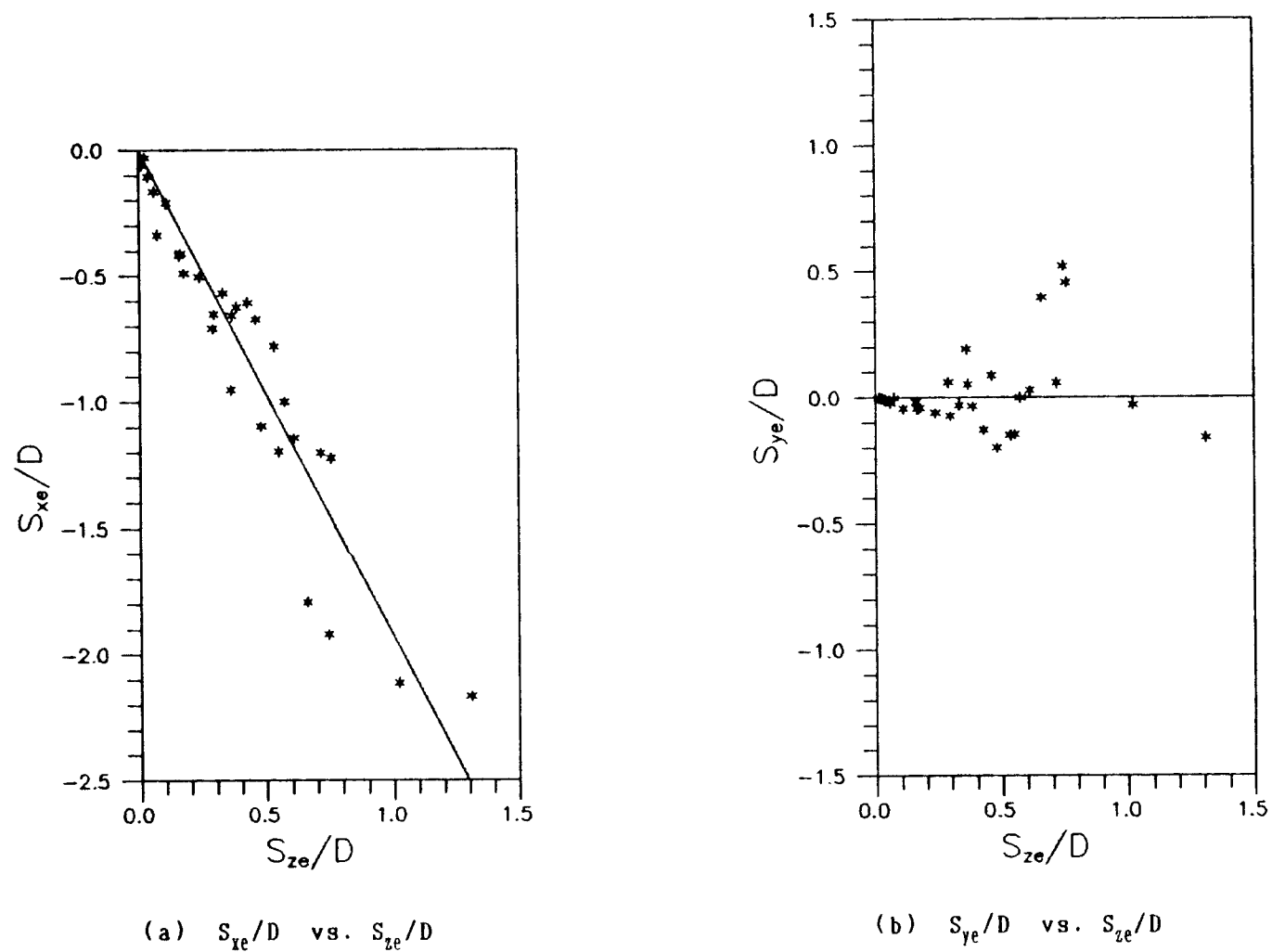
Figure 54. Relative longitudinal displacement (S_{xe}/D) and side shift (S_{ye}/D) vs. vertical settlement (S_{ze}/D) of cube at equilibrium in clear-water scour.
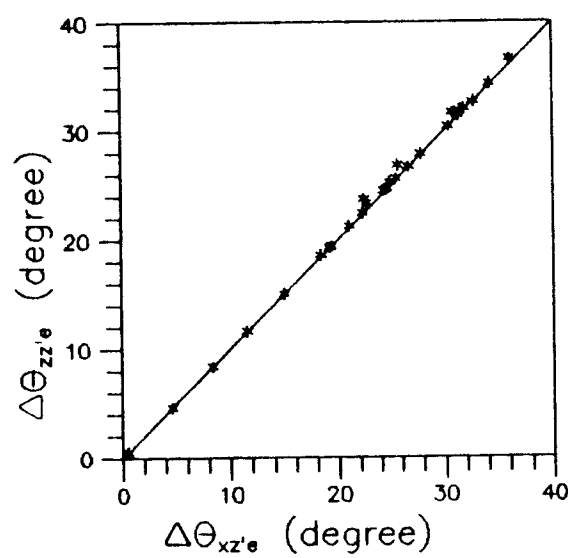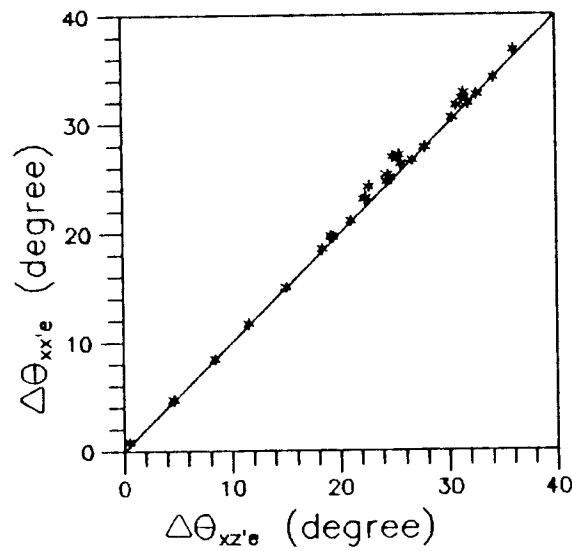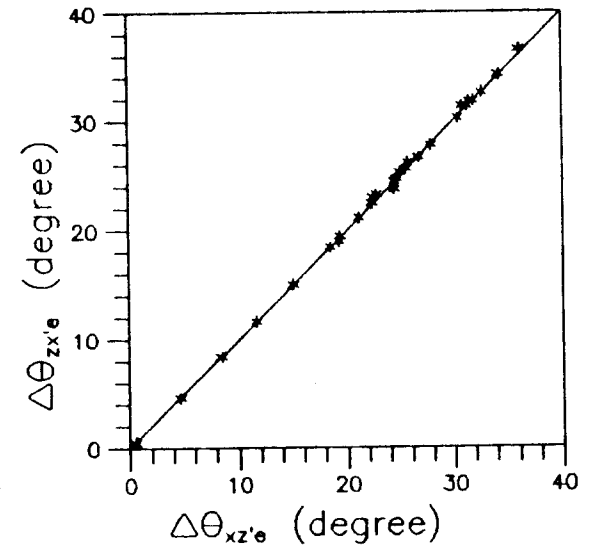
Figure 55. Longitudinal inclination ($\Delta\theta_{zz'e}$, $\Delta\theta_{xx'e}$, $\Delta\theta_{zx'e}$), side rotation ($\Delta\theta_{yz'e}$) and side twist ($\Delta\theta_{yx'e}$) vs. longitudinal inclination ($\Delta\theta_{xz'e}$) of cube at equilibrium in clear-water scour.
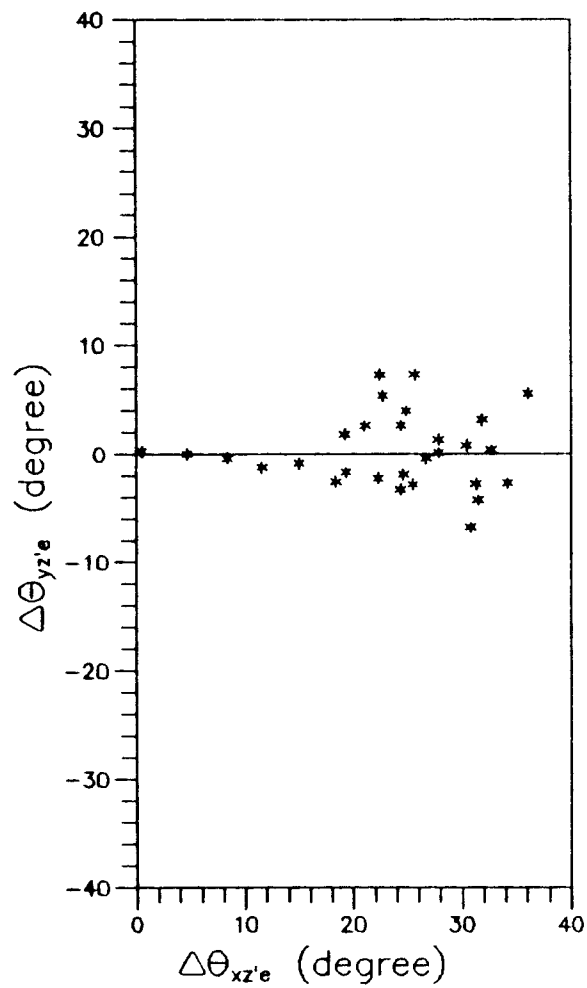
(d) $\Delta\theta_{yz'e}$ vs. $\Delta\theta_{xz'e}$
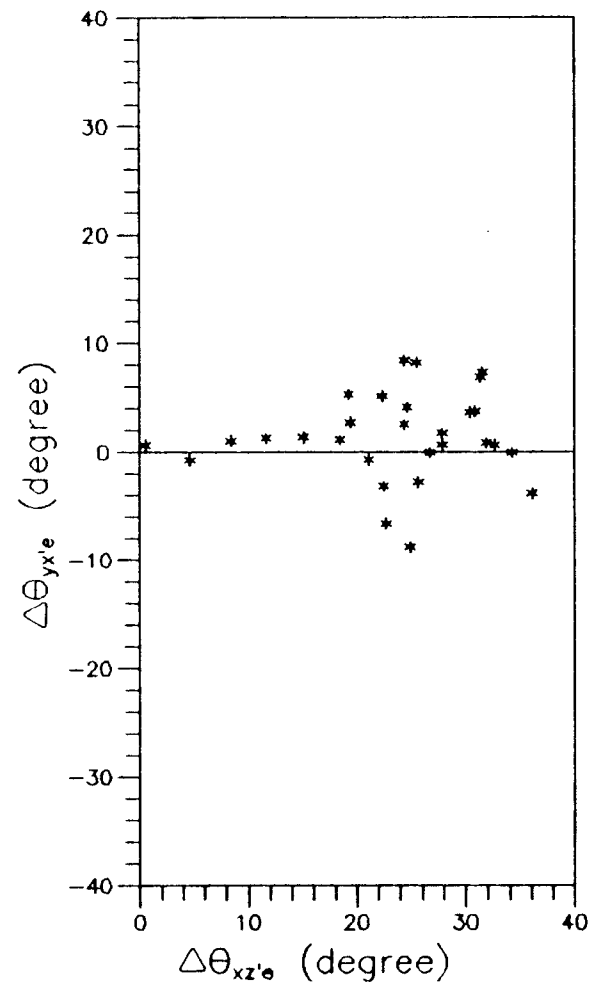
(e) $\Delta\theta_{yx'e}$ vs. $\Delta\theta_{xz'e}$

Figure 55. Continued.

inclinations $\Delta\theta_{zz'e}$, $\Delta\theta_{xx'e}$, $\Delta\theta_{zx'e}$ and $\Delta\theta_{xz'e}$ are nearly equal. The side rotations and side twists, $\Delta\theta_{yz'e}$ and $\Delta\theta_{yx'e}$, are approximately zero, on average, and are not dependent upon the longitudinal inclinations ($\Delta\theta_{xz'e}$).

These figures indicate that the major relative equilibrium movement of the cube can be described by the relative equilibrium longitudinal displacement S_{xe}/D, relative equilibrium vertical settlement S_{ze}/D and longitudinal inclination $\Delta\theta_{xz'e}$. The linear regression which satifies the zero S_{xe} and S_{ze} at the origin of the coordinate axes in Figure 54(a) gives the following equation:

$$S_{xe}/D = 1.93 \, S_{ze}/D \qquad\qquad 5.12$$

The coefficient of determination R^2 of Equation 5.12 is 0.88. This indicates a high correlation between the observed S_{xe}/D and S_{ze}/D. The standard error of estimate is 0.204, which is 24.8% of the observed mean value of S_{xe}/D.

The cube movement is a consequence of local scour. Therefore, the functions of $\Delta\theta_{xz'e}$ and S_{ze}/D are expected to have some analogy with the function of d_{se}/D, as indicated in Equation 5.4. When a cube becomes relatively small compared to the water depth, Equation 5.4 indicates that the maximum equilibrium scour depth at a cube is hardly affected by the water depth. It is expected that the $\Delta\theta_{xz'e}$ and the S_{ze} of the cube will not be affected by the water depth either. If a cube becomes relatively large compared to the water depth, Equation 5.4 infers that the maxium equilibrium scour depth at the cube will be only affected by the water depth. It is expected that the cube will keep stationary during local scour and

the $\Delta\theta_{xz'e}$ and the S_{ze} of the cube will be zero. Based on this reasoning for the possible functions of $\Delta\theta_{xz'e}$ and S_{ze}/D at the cube, the following equations are assumed to fit the experimental results of the cube:

$$\Delta\theta_{xz'e} = \{m1 + [m2 \ tanh(m3 \ F_r^{m4} \ D/\bar{d})]\} \ x$$

$$\{0.5 - 0.5 \ tanh[0.506(b/D - 5.75)]\} \qquad\qquad 5.13$$

$$S_{ze}/D = \{n1 + [n2 \ tanh(n3 \ F_r^{n4} \ D/\bar{d})]\} \ x$$

$$\{0.5 - 0.5 \ tanh[0.506(b/D - 5.75)]\} \ [tanh(0.215 \ b/D)] \quad 5.14$$

Here, m1, m2, m3, m4, n1, n2, n3, and n4 are constants which can be obtained by the best fit of the experimental results in Table 9. The nonlinear regressions of Equations 5.13 and 5.14 with the observed non-zero $\Delta\theta_{xz'e}$ and S_{ze}/D data points yield the following formulas:

$$\Delta\theta_{xz'e} = \{-45.0 + [75.4 \ tanh(0.71 \ F_r^{2.56} \ D/\bar{d})]\} \ x$$

$$\{0.5 - 0.5 \ tanh[0.506(b/D - 5.75)]\} \qquad\qquad 5.15$$

$$S_{ze}/D = \{-4.19 + [7.00 \ tanh(0.76 \ F_r^{2.66} \ D/\bar{d})]\} \ x$$

$$\{0.5 - 0.5 \ tanh[0.506(b/D - 5.75)]\} \ [tanh(0.215 \ b/D)] \quad 5.16$$

The coefficients of determination R^2 for Equations 5.15 and 5.16 are 0.85 and 0.89, respectively. They indicate high correlations between the observed $\Delta\theta_{xz'e}$, S_{ze}/D and the predicted $\Delta\theta_{xz'e}$, S_{ze}/D. Figure 56 shows the results of the observed $\Delta\theta_{xze'}$ and the predicted $\Delta\theta_{xz'e}$. The standard error of estimate is 3.3 degrees, which is 14.2% of the observed mean value of $\Delta\theta_{xz'e}$. Figure 57 shows the results of the observed S_{ze}/D and the predicted S_{ze}/D. The standard error of estimate is 0.103, which is 25.0% of the observed mean value of S_{ze}/D.
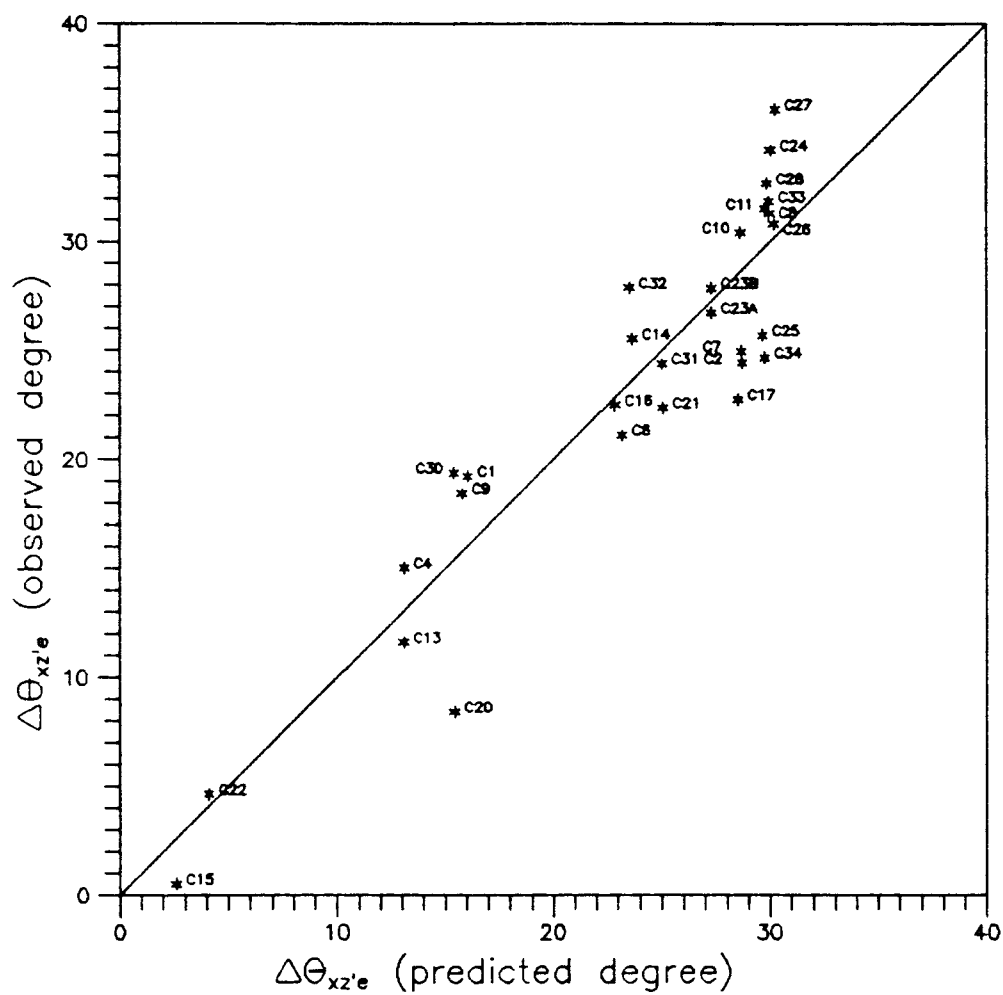
Figure 56. Comparison of observed $\Delta\theta_{xz'e}$ and predicted $\Delta\theta_{xz'e}$ of Equation 5.15 of cube in clear-water scour.
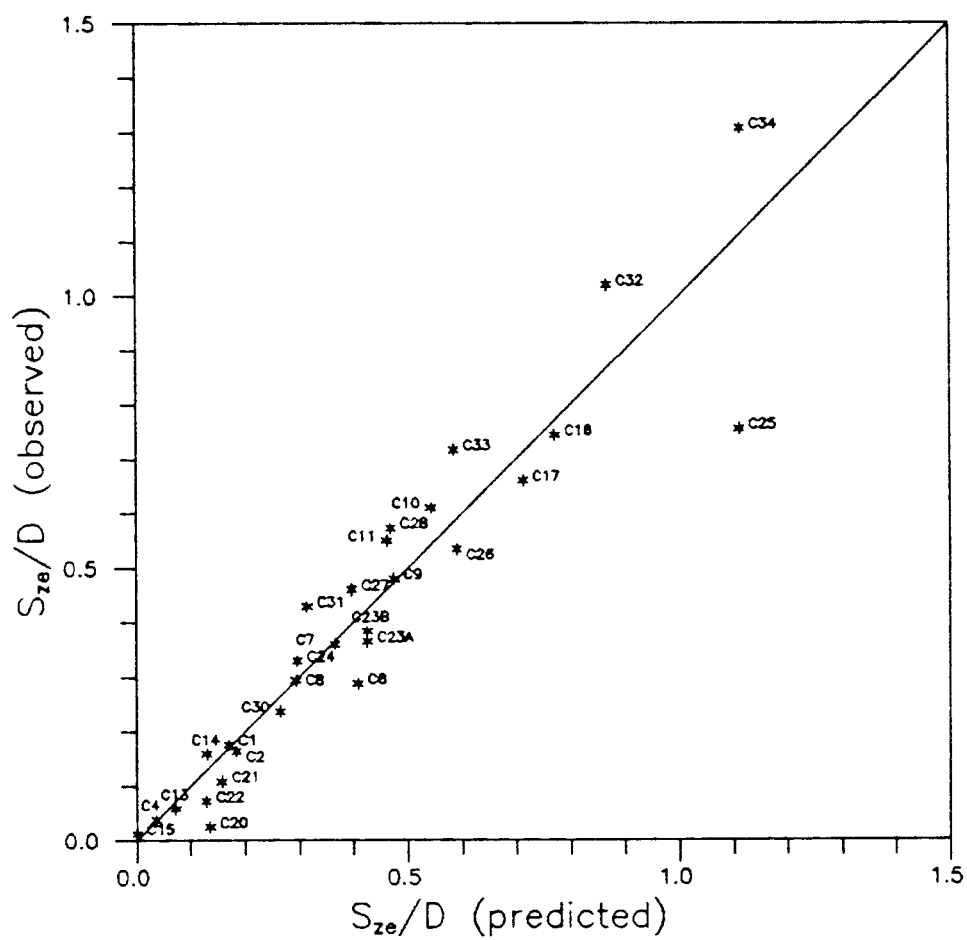
Figure 57. Comparison of observed S_{ze}/D and predicted S_{ze}/D of Equation 5.16 of cube in clear-water scour.

Figure 58 shows an example for the influence of b/D on $\Delta\theta_{xz'e}$ and S_{ze}/D at several different $D/\bar{d}$ when the F_r is kept constant at 0.20. Each constant $D/\bar{d}$ curve indicates that $\Delta\theta_{xz'e}$ is nearly constant but S_{ze}/D is increased almost linearly with b/D as long as b/D is relatively small. But the values of $\Delta\theta_{xz'e}$ and S_{ze}/D on each curve are expected to drop to zero eventually if b/D continues to increase as to become relatively large. The $\Delta\theta_{xz'e}$ vs. b/D and S_{ze}/D vs. b/D curves shift upward in Figure 58 with each incremental increase of $D/\bar{d}$ but the spacing among these curves decreases. It indicates that $\Delta\theta_{xz'e}$ and S_{ze}/D increase with $D/\bar{d}$. However, the influence of $D/\bar{d}$ becomes small when $D/\bar{d}$ continues to increase. It becomes more clear when $\Delta\theta_{xze'}$ and S_{ze}/D are directly related to $D/\bar{d}$. This is shown in Figure 59. The b/D is kept constant at b/D = 2.0 with several different F_r. The influence of $D/\bar{d}$ tends to become small when $D/\bar{d}$ is closer to the critical $D/\bar{d}$ for incipient motion of the bed material upstream of a cube. The increase of F_r from 0.2 to 0.8 tends to move the constant F_r curve closer to the origin of $D/\bar{d}$. This indicates that the critical $D/\bar{d}$ for incipient movement of a cube shifting into the scour hole and incipient motion of the bed material upstream of a cube are both decreased as F_r is increased.

Figure 60 directly shows the influence of F_r on $\Delta\theta_{xz'e}$ and S_{ze}/D at two different b/D (b/D =1.0 and 2.0) when $D/\bar{d}$ is kept constant at 16.93. Each curve in Figure 60 indicates that the increase of F_r leads to the increase of $\Delta\theta_{xz'e}$ and S_{ze}/D. The influence of F_r tends to become small when F_r is closer to the critical F_r for incipient motion of the bed material upstream of a cube.
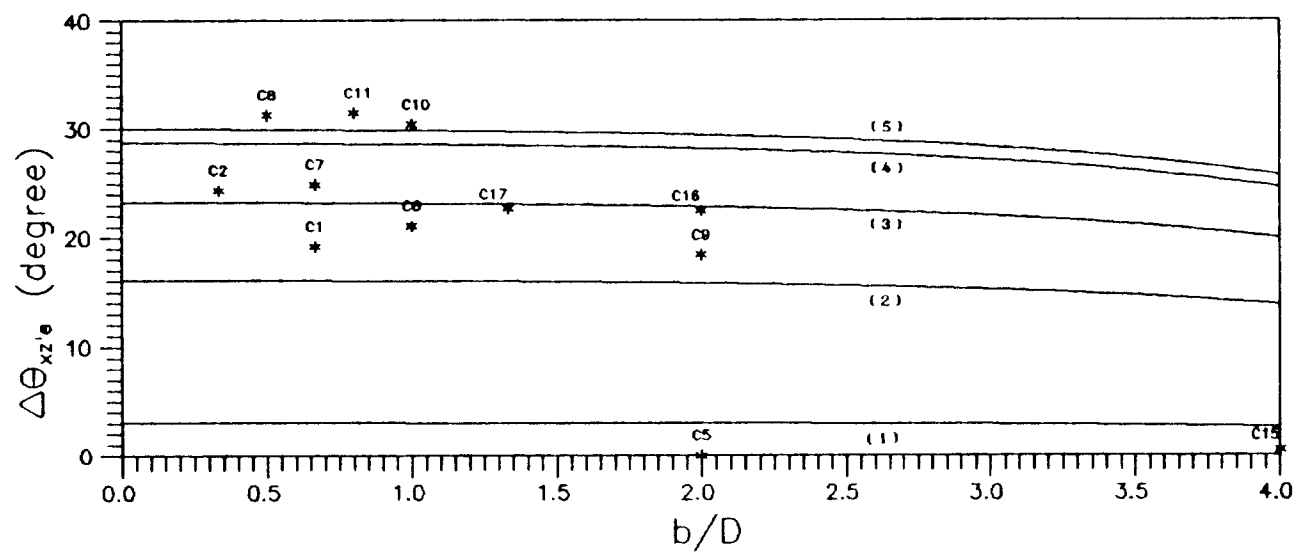
(a) $\Delta\theta_{xz'e}$ vs. b/D

Key: (1) D/d̄ = 65.13; (2) D/d̄ = 97.69; (3) D/d̄ = 130.26; (4) D/d̄ = 195.39; (5) D/d̄ = 260.52.

Figure 58. $\Delta\theta_{xz'e}$ and S_{ze}/D vs. b/D for cube in clear-water scour (F_r = 0.20).
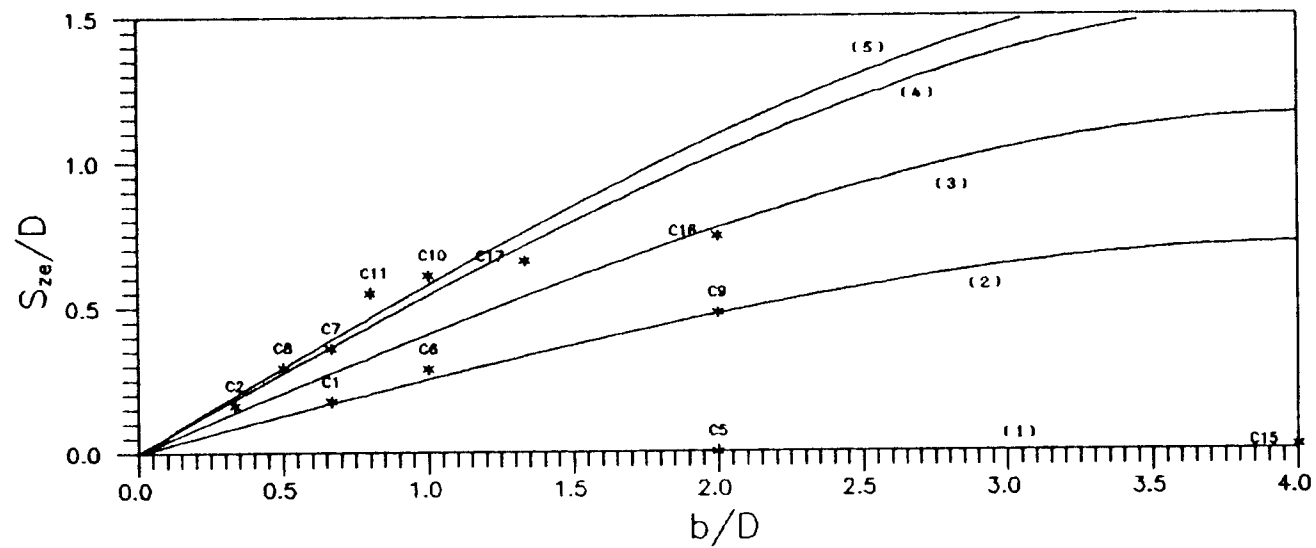
(b) S_{ze}/D vs. b/D

Figure 58. Continued.
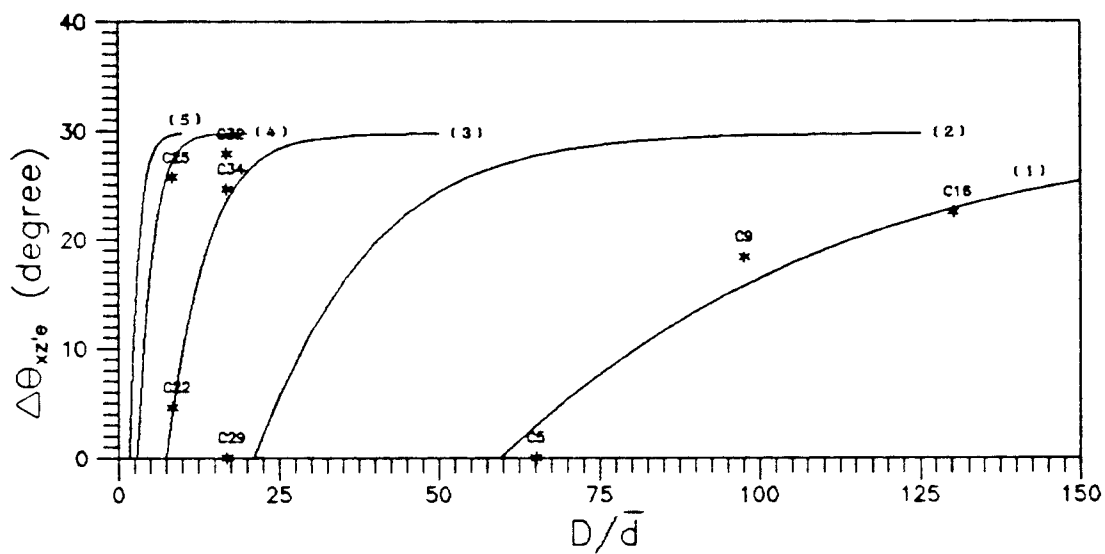
(a) $\Delta\theta_{xz'e}$ vs. $D/\bar{d}$
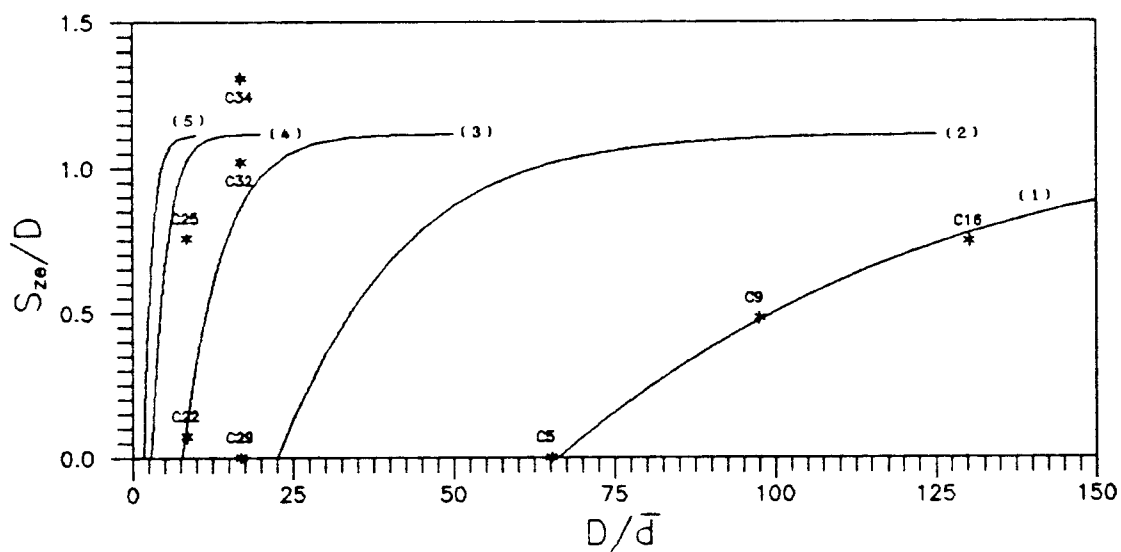
(b) S_{ze}/D vs. $D/\bar{d}$

Key: (1) $F_r = 0.20$; (2) $F_r = 0.30$; (3) $F_r = 0.45$; (4) $F_r = 0.65$;
      (5) $F_r = 0.80$.

Figure 59. $\Delta\theta_{xz'e}$ and S_{ze}/D vs. $D/\bar{d}$ for cube in clear-water scour
            ($b/D = 2.0$).
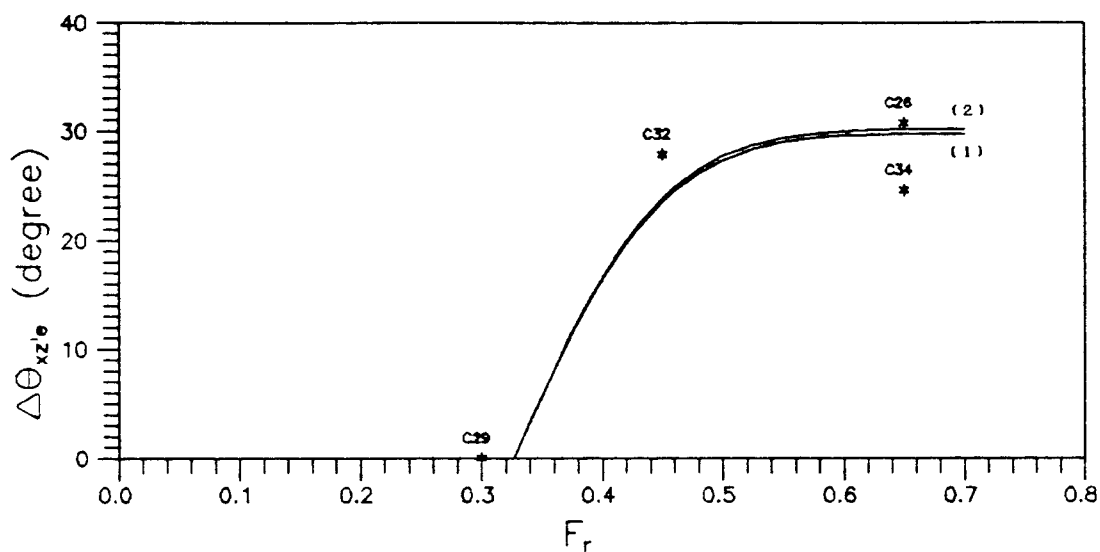
(a) $\Delta\theta_{xz'e}$ vs. F_r
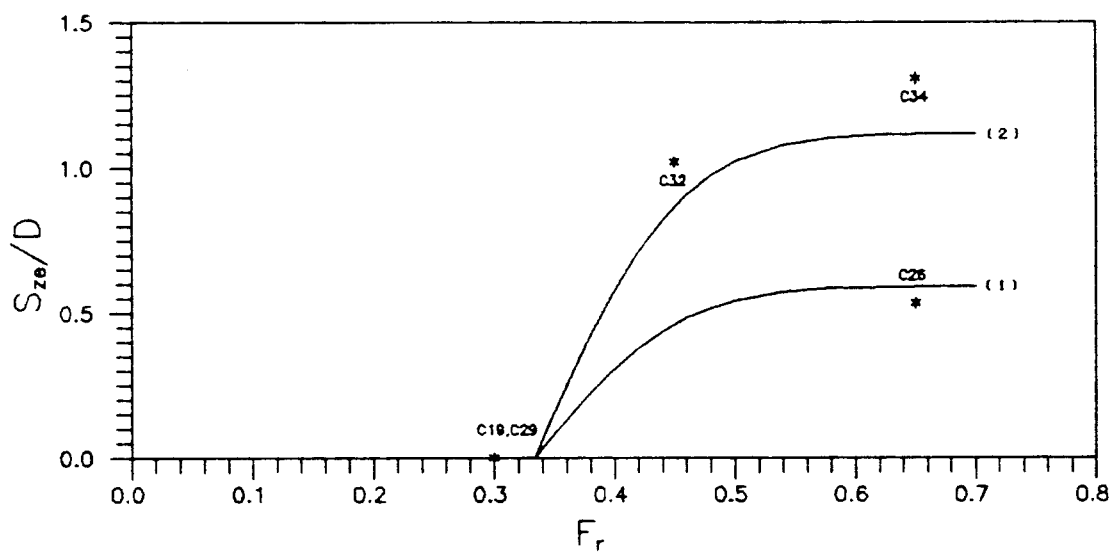
(b) S_{ze}/D vs. F_r

Key: (1) $b/D = 1.0$; (2) $b/D = 2.0$.

Figure 60. $\Delta\theta_{xz'e}$ and S_{ze}/D vs. F_r for cube in clear-water scour ($D/\overline{d} = 16.93$).

The critical condition for the incipient upstream movement of a cube in clear-water scour can be estimated when the $\Delta\Theta_{xz'e}$ and the S_{ze}/D in Equations 5.15 and 5.16 are set to zero. This gives

$$-45.0 + [75.4 \tanh(0.71 \ F_r^{2.56} \ D/\bar{d})] = 0 \qquad 5.17$$

and

$$-4.19 + [7.00 \tanh(0.76 \ F_r^{2.66} \ D/\bar{d})] = 0 \qquad 5.18$$

The explicit solution of Equations 5.17 and 5.18 in term of F_r and $D/\bar{d}$ becomes

$$F_r = 0.99 \ (D/\bar{d})^{-0.39} \qquad 5.19$$

and

$$F_r = 0.97 \ (D/\bar{d})^{-0.38} \qquad 5.20$$

respectively. The two equations are nearly the same despite the minor difference of the coefficients. An average of the coefficients in these two equations yields the formula

$$F_r = 0.98 \ (D/\bar{d})^{-0.39} \qquad 5.21$$

This can be used as the lower limit of F_r and $D/\bar{d}$ in Equations 5.15 and 5.16 when a cube starts to shift into the scour hole in clear-water scour. Neill's 1967 equation, Equation 5.6 mentioned in the previous section, again can be used as the upper limit of F_r and $D/\bar{d}$ in Equations 5.15 and 5.16 to maintain the clear-water scour at the cube. Figure 61 shows the experimental range of F_r and $D/\bar{d}$ and the two curves of Equations 5.6 and 5.21. The zone within these two curves indicates the F_r and $D/\bar{d}$ values which can cause cube movement upstream on a sand/gravel bed in clear-water scour. Substituting the critical F_r of Equation 5.6 into Equations 5.15 and 5.16 for incipient motion of the upstream bed material, Equations 5.15 and
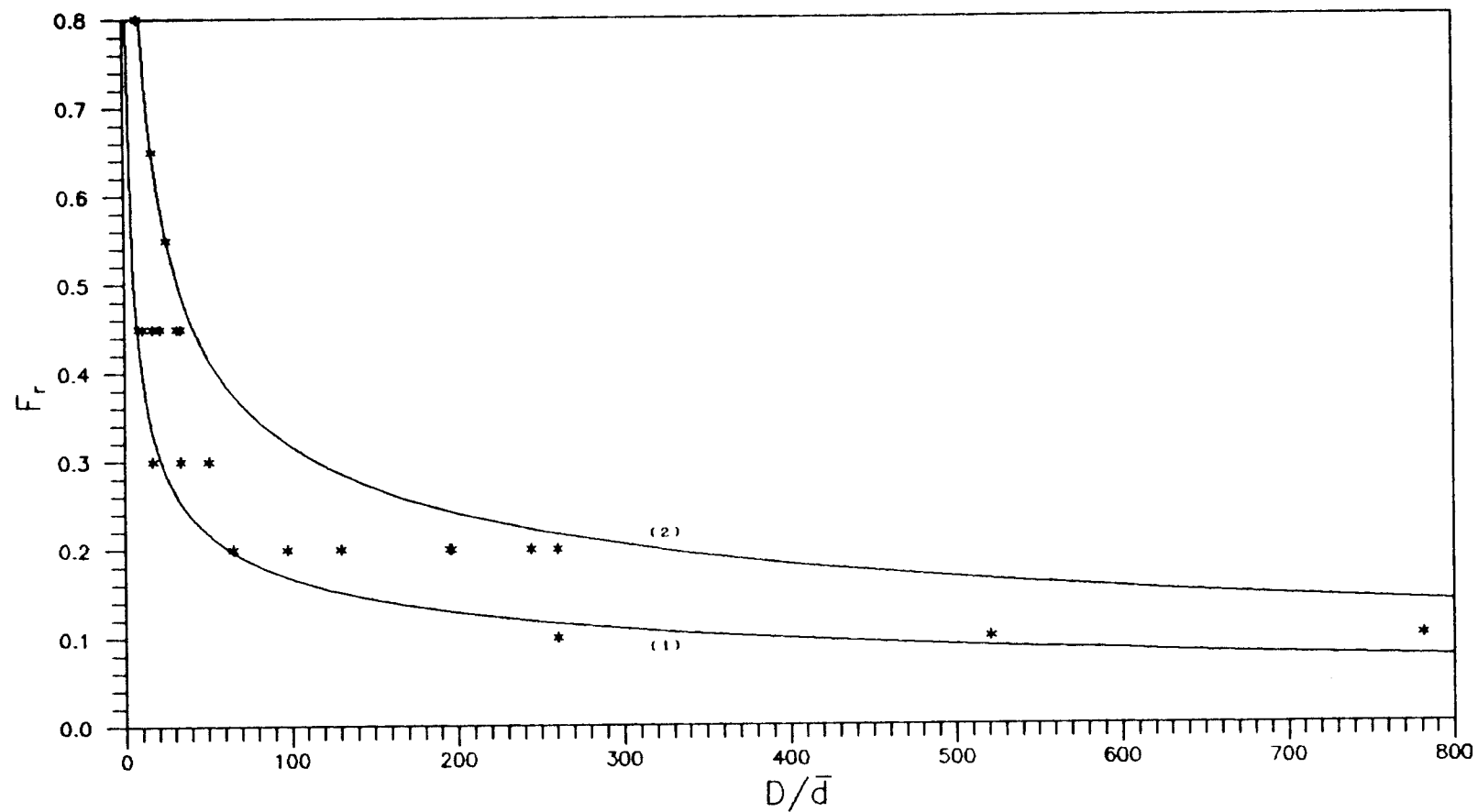
Key: (1) Equation 5.21 (Cube, present research);
(2) Equation 5.6 (Neill, 1967)

Figure 61.   The range of F_r and $D/\overline{d}$ to cause cube movement on
sand/gravel bed in clear-water scour.

5.16 become approximately

$$\Delta\theta_{xz'e} = 30.4 \{0.5 - 0.5 \tanh[0.506(b/D - 5.75)]\} \qquad 5.22$$

and

$$S_{ze}/D = 2.81\{0.5 - 0.5 \tanh[0.506(b/D - 5.75)]\} \times$$

$$[\tanh(0.215 \ b/D)] \qquad 5.23$$

respectively. Equations 5.22 and 5.23 are functions of b/D only, as

shown in Figure 62. It implies that $\Delta\theta_{xz'}$ will be approximately

equal to 30.4 degrees and S_{ze} will be approximately equal to 0.60 b

if b/D < 1.5. Hence S_{xe} will be approximately equal to 1.16 b

according to Equation 5.12. When b/D > 10, all the values are

approximately equal to zero.

Figure 63 compares the $\Delta\theta_{xz'e}$, the S_{ze}/D, and the S_{xe}/D of a cube

to those for of a circular cylinder and a sphere on a sand/gravel

bed under the same flow conditions. The obstacle sizes b are all

two inches. In Figure 63(a), 63(c) and 63(e), the upstream approach

water depths D for each obstacle on the sand bed change but the flow

Froude Number F_t remains constant at 0.20. In Figure 63(b), 63(d)

and 63(f) the bed material changes to gravel but F_t increases to

0.45. The decrease of water depth leads to increases in the

relative obstacle width b/D and the relative roughness of the bed

material $\bar{d}/D$. The curves for the cube in these figures are obtained

by Equations 5.15, 5.16 and 5.12. This indicates the combined

effect of b/D and D/$\bar{d}$. The sphere has the largest inclination among

the three obstacles because of its convenient shape to rotate. The

value can be up to almost five times larger than that of the cube or

the circular cylinder at b/D = 0.5 on a sand bed. The difference
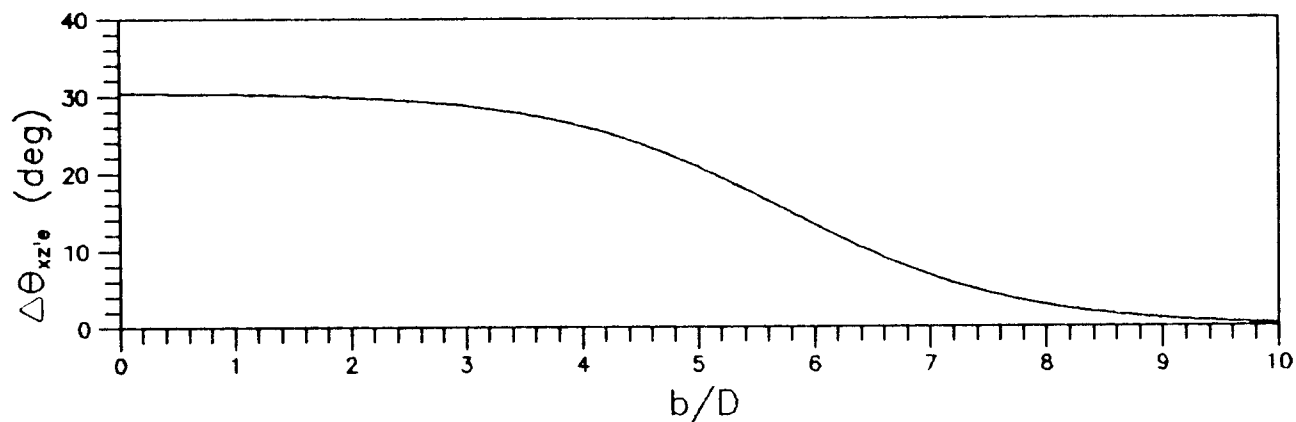
(a) $\Delta\theta_{xz'e}$ vs. b/D as given by equation 5.22
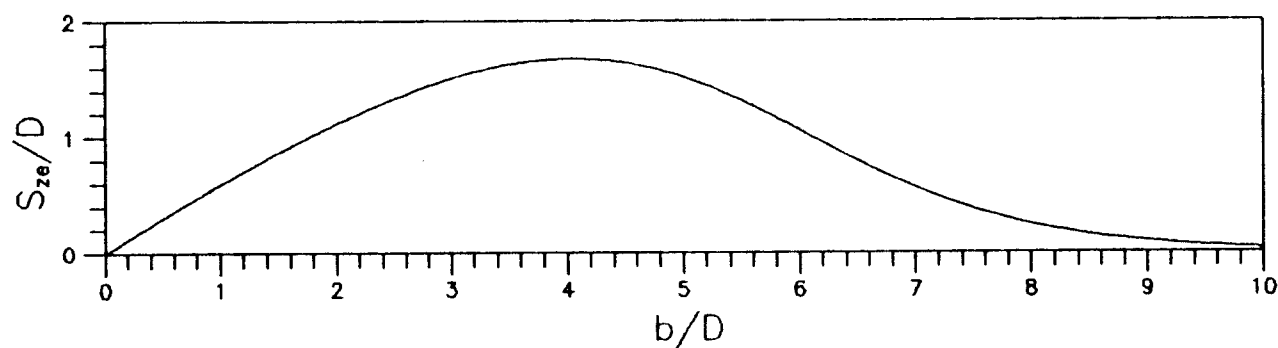
(b) S_{ze}/D vs. b/D as given by equation 5.23

Figure 62. $\Delta\theta_{xz'e}$ and S_{ze}/D vs. b/D for cube in clear-water scour
near critical conditions for incipient motion of the
upstream bed material.
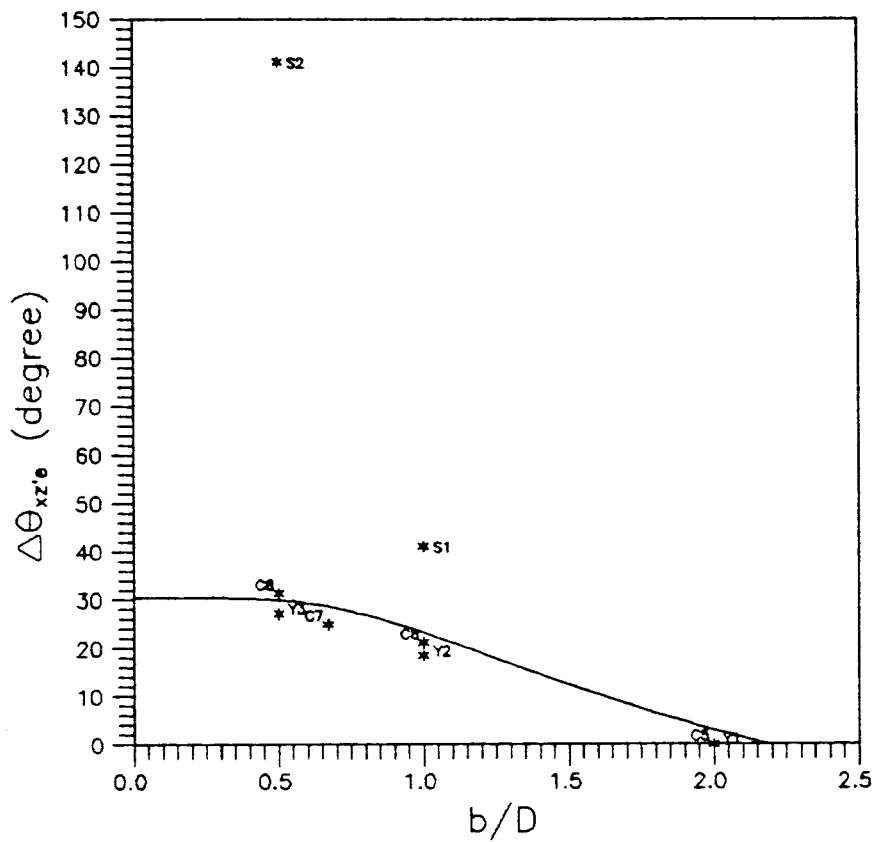
(a) $F_r = 0.20$ (sand bed)
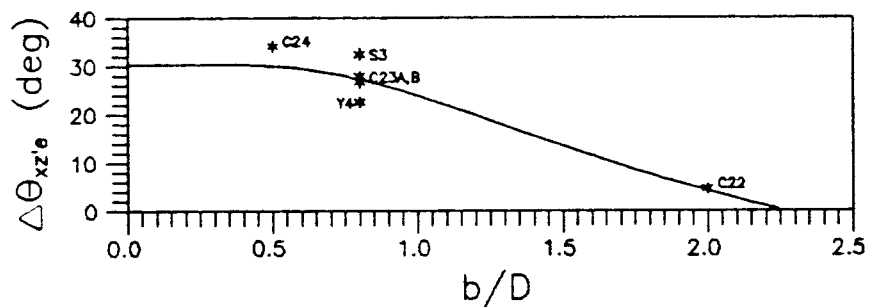
(b) $F_r = 0.45$ (gravel bed)

Figure 63.   Comparison of movement of cube, circular cylinder and sphere on sand/gravel bed in clear-water scour.
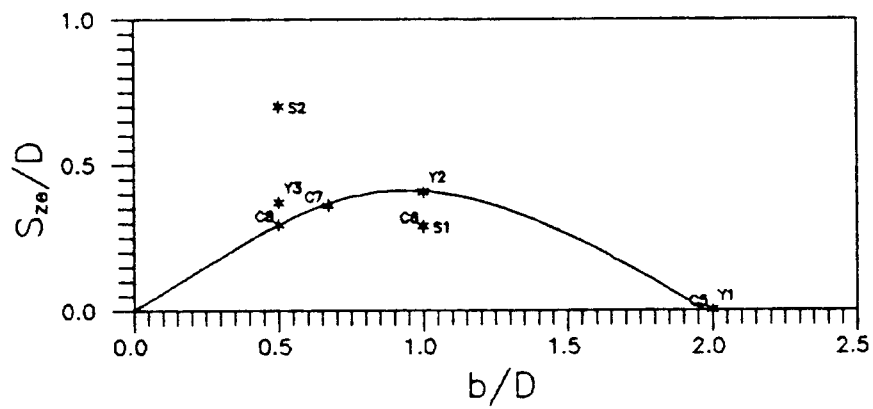
(c) $F_r = 0.20$ (sand bed)
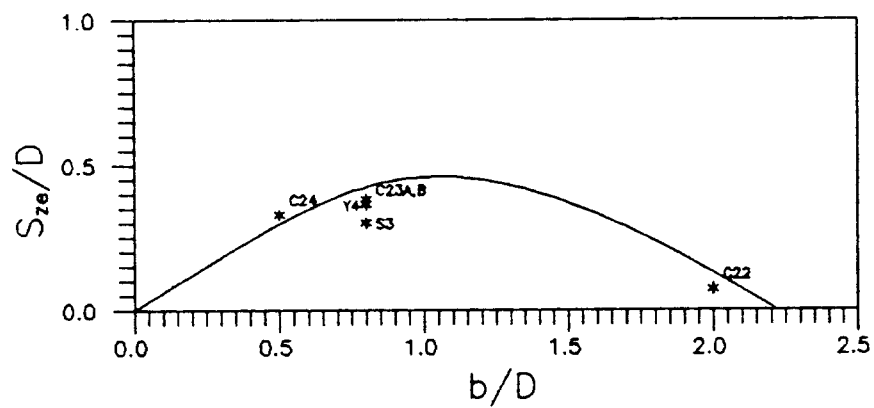
(d) $F_r = 0.45$ (gravel bed)

Figure 63. Continued.
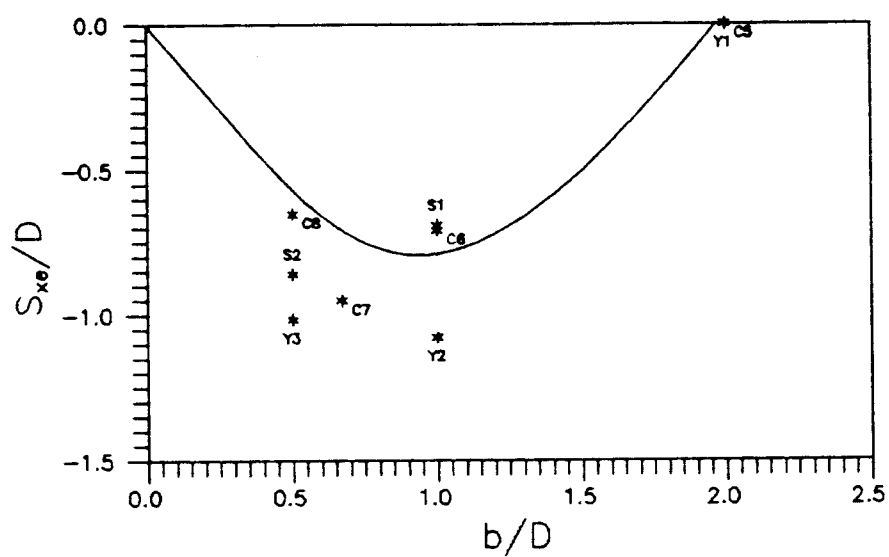
(e) $F_r = 0.20$ (sand bed)
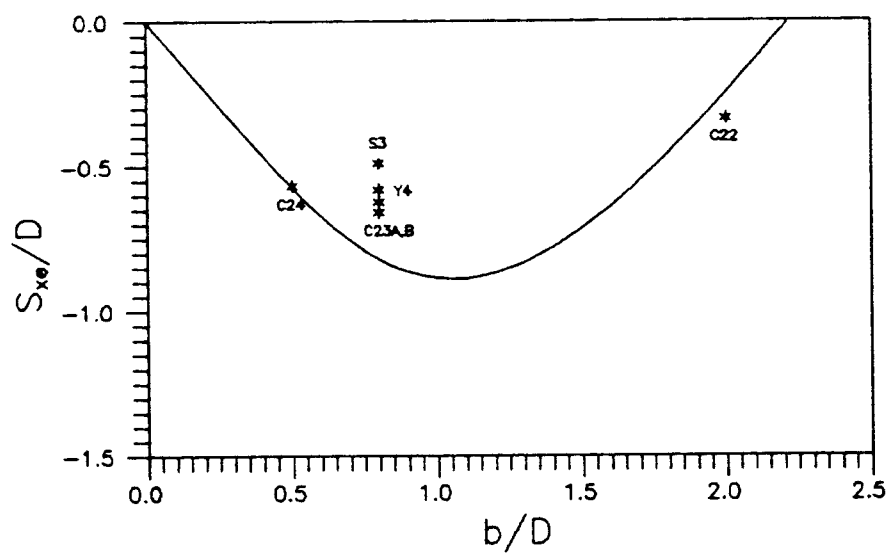
(f) $F_r = 0.45$ (gravel bed)

Figure 63. Continued.

decreases as the water depth decreases. The circular cylinder has nearly the same degrees of inclination as the cube but seems to slide more easily into the scour hole on a sand bed.

VI. SUMMARY AND CONCLUSIONS

Summary and Conclusions of Research

Local scour at isolated obstacles on river beds has been studied experimentally in this research. The main purpose of this study was to develop a predictive knowledge about the maximum equilibrium scour depths, equilibrium scour volumes, and induced equilibrium movements at isolated cubes on river beds in clear-water scour.

This research was achieved by a systematic flume study based on the results of dimensional analysis of local scour. Experiments were performed in a straight flume 8.23 m long with a rectangular cross section 46 cm wide and 61 cm deep. The main tested obstacles for local scour were cubes 2.54 cm, 5.08 cm, 7.62 cm and 10.16 cm wide. Local scour at a circular cylinder of aspect ratio 1 and a sphere (5.08 cm wide) were also examined for comparison with scour at cubes. The specific gravity of each obstacle was 2.79. Each obstacle was placed on a flat movable bed and oriented normal to the incident water flow. The two tested sediments were non-cohesive medium sand and very fine gravel. Each was nearly uniform in size, with mean sizes of 0.39 mm and 3.0 mm, respectively. Both sediments had specific gravities of 2.60. The tested flow conditions were controlled to give many combinations of the relevant dimensionless parameters for local scour: the flow Froude Number F_r, relative obstacle size b/D, and relative roughness of bed material $\bar{d}/D$. The

F_r values ranged from 0.1 to 0.8. The b/D values ranged from 0.25
to 4. The $\bar{d}$/D values ranged from 0.0013 to 0.1181.

The local scouring processes and equilibrium scour patterns at
isolated obstacles on movable beds were examined in movable-bed
experiments. Prior to the movable-bed experiments, the mean flow
fields around a 7.62 cm cube on a fixed bed were examined at
F_r = 0.20 and 0.45 with several relative water depths D/b. The mean
flow fields around a circular cylinder of aspect ratio 1 and a
sphere (each 7.62 cm wide) on a fixed bed were also examined at
F_r = 0.45 and D/b = 1.25 for comparison with the flow field at a
cube . Water surface profiles and longitudinal velocity profiles
along the plane of symmetry, as well as the horizontal velocities at
a vertical distance -z = 0.1 b near the bed, were measured around
these obstacles for the fixed-bed experiments.

The main conclusions drawn from this study can be summarized as
follows:

1. Longitudinal velocity profiles along the plane of symmetry
of an isolated obstacle on a fixed-bed:

For a slightly submerged cube (D/b = 1.25), the path of maximum
velocity downstream of the cube moves from the water surface into
the lower part of the flow by the time it reaches x/b = 4.0. At a
greater distance downstream, the path of maximum velocity tends to
move upward toward the water surface. An increase of flow Froude
Number F_r from 0.20 to 0.45 leads to a small hydraulic jump at x = 1 b
behind a cube. The relative longitudinal velocity $(u/\bar{U})$ near bed is
increased in this region. The hydraulic jump from flow past a

sphere is located closer to the obstacle than those for flow past a circular cylinder and a cube.

2. Distributions of horizontal velocity near the bed around an isolated obstacle on a fixed bed:

The decrease of relative water depth (D/b) at a constant Froude Number F_t leads to increased average relative horizontal velocity (V/u) for those points that have locally increased velocity near a cube. The increase of flow Froude Number (F_t) at a constant relative water depth also leads to increased average relative horizontal velocity (V/u) near a cube. The cube has the highest average V/u value, as compared to flow near a circular cylinder or a sphere.

3. Local scour process at an isolated cube on a movable bed:

Local scour starts at the upstream corners of a cube. The resulting two local disturbances of the movable bed grow radially. They rapidly merge at the plane of symmetry in front of the cube and undercut the bed material beneath the cube. The scoured bed material soon deposits around the two rear corners of the cube. These deposits rapidly merge at the plane of symmetry behind the cube and continue to grow. The cube overhangs the upstream scour hole until its stability is undermined. It then rotates forward and slides into the upstream scour hole. The horseshoe vortex in front of the cube gradually deepens and enlarges the scour hole. This leads to continuing movement of the cube in the scour hole. As local scour continues, the two mounds of deposits behind the cube on both sides are pushed away, allowing formation of a downstream scour

hole. In clear-water scour, without the general movement of the bed material upstream of the cube, the scouring will continue until equilibrium is reached. At this time, a scour hole has formed around the cube, the maximum scour depth has been attained, and the cube movement has stopped. In contrast, when there is general movement of bed material upstream of the cube after the development of the scour hole, the scour hole can be filled in by this upstream sediment supply, which can lead to partial burial of the cube. When the sediment supply later decreases, the scour hole can redevelop and the cube can be reexposed.

4. Bed scour depth and scour volume:

There is not a unique equilibrium scour pattern for clear-water scour at a cube on a movable bed. Replicate runs (23A and 23B) did produce nearly identical patterns. However, when test variables changed (as for all other runs), the interaction of the relative obstacle size b/D, the flow Froude Number F_r, and the relative roughness of bed material $\overline{d}/D$ upon local scour led to several different equilibrium scour patterns. The maximum equilibrium scour depth and scour volume at a cube are highly dependent upon these parameters.

A nonlinear regression of the experimental data yields the following equation for the prediction of maximum equilibrium scour depth at a cube in clear-water scour:

$$d_{se}/D = \{-1.30 + [4.75 \tanh(0.47 \, F_r^{2.56} \, D/\overline{d})]\} \, [\tanh(0.215 \, b/D)]$$

$$6.1$$

The upper limit of F_r and $D/\overline{d}$ which maintain clear-water scour at a

cube on sand/gravel bed in Equation 6.1 can be estimated by the
following equation:

$$F_r = 2.00 \ (D/\bar{d})^{-0.40} \qquad\qquad 6.2$$

The critical condition for the incipient motion of the bed material
at a cube in clear-water scour is:

$$F_r = 0.82 \ (D/\bar{d})^{-0.39} \qquad\qquad 6.3$$

As the water becomes relatively deep, the shape effect of the
circular cylinder and the sphere become negligible.

The equilibrium scour volume at a cube in clear-water scour can
be estimated by the following equation:

$$V_{se}^{\frac{1}{3}}/D = 2.10 \ d_{se}/D \qquad\qquad 6.4$$

5. <u>Obstacle displacement and inclination due to scour</u>:

The major relative equilibrium movement of a cube on a movable
bed due to scour involves the relative equilibrium longitudinal
displacement S_{xe}/D, relative equilibrium vertical settlement S_{ze}/D,
and longitudinal inclination $\Delta\theta_{xz'e}$.

The nonlinear regressions of the experimental data yield the
following equations for the predictions of $\Delta\theta_{xz'e}$ and S_{ze}/D:

$$\Delta\theta_{xz'e} = \{-45.0 + [75.4 \ \tanh(0.71 \ F_r^{2.56} \ D/\bar{d})]\} \ \times$$
$$\{0.5 - 0.5 \ \tanh[0.506(b/D - 5.75)]\} \qquad 6.5$$

$$S_{ze}/D = \{-4.19 + [7.00 \ \tanh(0.76 \ F_r^{2.66} \ D/\bar{d})]\} \ \times$$
$$\{0.5 - 0.5 \ \tanh[0.506(b/D - 5.75)]\} \ [\tanh(0.215 \ b/D)] \qquad 6.6$$

The critical condition for the incipient upstream movement of a cube
in clear-water scour is:

$$F_r = 0.98 \ (D/\bar{d})^{-0.39} \qquad\qquad 6.7$$

The relative equilibrium longitudinal displacement S_{xe}/D can be

estimated by the following equation:

$$S_{xe}/D = 1.93 \, S_{ze}/D \qquad\qquad 5.12$$

The longitudinal inclination of a sphere can be up to almost five times larger than that of a cube or a circular cylinder on a sand bed at $b/D = 0.5$ and $F_r = 0.20$. The difference decreases as the water depth decreases.

Application of Research

Study of local scour at isolated obstacles on river beds has the immediate application in fish habitat rehabilitation and enhancement. It provides important information for estimating the maximum scour depth and scour volume, both of which are needed for such application. Information about incipient motion of an isolated obstacle due to scour derived from the study can provide guidance for designing stable instream structures in engineering applications. Finally, information about the movement of an isolated obstacle due to scour can contribute to a better general understanding of the local scour problems. This can be lead to possible future applications.

Recommendations for Future Research

1. Laser doppler anemometry without disturbing the flow, or hot film anemometry having a smaller velocity probe, is recommended for obtaining detailed velocity and turbulence measurements near the

bed in the horseshoe vortex and near-wake zone at an obstacle.

2. Tests with large relative cube size ($b/D > 10$) are suggested for future research to confirm the inferences of this study that this relative cube size will be too large to affect the relative maximum equilibrium scour depth d_{se}/D and a cube will keep stationary during clear-water scour.

3. Larger models and prototype tests are suggested for future research to compare and to verify the results of this study.

4. Future research can extend the results of this study to other obstacle shapes and to consider the effects of the bed material size distribution, as well as to consider local scour during general sediment transport.

5. Numerical modeling is recommended for future research. The results of this study can be used to tune up and to verify the model. Existing model to compute flow field can be coupled with sediment transport relation to attempt to describe local scour at isolated obstacles.

VII. REFERENCES

Adamek, J. C., "Lift and Drag Forces on a Cube on a Boundary in a Finite, Three-Dimensional Flow Field with Free-Surface Effects," PhD Thesis, Utah State University, 1968.

Baker, C. J., "The Laminar Horseshoe Vortex," Journal of Fluid Mechanics, Vol. 95, Part 2, 1979.

Baker, C. J., "Theoretical Approach to Prediction of Local Scour Around Bridge Piers," Journal of Hydraulic Research, Vol. 18, No. 1, 1980.

Baker, C. J., "New Design Equations for Scour Around Bridge Piers," Journal of Hydraulic Division, ASCE, Vol. 107, No. HY11, November 1981.

Breusers, H. N .C., Nicollet, G., and Shen, H. W., "Local Scour Around Cylindrical Piers," Journal of Hydraulic Research, Vol. 15, No. 3, 1977.

Castro, I. P., and Robins A. G., "The Flow Around a Surface-Mounted Cube in Uniform and Turbulent Streams," Journal of Fluid Mechanics, Vol. 79, Part 2, 1977.

Chiew, Y. M., and Melville B. W., "Local Scour Around Bridge Piers," Journal of Hydraulic Research, Vol. 25, No.1, 1987.

Clark, A., Novak, P., and Russell K., "Modeling of Local Scour With Particular Reference to Offshore Structures," International Conference on the Hydraulic Modeling of Civil Engineering Structures, Coventry, England, September 22-24,1982.

Eckerle, W. A., and Langston L. S., "Horseshoe Vortex Formation Around a Cylinder," Transactions of the ASME, Vol. 109, April 1987.

Eckman, J. E., and Nowell, A. R. M., "Boundary Skin Friction and Sediment Transport About an Animal-Tube Mimic," Sedimentology, 31, 1984.

Fisher, A. C., "Characteristics of Local Scour Induced by an Individual Fish Rock," M.S. project report, Oregon State University, 1984.

Fisher, A. C. and Klingeman, P. C., "Local Scour at Fish Rocks," Water for Resource Development, Conference Proceedings, ASCE, Coeur d'Alene, Idaho, August 1984.

Gowda, B. H. L., Gerhardt, H. J., and Kramer, C., "Surface Flow Field Around Three-Dimensional Bluff Bodies," Journal of Wind Engineering and Industrial Aerodynamics, Vol. 11, 1983.

Graf, W. H., "Hydraulics of Sediment Transport," McGraw-Hill Book Company, 1971.

Jain S. C., and Fischer E. E., "Scour Around Bridge Piers at High Flow Velocities," Journal of Hydraulic Division, ASCE, Vol. 106, No. HY11, November 1980.

Kaplan W., "Advanced Mathematics for Engineers," Addison-Wesley Publishing Company, 1981.

Klingeman, P. C., "Evaluating Hydrologic Needs for Design of Stream Habitat Modification Structures," Pacific Northwest Stream Habitat Management Workshop, Humboldt Chapter, American Fisheries Society, Arcata, California, Oct. 10 - 12, 1984.

Laursen, E. M., "Observations on the Nature of Scour," Proc. of 5th Hydraulic Conference, Bulletin 34, University of Iowa, Iowa City, Iowa, 1952.

Melville, B. W., and Raudkivi, A. J., "Flow Characteristics in Local Scour at Bridge Piers," Journal of Hydraulic Research, Vol. 15, No. 4 , 1977.

Okamoto, S., "Turbulent Shear Flow Behind a Sphere Placed on a Plane Boundary," in: Turbulent shear flow 2, ed. by L. J. S. Bradbury, F. Durst, B. E. Launder, F. W. Schmidt, J. H. Whitelaw (Springer-Verlag Berlin Heidelberg New York 1980).

Okamoto, S., "Experimental Investigation of Flow Past Bluff Body of Square Section Placed On Ground Plane," Bulletin of JSME, Vol. 28, No. 239, May 1985.

Peterka, J. A., Meroney, R. N., and Kothari, K. M., "Wind Flow Patterns about Buildings," Journal of Wind Engineering and Industrial Aerodynamics, Vol. 21, 1985.

Qadar, A., "Vortex Scour Mechanism at Bridge Piers," Proc. Instn. Civ. Engrs., 1981, Part 2.

Raudkivi, A.J. and Ettema, R., "Stability of Armour Layers in Rivers," Journal of Hydraulic Division, ASCE, Vol. 108, No. HY9, September 1982.

Thomas Z., "Settlement of a Cylindrical Body Placed on the Surface of an Alluvial River Bottom," Proceeding 14 IAHR Congress, Paris, 3, 1971a.

Thomas, Z., "Time Development of the Deformation of an Alluvial Bottom," Proceeding 14 IAHR Congress, Paris, 3, 1971b.

Wang, S. S.-Y., "Computer Simulation of Sedimentation Processes," Finite Elements in Water Resources, Proceedings of the 4th International Conference, Hannover, Germany, June 1982.

Wang, S. S.-Y., "Development of a Sediment Transport Model for Field Application," Technical Interim Report G1234-06, Water Resources Research Institute, Mississippi State University, July 1987.

APPENDICES

APPENDIX A: LIST OF SYMBOLS

B = channel width;

b = obstacle width;

c = cohesiveness of the bed material;

D = water depth;

D_x = water depth along the plane of symmetry;

$\bar{d}$ = mean size of the bed material;

d_1 = exposed single particle size;

d_2 = particle size of sediment beneath a single d_1 particle;

d_s = local scour depth at the obstacle;

d_{se} = d_s value after scour has reached equilibrium;

F_r = $\bar{U}/\sqrt{gD}$ = Froude Number of the flow;

$F_{\bar{d}}$ = $\bar{U}/\sqrt{\gamma'_{sb}\bar{d}/\rho}$ = Shields parameter of the bed material;

F_b = $\bar{U}/\sqrt{\gamma'_{so}b/\rho}$ = Shields parameter of the obstacle;

g = gravitational acceleration;

h = obstacle height;

K_D = flow depth adjustment factor;

K_d = sediment size adjustment factor;

L = obstacle length;

Nc = geometric shape of the channel;

P = protrusion of a particle into the flow;

Q = flow discharge;

R = radial distance from obstacle center;

r = initial radius of the horseshoe vortex;

Re = $\bar{U}D/\nu$ = Reynolds Number in terms of water depth D;

Re_b = $\overline{U}b/\nu$ = Reynolds Number in terms of obstacle width b;

Re_p = $\overline{U}_* d_1/\nu$ = Reynolds Number in terms of particle size d_1;

S = sediment supply in a channel;

s = channel slope;

S_1 = distance from the upwind side of the obstacle to the primary separation point of the horseshoe vortex;

S_2 = distance from the upwind side of the obstacle to the secondary separation point of the horseshoe vortex;

S_3 = maximum width between the two primary separation points on each side of the obstacle;

S_4 = near-wake length between the rear face and the downwind reattachment point of the obstacle;

S_i = displacement at the center of the obstacle top surface in i direction, i = x, y, and z;

S_{ie} = S_i value after scour has reached equilibrium;

S_g = the specific gravity of the particle;

t = time;

U = freestream velocity of the flow in x direction;

$\overline{U}$ = average velocity of the flow;
    = approach mean velocity of the flow in x direction;

$\overline{U}_c$ = critical mean approach flow velocity for the incipient motion of the bed material;

U_r = approach mean velocity of the flow at z = 10 h in x direction;

u = longitudinal component of velocity;

u′ = velocity fluctuation of the flow in x direction;

u_* = shear velocity of the flow;

u_{*1} = critical shear velocity for the incipient motion of a surface of d_1 particle;

u_{*i} = critical shear velocity for the incipient motion of a single exposed d_1 particle on the bed of d_2 particles;

V = horizontal velocity at $-z = 0.1\ b$ from the bed;

V_s = local scour volume at the obstacle;

V_{se} = V_s value after scour has reached equilibrium;

w = vertical component of velocity;

x = coordinate axis with the origin at the center of the bottom face of the obstacle; x is taken in the direction of the flow;

y = coordinate axis with the origin at the center of the bottom face of the obstacle; y is taken horizontally rightward to the direction of the flow;

z = coordinate axis with the origin at the center of the bottom face of the obstacle; z is taken vertically downward to the direction of the flow;

x' = movable reference axis with the origin at the center of the top surface of the obstacle; x is taken in the direction of the normal vector of the rear face of the obstacle;

y' = movable reference axis with the origin at the center of the top surface of the obstacle; y is taken in the direction of the normal vector of the right face of the obstacle;

z' = movable reference axis with the origin at the center of the top surface of the obstacle; z' is taken in the direction of the normal vector of the top face of the obstacle;

β = obstacle shape;

γ = specific weight of the fluid;

γ'_{sb} = submerged specific weight of the bed material;

γ'_{so} = submerged specific weight of the obstacle;

θ = angle of attack of the flow against the obstacle;

θ_{ci} = $u_{*i}^2/g(S_s-1)d_i$ = critical dimensionless shear stress for the exposed d_i particle;

θ_{cl} = critical dimensionless shear stress for a surface of d_i particles;

θ_{c2} = critical dimensionless shear stress for a surface of d_2 particles;

θ_{ij} = angle from axis i to axis j at the obstacle top surface, i = x, y and z at time t =o, j = x', z' at time t;

δ = boundary layer height or thickness;

$\Delta\theta_{ij}$ = inclination of the unit tangent vector and unit normal vector at the obstacle top surface, equals to the difference of θ_{ij} at time t and at time zero;

$\Delta\theta_{ije}$ = $\Delta\theta_{ij}$ value after scour has reached equilibrium;

ν = kinematic viscosity of the fluid;

ρ = density of the fluid;

σ = standard deviation of the grain size distribution of the bed material;

$\bar{\tau}_c$ = critical shear stress of the bed;

$\bar{\tau}_i$ = imposed shear stress of the approach flow;

$\sqrt{\overline{\tau_i^2}}$ = imposed turbulent shear stress of the approach flow;

$\bar{\tau}$ = mean skin friction; and

$\sqrt{\overline{\tau^2}}$ = turbulent skin friction.

APPENDIX B:

VELOCITY DATA FOR FIXED-BED EXPERIMENTS
WITH CUBE, CIRCULAR CYLINDER AND SPHERE

Tables B-1 through B-4: Longitudinal Velocities in Plane of Symmetry

Tables B-5 through B-11: Horizontal Velocities around Obstacles at
Plane of -z/b = 0.1

Table B-1. Longitudinal velocities on plane of symmetry of cube during fixed-bed runs CU1 and CU2.

Run No.	CU1						CU2					
$-z/b$	0.10	0.50	0.90	1.10	1.30	1.70	0.10	0.31	0.56	0.81	1.06	1.11
x/b	$u/\bar{U}$	$u/\bar{U}$	$u/\bar{U}$	$u/\bar{U}$	$u/\bar{U}$	$u/\bar{U}$	$u/\bar{U}$	$u/\bar{U}$	$u/\bar{U}$	$u/\bar{U}$	$u/\bar{U}$	$u/\bar{U}$
-8.00	0.73	0.87	0.96		0.99	0.99	0.73	0.88	0.99	0.99	1.04	
-4.00	0.73	0.87	0.96		0.99	1.02	0.81	0.92	0.95	1.04	1.04	
-2.50	0.73	0.87	0.96		0.99	1.02	0.77	0.84	0.95	0.99	1.04	
-2.00	0.67	0.82	0.93		0.99	1.02	0.77	0.88	0.95	0.95	1.04	
-1.50	0.49	0.75	0.87		0.93	1.02	0.57	0.77	0.88	0.92	0.99	
-1.00	0.17	0.49	0.58		0.93	1.05	0.16	0.54	0.61	0.72	0.88	
-0.67	-0.05	0.17	0.44		1.05	1.07	0.00	0.19	0.19	0.38	0.88	
-0.50				0.87	1.07	1.11						1.45
0.00				0.29	1.34	1.19						1.56
0.50				0.44	1.23	1.31						1.22
0.67	-0.09	-0.15	-0.05		1.02	1.28	-0.04	-0.04	-0.04	-0.07	0.95	
1.00	-0.24	-0.17	0.24		0.99	1.25	-0.19	-0.15	-0.19	-0.04	0.88	
1.50	-0.09	-0.05	0.26		0.99	1.14	-0.16	-0.19	-0.15	-0.19	0.61	
2.00	0.09	0.17	0.44		0.93	1.11	0.00	0.11	0.04	0.04	0.38	
2.50	0.17	0.35	0.58		0.93	1.11	0.16	0.23	0.23	0.19	0.34	
4.00	0.44	0.58	0.73		0.96	1.05	0.46	0.57	0.57	0.46	0.42	
6.00	0.64	0.75	0.87		0.99	1.05	0.61	0.72	0.77	0.69	0.69	
8.00	0.70	0.82	0.87		0.99	1.05	0.69	0.77	0.84	0.84	0.77	
12.00	0.73	0.87	0.96		1.02	1.05	0.77	0.90	0.88	0.88	0.88	
16.00	0.73	0.87	0.99		1.02	1.05	0.77	0.88	0.88	0.92	0.92	

Table B-2. Longitudinal velocities on plane of symmetry of cube during fixed-bed runs CU3 and CU4.

Run No.	CU3			CU4						
-z/b	0.10	0.22	0.42	0.10	0.31	0.56	0.81	1.00	1.06	1.11
x/b	u/Ū	u/Ū	u/Ū	u/Ū	u/Ū	u/Ū	u/Ū	u/Ū	u/Ū	u/Ū
-8.00	0.88	1.08	1.08							
-4.00	1.02	1.08	1.08	0.92		1.07			1.07	
-2.50	0.95	1.08	1.08	0.92		1.07			1.07	
-2.00	0.81	1.01	1.01							
-1.50	0.67	0.88	0.88	0.61	0.84	0.92	0.99		0.99	
-1.00	0.27	0.48	0.54	0.28	0.52	0.57	0.67		0.76	
-0.67	0.00	0.20	0.20	0.00	0.20	0.20	0.30		0.66	
-0.50										1.15
0.00										1.22
0.50										
0.67	0.00	0.00	0.00	-0.26	-0.26	-0.14	0.06	1.30		
1.00	0.00	-0.07	-0.14	-0.34	0.30	-0.03	0.69	-0.18		
1.50	-0.20	-0.20	-0.20	0.31	0.35	0.17	0.17	-0.15		
2.00	0.00	0.00	-0.20	0.54						
2.50	0.00	0.20	0.27	0.55	0.55	0.38	0.00		-0.18	
4.00	0.27	0.54	0.61	0.49	0.52	0.43	0.31		0.21	
6.00	0.54	0.67	0.81	0.61	0.69	0.69	0.61		0.46	
8.00	0.61	0.74	0.95	0.69	0.76	0.76	0.76		0.69	
12.00	0.81	0.88	1.01							
16.00	0.81	0.95	1.01	0.93		0.99			0.92	

Table B-3. Longitudinal velocities on plane of symmetry of cube during fixed-bed run CU5.

Run No.	CU5				
-z/b	0.10	0.22	0.32	0.40	0.42
x/b	$u/\bar{U}$	$u/\bar{U}$	$u/\bar{U}$	$u/\bar{U}$	$u/\bar{U}$
-8.00					
-4.00	1.02	1.10			1.05
-2.50	0.97	1.07			1.02
-2.00					
-1.50	0.71	0.87			0.87
-1.00	0.31	0.58			0.58
-0.67	-0.15	0.18			0.23
-0.50					
0.00					
0.50					
0.67	-0.08	0.00	0.00		
1.00	-0.18	0.08	-0.02		
1.50	-0.31	-0.15	0.00		
2.00			0.08		
2.50	-0.26	0.00	0.39		
4.00	0.23	0.39	0.61		
6.00	0.56	0.61		0.61	
8.00	0.66	0.69			
12.00					
16.00	0.87	0.94			0.84

Table B-4. Longitudinal velocities on plane of symmetry of circular cylinder and sphere during fixed-bed runs CY and SP.

Run No.	CY							SP							
-x/b	0.10	0.31	0.56	0.81	1.00	1.06	1.11	0.10	0.31	0.56	0.81	0.90	1.00	1.06	1.14
x/b	$u/\bar{U}$	$u/\bar{U}$	$u/\bar{U}$	$u/\bar{U}$	$u/\bar{U}$	$u/\bar{U}$	$u/\bar{U}$	$u/\bar{U}$	$u/\bar{U}$	$u/\bar{U}$	$u/\bar{U}$	$u/\bar{U}$	$u/\bar{U}$	$u/\bar{U}$	$u/\bar{U}$
-8.00								0.85							
-4.00	0.97	1.07	1.07	1.15		1.10		0.92	1.00	1.08	1.08			1.08	
-2.50	0.92	1.07	1.11	1.11		1.10		0.92	1.00	1.08	1.08			1.08	
-2.00								0.92	1.00	1.08	1.08			1.08	
-1.50	0.79	0.95	1.02	1.07		1.03		0.85	0.97	1.00	1.06			1.05	
-1.00	0.53	0.77	0.84	0.84		0.92		0.69	0.80	0.85	0.92			0.95	
-0.67	0.23	0.36	0.36	0.45		0.77		0.49	0.52	0.46	0.62			0.82	
-0.50							1.00	0.48				0.71		0.88	
0.00							1.15								1.23
0.50								-0.15				0.85			
0.67	-0.30	-0.16	-0.16	0.00	1.30			-0.12	0.17	0.62	0.46	-0.17			
1.00	-0.25	0.00	0.16	0.69	-0.03			0.31	0.77	0.92	-0.26	-0.42			
1.50	0.30	0.33	0.39					0.85	0.95	0.62	0.00		-0.31		
2.00								0.95	1.00	0.89	0.31		0.00		
2.50	0.69	0.52	0.36	0.16				0.92	1.00	0.92	0.54			0.18	
4.00	0.77	0.69	0.55	0.49		0.43		0.92	0.94	0.92	0.77			0.66	
6.00	0.77	0.84	0.84	0.77		0.77		0.92	0.95	0.97	0.92			0.83	
8.00	0.84	0.92	0.92	0.92		0.84		0.92	1.00	1.00	0.98			0.89	
12.00								0.92	1.00	1.08	1.08			0.98	
16.00	0.92	1.07	1.07	1.07		1.07		0.92	1.00	1.08	1.08			1.01	

Table B-5. Horizontal velocities around cube at -z/b = 0.1 during fixed-bed run CU1.

Run No.	CU1									
y/b	0		0.50		0.67		1.00		2.17	
x/b	V/u	θ-deg	V/u	θ-deg	V/u	θ-deg	V/u	θ-deg	V/u	θ-deg
-8.00	1.00	0					1.00	0	1.00	0
-4.00	1.00	0					1.00	0	1.00	0
-2.50	1.00	0					1.04	0	1.04	0
-2.00	0.92	0								
-1.50	0.68	0					1.00	5	1.04	0
-1.00	0.24	0	0.68	30			0.96	10	1.00	0
-0.67	-0.07	180	0.96	35						
-0.50					1.27	18	1.12	11	1.16	0
0.00					0.80	0	1.27	0	1.20	0
0.50					0.56	0	1.12	-10	1.20	0
0.67	-0.12	180	0.40	0						
1.00	-0.33	180	0.27	0			1.07	-15	1.20	0
1.50	-0.12	180	0.40	0			1.00	-11	1.20	0
2.00	0.12	0	0.33	0			0.80	-16	1.20	0
2.50	0.24	0	0.47	0			0.80	0	1.20	0
4.00	0.60	0					0.80	0	1.07	0
6.00	0.87	0								
8.00	0.96	0					0.96	0	0.96	0
12.00	1.00	0								
16.00	1.00	0							1.00	0

Table B-6. Horizontal velocities around cube at -z/b = 0.1 during fixed-bed run CU2.

Run No.	CU2												
y/b	0		0.50		0.67		0.92		1.00		1.50		2.17	
x/b	V/u	θ-deg	V/u	θ-deg	V/u	θ-deg	V/u	θ-deg	V/u	θ-deg	V/u	θ-deg	V/u	θ-deg
-8.00	0.91	0												
-4.00	1.00	0											0.95	0
-2.50	0.95	0											0.91	0
-2.00	0.95	0												
-1.50	0.71	0							1.00	10			0.95	0
-1.00	0.20	0	0.76	24					1.05	12			1.14	0
-0.67	0.00	0	0.76	28									1.29	0
-0.50					1.67	28			1.33	15			1.29	0
0.00					0.71	0	1.94	4	1.67	4	1.52	0	1.33	0
0.50					0.52	0			1.52	-6			1.33	0
0.67	-0.05	180	0.20	0										
1.00	-0.24	180	0.38	0					1.29	-7	1.47	0	1.43	0
1.50	-0.20	180	0.47	0					1.09	-5	1.38	0	1.43	0
2.00	0.00	0	0.52	0					1.00	-5			1.43	0
2.50	0.20	0	0.67	0					0.95	-5	1.29	0	1.38	0
4.00	0.57	0							0.85	0	1.00	0	1.05	0
6.00	0.76	0												
8.00	0.85	0												
12.00	0.95	0												
16.00	0.95	0											1.05	0

Table B-7. Horizontal velocities around cube at -z/b = 0.1 during fixed-bed run CU3.

Run No.	CU3												
y/b	0		0.50		0.67		0.83		1.00		1.50		2.17	
x/b	V/u	θ-deg	V/u	θ-deg	V/u	θ-deg	V/u	θ-deg	V/u	θ-deg	V/u	θ-deg	V/u	θ-deg
-8.00	0.86	0												
-4.00	1.00	0											0.80	0
-2.50	0.93	0											0.86	0
-2.00	0.80	0												
-1.50	0.66	0							0.93	10			0.93	0
-1.00	0.26	0	0.66	25					1.00	20			1.00	0
-0.67	0.00	0	1.06	40										
-0.50					1.59	25			1.46	15			1.26	5
0.00					0.86	0	1.92	10	1.73	10	1.52	5	1.33	5
0.50					0.74	0			1.73	0			1.40	0
0.67	0.00	0	0.20	0										
1.00	0.00	0	0.26	0					1.59	0			1.33	0
1.50	-0.19	180	0.53	0					1.46	-5			1.33	0
2.00	0.00	0	0.26	0					1.33	-5			1.40	0
2.50	0.00	0	0.47	0					1.06	-5			1.33	0
4.00	0.26	0							0.86	0			1.00	0
6.00	0.53	0												
8.00	0.68	0												
12.00	0.80	0												
16.00	0.80	0											0.86	0

Table B-8. Horizontal velocities around cube at -z/b = 0.1 during
fixed-bed run CU4.

Run No.	CU4												
y/b	0		0.50		0.67		0.92		1.00		1.50		2.17	
x/b	V/u	θ-deg	V/u	θ-deg	V/u	θ-deg	V/u	θ-deg	V/u	θ-deg	V/u	θ-deg	V/u	θ-deg
-8.00														
-4.00	1.00	0											1.00	0
-2.50	1.00	0											1.00	0
-2.00														
-1.50	0.66	0							1.00	10	1.08	5	1.08	0
-1.00	0.30	0	0.75	20					1.08	15	1.16	10	1.16	0
-0.67	0.00	0	1.00	35										
-0.50					1.58	26			1.33	15	1.33	10	1.41	0
0.00					0.75	5	1.66	10	1.58	10	1.50	10	1.41	0
0.50					0.83	0			1.58	0	1.58	0	1.50	0
0.67	-0.28	180	0.53	0										
1.00	-0.37	180	1.00	-15					1.58	0	1.58	0	1.50	0
1.50	0.34	0	1.00	-15					1.50	0	1.50	0	1.50	0
2.00	0.59	0	1.00	-10					1.33	0	1.41	0	1.50	0
2.50	0.60	0	1.08	-10					1.33	0	1.41	0	1.50	0
4.00	0.53	0							1.16	0	1.16	0	1.25	0
6.00	0.66	0												
8.00	0.75	0												
12.00														
16.00	1.00	0											1.00	0

Table B-9. Horizontal velocities around cube at -z/b = 0.1 during
fixed-bed run CU5.

CU5													
0		0.50		0.67		0.75		1.00		1.50		2.17	
V/u	θ-deg	V/u	θ-deg	V/u	θ-deg	V/u	θ-deg	V/u	θ-deg	V/u	θ-deg	V/u	θ-deg
1.00	0											0.83	0
0.95	0											0.95	3
0.70	0							0.90	15	1.00	8	1.00	5
0.30	0	0.75	35					1.05	20	1.10	13	1.08	8
-0.15	180	1.05	37										
				1.62	13			1.50	15	1.38	10	1.38	5
				2.05	-5	2.13	-5	1.87	0	1.71	5	1.50	5
				0.25	5			1.75	0	1.80	2	1.62	2
-0.08	180	0.15	0										
-0.17	180	0.45	0					1.68	-2	1.62	-2	1.62	5
-0.30	180	0.40	0					1.75	-3	1.70	0	1.62	0
-0.25	0	0.50	0					1.38	-2	1.62	0	1.68	2
0.22	0							1.00	0	1.10	0	1.15	0
0.55	0												
0.65	0												
												1.13	0
0.85	0												

Table B-10. Horizontal velocities around circular cylinder at
-z/b = 0.1 during fixed-bed run CY.

Run No.	CY											
y/b	0		0.50		0.67		1.00		1.50		2.17	
x/b	V/u	θ-deg	V/u	θ-deg	V/u	θ-deg	V/u	θ-deg	V/u	θ-deg	V/u	θ-deg
-8.00												
-4.00	1.00	0									0.95	0
-2.50	0.95	0									1.03	0
-2.00												
-1.50	0.82	0					1.03	5	1.03	3	1.03	0
-1.00	0.55	0	0.87	10			1.03	7	1.11	5	1.11	0
-0.67	0.24	0	0.87	15								
-0.50			1.18	30			1.18	7	1.18	5	1.18	4
0.00					1.66	12	1.42	0	1.34	0	1.27	0
0.50			1.03	0			1.48	0	1.42	5	1.34	3
0.67	-0.31	180	1.11	0								
1.00	-0.26	180	1.18	0			1.51	0	1.42	0	1.34	0
1.50	0.31	0	1.27	0			1.42	0	1.42	0	1.42	0
2.00												
2.50	0.71	0	1.18	0			1.27	0	1.30	0	1.42	0
4.00	0.80	0					1.11	0	1.11	0	1.15	0
6.00	0.80	0										
8.00	0.87	0										
12.00											1.03	0
16.00	0.95	0									1.03	0

181

Table B-11. Horizontal velocities around sphere at -z/b = 0.1
during fixed-bed run SP.

Run No.	SP											
y/b	0		0.50		0.67		1.00		1.50		2.17	
x/b	V/u	O-deg	V/u	O-deg	V/u	O-deg	V/u	O-deg	V/u	O-deg	V/u	O-deg
-8.00	0.92	0									0.92	0
-4.00	1.00	0					1.00	0			0.97	0
-2.50	1.00	0					1.00	0			1.00	0
-2.00	1.00	0					1.00	0			1.05	0
-1.50	0.92	0					1.00	5	1.09	3	1.05	0
-1.00	0.75	0	0.97	4			1.00	4	1.05	4	1.05	0
-0.67	0.53	0	0.97	20								
-0.50	0.52	0	1.09	22	1.14	20	1.15	15	1.02	10	1.15	5
0.00			1.62	13	1.42	12	1.34	7	1.17	0	1.21	0
0.50	-0.16	180	1.25	0	1.42	10	1.37	15	1.22	5	1.24	2
0.67	-0.13	180	1.09	0								
1.00	0.34	0	0.50	0			1.34	0	1.32	0	1.25	0
1.50	0.92	0	0.59	0			1.32	0	1.32	0	1.25	0
2.00	1.03	0	0.62	0			1.17	0	1.25	0	1.25	0
2.50	1.00	0	0.65	0			1.00	0	1.17	0	1.25	0
4.00	1.00	0	0.80	0			0.84	0	0.99	0	1.00	0
6.00	1.00	0	0.97	0			0.92	0	1.00	0	1.00	0
8.00	1.00	0	0.97	0			0.97	0			1.00	0
12.00	1.00	0										
16.00	1.00	0					1.00	0			1.00	0